FY2010 YEAR END TECHNICAL REPORT

May 17, 2010 to May 16, 2011

Chemical Process Alternatives for Radioactive Waste

Principal Investigator:

D. Roelant, Ph.D.

Florida International University Collaborators:

Dwayne McDaniel, Ph.D., P.E.

Georgio Tachiev, Ph.D., P.E.

Jose Varona, M.S.

Amer Awwad, M.S., P.E.

Seckin Gokaltun, Ph.D.

Romani Patel, M.S.

Tomas Pribanic, M.S.

Prepared for:

U.S. Department of Energy
Office of Environmental Management
Office of Science and Technology
Under Grant No. DE-EM0000598

DISCLAIMER

TABLE OF CONTENTS

TABLE OF CONTENTS i
LIST OF FIGURES iii
LIST OF TABLES vi
PROJECT 1 OVERVIEW 1
TASK 2 FY10 YEAR END TECHNICAL REPORT Waste Slurry Transport Characterization 2
EXECUTIVE SUMMARY 2
INTRODUCTION 4
EXPERIMENTAL TESTING OF THE ASYNCHRONOCUS PULSING SYSTEM 5
RESULTS - ASYNCHRONOCUS PULSING SYSTEM 10
EXPERIMENTAL TESTING OF THE SECOND GENERATION PERISTALTIC CRAWLER 15
RESULTS - SECOND GENERATION PERISTALTIC CRAWLER 23
CONCLUSIONS 26
REFERENCES 28
TASK 12 FY10 YEAR END TECHNICAL REPORT Multiple-Relaxation-Time Lattice Boltzmann Model for Multiphase Flows 29
EXECUTIVE SUMMARY 29
INTRODUCTION 30
RESULTS 36
OVERALL PROJECT CONCLUSIONS 40
REFERENCES 41
TASK 13 FY10 YEAR END TECHNICAL REPORT Hydrodynamic Properties and Rheology of High-Level Waste Fluids 42
EXECUTIVE SUMMARY 42
INTRODUCTION 43
EXPERIMENTAL 44
RESULTS 56
OVERALL PROJECT CONCLUSIONS 70
REFERENCES 71
APPENDIX A. 72
TASK 15 FY10 YEAR END TECHNICAL REPORT Evaluation of Advanced Instrumentation Needs for HLW Retrieval 76
EXECUTIVE SUMMARY 76
INTRODUCTION 78
LITERATURE & TECHNOLOGY REVIEW 80
EXPERIMENTAL APPROACH 85

RESULTS & DISCUSSION 91
CONCLUSIONS.....96
REFERENCES 97
APPENDIX A.....99
APPENDIX B 101

LIST OF FIGURES

Figure 1. Pipeline unplugging scenario in a horizontal pipe. 5
Figure 2. Schematic showing the net effect of two-sided pulsing on the plug pressure. 6
Figure 3. Experimental set-up used for validating APS. 6
Figure 4. Top view of the testbed utilized for the experimental testing. 7
Figure 5. Detail views of the relief valve and ball valve used in the pipeline. 7
Figure 6. Detail views of valve used for draining the pipeline. 8
Figure 7. Screen captures of the software developed to control and record the experimental data for the system. 8
Figure 8. Results from parametric testing with pipeline initially pressurized to 40 psi. 10
Figure 9. Pressure readings at the plug location for the left and right pipeline operated at 1 Hz using a sine wave profile. 11
Figure 10. Pressure readings at the plug location for the left and right pipeline operated at 0.25 Hz using a square wave profile. 12
Figure 11. Pressure readings at the plug location for the left and right pipeline operated at 0.5 Hz using a sine wave profile. 12
Figure 12. Accelerometer readings for the X-axis (along the pipeline) operated at 1 Hz using a sine wave profile. 13
Figure 13. Results with hydraulic oil set to 300 psi. 14
Figure 14. Results with hydraulic oil set to 500 psi. 14
Figure 15. Results with hydraulic oil set to 700 psi. 14
Figure 16. Side view of the peristaltic crawler. 15
Figure 17. Section view of crawler with an auger attachment. 16
Figure 18. Schematic of pneumatic system for the crawler. 17
Figure 19. Pneumatic system to power unplugging attachment. 17
Figure 20. Side view of first generation crawler. 18
Figure 21. A) Edge-welded bellow B) detail cross section of edge-welded below C) hydro-formed bellow. 19
Figure 22. Burst pressure test on hydro-formed bellow. 19
Figure 23. Double walled bellow assembly contracted due to vacuum pressure. 20
Figure 24. A) Natural rubber pressurize cavity, B) flexible PVC pressurize cavity. 20
Figure 25. A) Rim showing grooves for clamps, B) front rim assemble and pressurized. 21
Figure 26. A) Screen capture of OMRON software, B) control unit and pneumatic system to control SGPC. 21

Figure 27. A) Rotating nozzle attachment, B) 15° nozzle attachment..... 22
Figure 28. Testbed used for the speed test..... 23
Figure 29. Sequence of crawler turning through an 90° elbow. 24
Figure 30. Testbed used to measure the pulling force. 24
Figure 31. Pulling force vs. bellow pressure..... 24
Figure 32. (a) Setup used to perform the sodium-aluminum-silicate unplugging test, (b) pipe after unplugging operation. 25
Figure 33. D2Q9 lattice structure..... 31
Figure 34. Effect of interface thickness on the pressure difference across the bubble interface at three different values of surface tension. 36
Figure 35. Effect of interface thickness on the magnitude of maximum parasitic velocity in the vicinity of the bubble interface at three different values of surface tension calculated with MRT and the BGK LBM. 37
Figure 36. MRT and BGK solution for the evolution of a rising bubble at Eo=9, $M=6x10^{-4}$. 38
Figure 37. Vertical velocity component calculated using MRT and BGK methods. 39
Figure 38. Experimental set-up..... 44
Figure 39. Test column set-up. 45
Figure 40. Rake impeller (left) and spargers (right). 46
Figure 41. Gas flow during purging and simulant conditioning..... 47
Figure 42. Gas flow during hydrogen peroxide injection. 47
Figure 43. Gas flow during release of oxygen from gelled state. 48
Figure 44. Correlation between Bingham yield stress and kaolin-bentonite concentration at 25 °C. 54
Figure 45. Repeatability tests with 2 Pa slurry. 56
Figure 48. Total oxygen released for the 2 Pa test..... 57
Figure 49. Oxygen concentration during release. 58
Figure 50. Oxygen concentration during the first 15 minutes. 58
Figure 51. Comparison of the total oxygen gas released. 59
Figure 52. Comparison of oxygen concentration in the effluent stream..... 60
Figure 54. Percentage of oxygen released in the first 20 minutes. 61
Figure 55. Comparison of release curves with and without AFA for 7 Pa..... 62
Figure 56. Total oxygen released during the release test for 7 Pa. 63
Figure 57. Comparison of release curves for Kaolin-bentonite tests with AFA..... 63

Figure 59. Oxygen peaks detected during hydrogen peroxide injection for AZ-101+Clay mix tests. 65

Figure 60. Release curve of 7 Pa AZ-101+Clay mix at 350 rpm. 65

Figure 61. Total oxygen released during the release test of 4 Pa and 7 Pa for AZ-101+Clay mix. 66

Figure 63. Release Profile of the 4 Pa with AFA Test..... 67

Figure 64. Comparison of release curves with and without AFA for 4 Pa. 67

Figure 65. Comparison of release rates for 4 Pa tests with and without AFA. 68

Figure 66. Comparison of release profiles for tests with AFA. 68

Figure 68. Calibration curve of argon in nitrogen at various concentrations. 74

Figure 69. Mass balance of argon. 74

Figure 70. Mass balance of nitrogen. 75

Figure 71. Mass balance of argon-nitrogen mix. 75

Figure 72. USS Probe 82

Figure 73. Probe close-up drawing of sensing zone (Courtesy of Industrial Tomography Systems plc). 82

Figure 74. Mixing and sampling loop diagram. 88

Figure 75. Sampling loop at FIU. The sampling pump and Coriolis meter are visible in the center and top of the image. 88

Figure 76. Benchtop test setup. Preliminary solids loading tests and troubleshooting were performed in this setup. 89

Figure 77. USS System installed in laboratory. The hardware components are shown: (1) controller, (2) probe. 91

Figure 78. 40 mm spacers provided a 7.83 mm propagation path for the ultrasonic pulse. 92

Figure 79. 36 mm spacers reduced the propagation path to 3.83 mm, allowing for higher solids concentration in the media under test. 92

Figure 80. Attenuation versus pulse frequency for various $AL(OH)_3$ concentrations. 93

Figure 81. Attenuation profile at 10MHz pulse for varying bulk density 94

Figure 82. Relationship between liquid solution and solid/liquid suspension densities and velocity. 95

LIST OF TABLES

Table 1. Significant Simulant Properties for Hybrid Mixing Systems and Goal Values 49

Table 2. Simulants Used in the Test Program..... 49

Table 3. Summary of In-situ Gas Retention and Release Test Conditions Using Peroxide without AFA..... 50

Table 4. Summary of In-situ Gas Retention and Release Test Conditions Using Peroxide with AFA..... 50

Table 5. Summary of In-situ Gas Retention and Release Test Conditions Using Peroxide without AFA..... 50

Table 6. Summary of In-situ Gas Retention and Release Test Conditions Using Peroxide with AFA..... 51

Table 7. Yield Stress and Viscosity Measurements for Kaolin-Bentonite Simulant without AFA 51

Table 8. Yield Stress and Viscosity Measurements for Kaolin-Bentonite Simulant with AFA... 52

Table 9. Yield Stress and Viscosity Measurements for AZ-101+Clay Mix without AFA..... 53

Table 10. Yield Stress and Viscosity Measurements for AZ-101+Clay mix with AFA 53

Table 11. Summary of In-situ Gas Retention and Release Test Results for Kaolin-Bentonite without AFA 56

Table 12. Summary of Release Parameters 61

Table 13. Summary of In-situ Gas Retention and Release Test Results for Kaolin-bentonite with and without AFA..... 62

Table 14. Comparison of Release Parameters of Kaolin-Bentonite with and without AFA 64

Table 15. Summary of In-situ Gas Retention and Release Test Results for AZ-101-Clay Mix without AFA 64

Table 16. Summary of Release Parameters for AZ-101+Clay Simulant..... 66

Table 17. Summary of In-situ Gas Retention and Release Test Results for AZ-101+Clay Mix with AFA 67

Table 19. Statistical Values for 100 ppm of Argon in Nitrogen..... 72

Table 20. Statistical Values for 500 ppm of Argon in Nitrogen..... 72

Table 21. Statistical Values for 5000 ppm of Argon in Nitrogen..... 73

Table 22. Hanford Tank Waste Parameters/Ranges Varied for Simulant Slurries..... 87

Table 23. Slurries Prepared for Technology Assessment 90

Table 24. Preliminary Results for Various Test Runs 92

PROJECT 1 OVERVIEW

The Department of Energy's (DOE's) Office of Environmental Management (EM) has a mission to clean up the contaminated soils, groundwater, buildings and wastes generated over the past 60 years by the R&D and production of nuclear weapons. The nation's nuclear weapons complex generated complex radioactive and chemical wastes. This project is focused on tasks to support the safe and effective storage, retrieval and treatment of high-level waste (HLW) from tanks at Hanford and Savannah River sites. The objective of this project is to provide the sites with modeling, pilot-scale studies on simulated wastes, technology assessment and testing, and technology development to support critical issues related to HLW retrieval and processing. Florida International University (FIU) engineers work directly with site engineers to plan, execute and analyze results of applied research and development.

During FY10 Project 1, titled "Chemical Process Alternatives for Radioactive Waste", focused on four tasks related to HLW research at FIU. These tasks are listed below and this report contains a detailed summary of the work accomplished for FY10.

Task 2 - Waste Slurry Transport Characterization: The objective of this task is to qualify (test & evaluate) pipeline unplugging technologies for deployment at the DOE sites. Additionally, FIU will work closely with engineers from Hanford's Tank Farms and Waste Treatment and Immobilization Plant on developing alternative pipeline unplugging technologies.

Task 12 - Multiple-Relaxation-Time Lattice Boltzmann Model for Multiphase Flows: The objective of this task is to develop stable computational models based on the multiple-relaxation-time lattice Boltzmann method. The computational modeling will assist site engineers with critical issues related to HLW retrieval and processing.

Task 13 - Hydrodynamic Properties and Rheology of High-Level Waste Fluids: The objective of this task is to conduct experimental and numerical work for selected stimulants (relevant to HLW fluids and with known hydrodynamic and rheological properties) and correlate the rheological parameters with the settling and mixing properties, gas retention and release, and foaming behavior. The experimental results from the tests will be correlated with bubble coalescence in non-Newtonian fluids, and analysis will be performed to identify the principal properties of the solids phase that stabilize the bubble to bubble interface. This includes particle size, morphology, surface chemistry, zeta-potential and the liquid-gas-solid interfacial tension.

Task 15 - Evaluation of Advanced Instrumentation Needs for HLW Retrieval: This task will evaluate the maturity and effectiveness of commercial and emerging technologies capable of addressing several instrumentation needs for HLW feed mixing and retrieval. Promising candidate technologies will be evaluated for their functional and operational capabilities and the technologies that show sufficient feasibility for deployment will be subjected to additional tests to determine their effectiveness in the harsh chemical and nuclear radiation tank environments.

TASK 2 FY10 YEAR END TECHNICAL REPORT
Waste Slurry Transport Characterization

EXECUTIVE SUMMARY

In previous years, Florida International University (FIU) has tested and evaluated a number of commercially available pipeline unplugging technologies. Two of the more promising technologies (AIMM Technologies' Hydrokinetic Method and NuVision's wave erosion technology) were further evaluated and found to have shortcomings associated with their processes. Based on the lessons learned from the evaluation of the technologies, two alternative approaches were proposed by FIU. These are an asynchronous pulsing system (APS) and a peristaltic crawler. The APS is based on the principle of creating pressure waves in the pipeline filled with water from both ends of the blocked section in order to break the bonds of the blocking material with the pipe wall via forces created by the pressure waves. The waves are created asynchronously in order to shake the blockage as a result of the unsteady forces created by the waves. The peristaltic crawler is a pneumatically operated crawler that propels itself by a sequence of pressurization/depressurization of cavities (inner tubes). The changes in pressure result in the translation of the vessel by peristaltic movements.

For this performance period, the first phase of the experimental testing of the APS was conducted. The infrastructure that includes the pulse generation unit, testbed, instrumentation, and data acquisition unit was developed and assembled. The hydraulic powered pulse generation unit was designed and procured having a maximum pulsing frequency of 20 Hz. The software required to control the unit was developed allowing for the generation of pressure pulse waves having a sinusoidal or square profile. The testbed consisted of a 40 ft 3 in diameter pipeline having a solid aluminum cylinder in the middle to emulate a plug. Each side of the pipeline consists of two 10 ft sections with a 90° elbow. The pipeline is heavily instrumented with pressure transducers, accelerometers and thermocouples to capture the changes resulting from the pressure pulses generated. Tests were performed for pulse frequencies ranging from 0.125 Hz to 10 Hz. Results show clear asynchronous pressures at each of the sides of the aluminum cylinder for frequencies lower than 2 Hz. Results were inconclusive for higher frequencies.

Using the capability of the pulse generation unit, a second set of tests was performed to attempt resonating the water column. These tests were carried out using half of the testbed. The frequencies generated ranged from 2 Hz to 20 Hz. To evaluate the effect of the air in the pipeline, the pipeline was tested with 100% water and also for 87.5% and 75% water to air. Only trials with the hydraulic oil set to 300 psi and 25% air demonstrated a significant increase in vibration response. This occurred at the 2-6 Hz range.

Additionally, the second generation peristaltic crawler (SGPC) was designed, assembled and experimentally tested. Improvements on the materials and design of the unit were implemented to improve its durability and maximum pressure rating. Edge-welded and hydro-formed stainless steel bellows were evaluated and tested. Improvements on the front and back cavities were also develop to minimize possible leaks and increase the anchoring force of the crawler to the pipeline. The control systems for the crawler were automated to provide a joystick controlled forward and backward motion.

The experimental testing of the crawler included a speed test yielding a maximum speed of 0.5 ft/min. The maneuverability test indicated that the crawler is able to navigate through a 90° PVC elbow having a radius of 5.56 ins in a time of approximately 7.5 minutes. The maximum pulling force achieve by the crawler was 110 lb of force when providing 90 psi of pressure to the bellow. Two high pressure water nozzles were used to test the crawler unplugging ability: 1) a rotating nozzle and 2) a 15° nozzle. Results showed that the 15° nozzle provided the most effective unplugging effect on clay and salt based plugs.

INTRODUCTION

Pumping high-level waste (HLW) between storage tanks or treatment facilities is a common practice performed at Department of Energy (DOE) Sites. Changes in the chemical and/or physical properties of the HLW slurry during the transfer process may lead to the formation of blockages inside the pipelines. Current commercially available pipeline unplugging technologies do not provide results that are cost-effective and reliable. As part of the research objectives at Florida International University (FIU), novel pipeline unplugging technologies that have the potential to efficiently remediate cross-site and transfer line plugging incidents are being developed. These are an asynchronous pulsing system (APS) and a peristaltic crawler. This report presents details of the devices and procedures used for the experimental testing of the two technologies. The first section pertains to the experimental testing of the APS followed by the experimental testing of the peristaltic crawler.

Initially, a brief background on the principles in which the APS technology is based is provided. A detailed description is then provided of the hydraulic unit employed to generate the pressure pulses that creates the desired disturbances. The functioning and capabilities for the hydraulic unit to create a specific pulse profile are also explained. In addition, this report explains the procedure implemented to use the pulse generation hydraulic unit to study water column vibration as an alternative method for pipeline unplugging. Using the described system, results obtained during the experimental phase of the project are presented. This includes data from asynchronous pulsing and water column vibration tests.

In addition, this document presents the design of the second generation peristaltic crawler (SGPC) unit. It includes the evaluation of different materials and configuration that could allow it to withstand operations in a HLW environment. Improvements from the original prototype are outlined and the rationale for the changes is explained. This document also presents the systems used for automating the motion of the crawler and provides the specifics on the procedures to follow for its operation.

For each of the technologies developed during this performance period, a description of the testbeds used for the experimental validation is presented. Their characteristics were designed to emulate possible scenarios present in the DOE pipelines. For the case of the asynchronous pulsing, a heavily instrumented 3 in diameter pipeline was used. Pressure transducers and vibration recording accelerometers were installed along the pipeline to capture the propagation of the pulses generated by the hydraulic unit. The testbed used for the Peristaltic Crawler included obstacles by means of changes in pipeline direction to challenge the crawler ability to navigate through and conform to different pipeline geometry. This document also presents the details of the trials performed to test the crawler's effectiveness in performing unplugging operations as well as its pulling force ability.

Finally, preliminary conclusions from the results obtained for each technology are presented. Based on the results and conclusions, recommendations of the path forward are provided.

EXPERIMENTAL TESTING OF THE ASYNCHRONOCUS PULSING SYSTEM

Background

In order to clear plugged radioactive waste transfer lines, non-invasive techniques can have significant advantages since problems such as contamination clean-up and exposure to radioactive waste of invasive devices can be avoided. FIU has evaluated two technologies that fall in this category, namely, NuVision's wave erosion method and AIMM Technologies' Hydrokinetics method. These technologies fill the plugged pipeline with water up to an operating pressure level and induce a pressure variation at the inlet of the pipeline to dislodge the plug. Using the experience obtained during experimental evaluations of both technologies, FIU has developed a non-invasive unplugging technology called APS that combines the attributes of previously tested technologies.

A pipeline unplugging technology using similar principles for generating pressure pulses in pipelines has previously been tested at the Idaho National Laboratory (INL) by Zollinger and Carney [1]. The most relevant difference of the current technology from the unplugging method developed at INL is that both sides of the pipeline are used to create the asynchronous pulsing in the current technology. The pulse generation unit for the APS was optimized to maximize the effect of the pressure differential at the plug faces. Figure 1 shows a sketch of how this technology can be utilized for a typical plugging scenario.

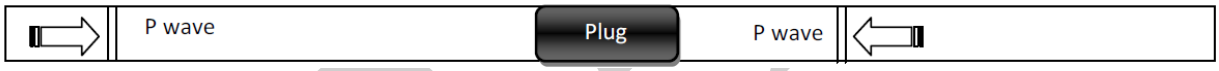

Figure 1. Pipeline unplugging scenario in a horizontal pipe.

Theory of Operation

The APS is based on the idea of creating pressure waves in the pipeline filled with water from both ends of the blocked section in order to dislodge the blocking material via forces created by the pressure waves. The waves are generated asynchronously in order to break the mechanical bonds between the blockage and the pipe walls as a result of the vibration caused by the unsteady forces created by the waves (Figure 2). The general unplugging procedure for using the APS is as follows:

1. To optimize the process, flush the liquid in the pipes and evacuate the air using a vacuum pump on both sides of the blockage, if possible.
2. Fill the pipeline from both ends with water up to a specified pressure.
3. Start asynchronous pulsing by creating positive pressure waves at both ends of the pipeline by adjusting the frequency and phase shift between two pulse generators.

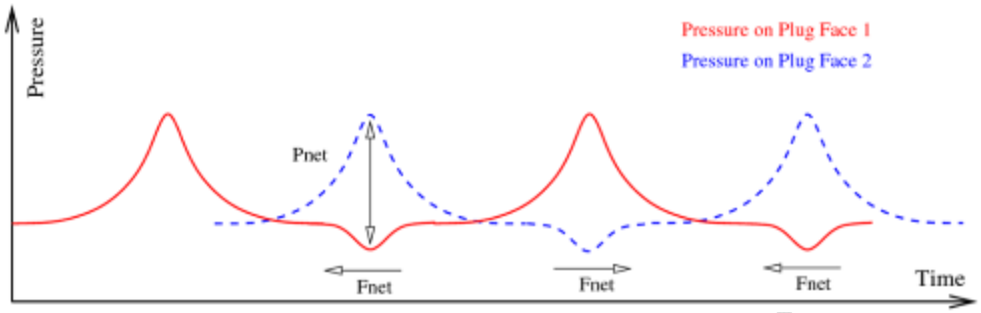

Figure 2. Schematic showing the net effect of two-sided pulsing on the plug pressure.

General Description

The experimental set-up includes a hydraulic pulse generation unit, pipeline testbed, and data acquisition unit. As shown in Figure 3, the experimental test loop was assembled using four 10 ft straight sections and two 90° elbows. The pipes used for the loop are 3 in diameter schedule 10 carbon steel pipes. A solid aluminum cylinder is placed at the center of the 20 ft straight section to emulate a blockage in the pipeline. The pipeline is instrumented with accelerometers, pressure transducers and thermocouples located at strategic locations to capture the changes of the induced disturbances inside the pipeline. Figure 3 shows a descriptive illustration of the infrastructure used to experimentally test the APS.

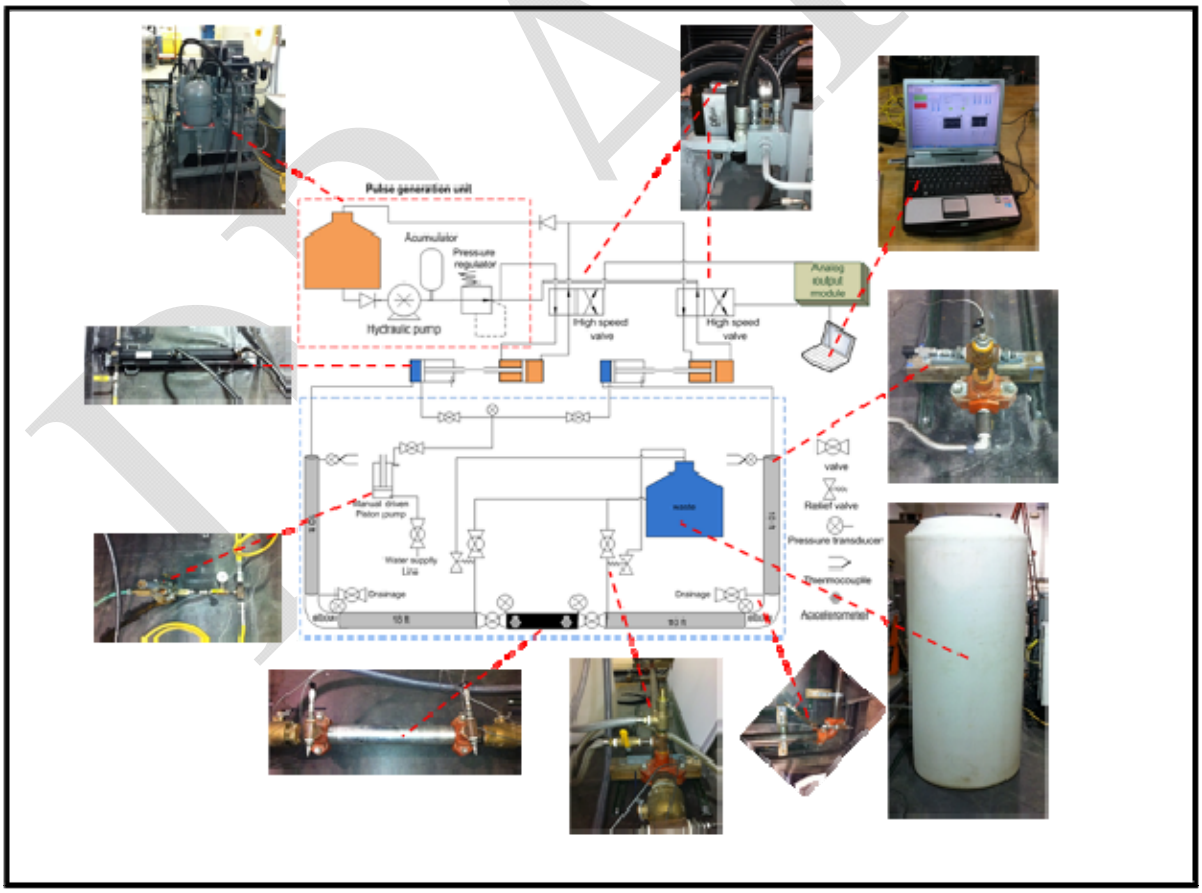

Figure 3. Experimental set-up used for validating APS.

Bench-scale pipeline for APS testing

The APS requires the use two types of pressurized fluids: hydraulic oil and water. The hydraulic oil is pressurized by the pulse generation unit to generate a force by each one of the two tandem pistons. The other side of the tandem pistons is flooded with water and connected to the pipeline by mean of hydraulic lines. This arrangement results in a direct relationship between the pressure of the oil in the system and the water pressure inside the pipeline. Figure 4 shows the top view of the experimental set-up assembled to create the bench-scale pipeline to perform the testing of the APS.

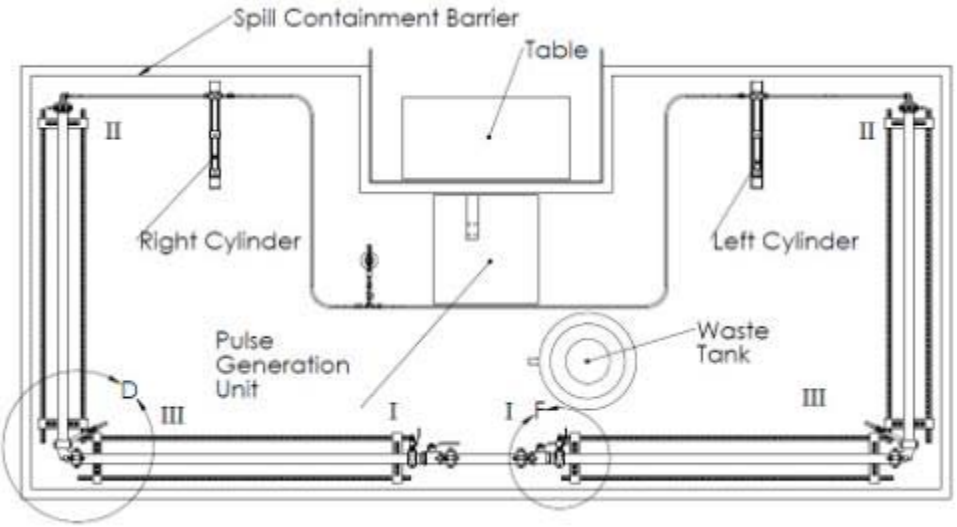

Figure 4. Top view of the testbed utilized for the experimental testing.

For the water side of the system, pressure relief valves (PRVs) were located at each end of the plug to prevent an over-pressurization condition. Figure 5 shows detail F describing the plumbing arrangement of the PRV and bleeding line.

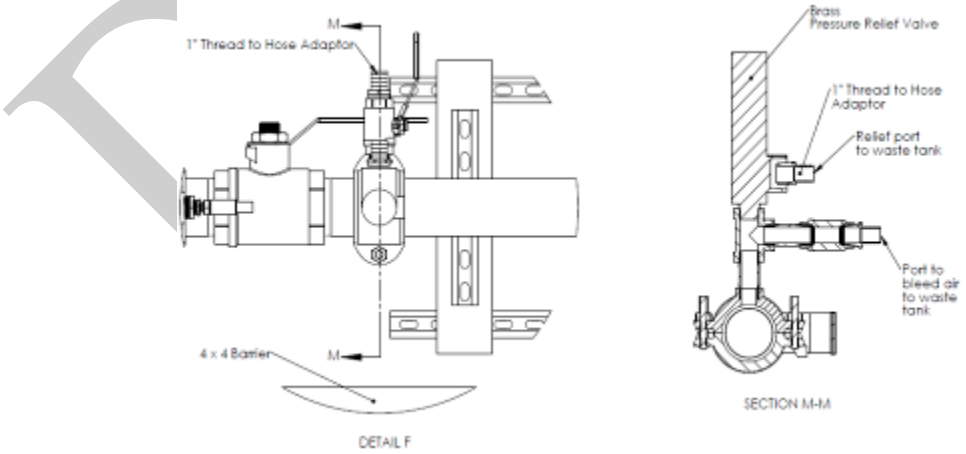

Figure 5. Detail views of the relief valve and ball valve used in the pipeline.

Once all trials were performed, the pipeline arrangement is designed so that the water could be removed by connecting a pump from the ball valves located at the 90° elbows to a water storage container. To provide appropriate height differences to promote the flow of fluid to these ports,

the system has three different height levels each one having about a 1in difference. As indicated in Figure 4, the highest point is located at the plug (I) and the lowest at the elbows (III). The inlet points (II) have a height between (I) and (III). Figure 6 shows the detail of D from Figure 4 depicting the location of one of the drainage ports. This drainage port was also used to empty a percentage of the water in the pipeline to test the performance of the APS with different water to air ratios.

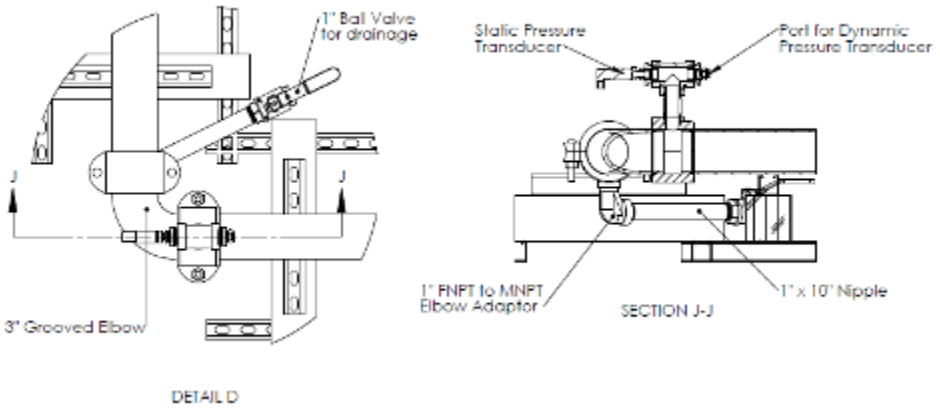

Figure 6. Detail views of valve used for draining the pipeline.

Data acquisition unit

The APS control and monitoring system consists of two modules operating via a synchronized communication bus. The first module provides status of the relevant states of the hydraulic equipment and user control operations of the hydraulic power system. This controller allows parallelization of I/O functions and provides synchronization of cylinder pulsing during the system drive phase. The second module provides all experimental test loop data and logging functionality. Both modules communicate via a dedicated time-synchronized protocol. The current implementation of pulse generation algorithm allows the user to determine the maximum piston travel distance and implements the inverse on the other side simultaneously. This leads to a maximum differential pressure on the plug. Figure 7 shows screen captures of the software developed to control and record the experimental data.

Figure 7. Screen captures of the software developed to control and record the experimental data for the system.

Instrumentation

To measure the pressure changes along the pipeline, a total of 6 pressure transducers were used; three on each side of the pipeline located at points (I), (II) and (III) as shown in Figure 4. Their range and accuracy are 0 to 1000 psig and +/- 2%, respectively. The temperature was recorded using two thermocouples, each located at point (II) on the pipeline. Their range and accuracy are -200 C to 1250 C and +/- 0.75%, respectively. Vibration resulting from the pressure pulses was recorded using two 3-axis accelerometers placed at each side of the solid aluminum cylinder that emulates a plug. Their range and accuracy are +/- 2.4 g and +/- 1.25%, respectively. All the data was recorded with a sampling rate of 1 ms.

RESULTS - ASYNCHRONOCUS PULSING SYSTEM

Evaluating the System Response

After the infrastructure was assembled, the testing began by evaluating the response of the hydraulic system. One side of the pipeline was initially flooded with water and pressurized to 40 psi. Parametric tests were conducted to determine which system parameters provided the maximum inlet pressure. The three system parameters considered were the oil side pressure, percentage of valve opening, and duration of pulse. Figure 8 shows the results from the parametric testing of the system. The maximum pressure pulse achieved was at an oil pressure (hydraulic unit pressure) of 500 psi with a 5 second pulse duration at 100% of the valve opening.

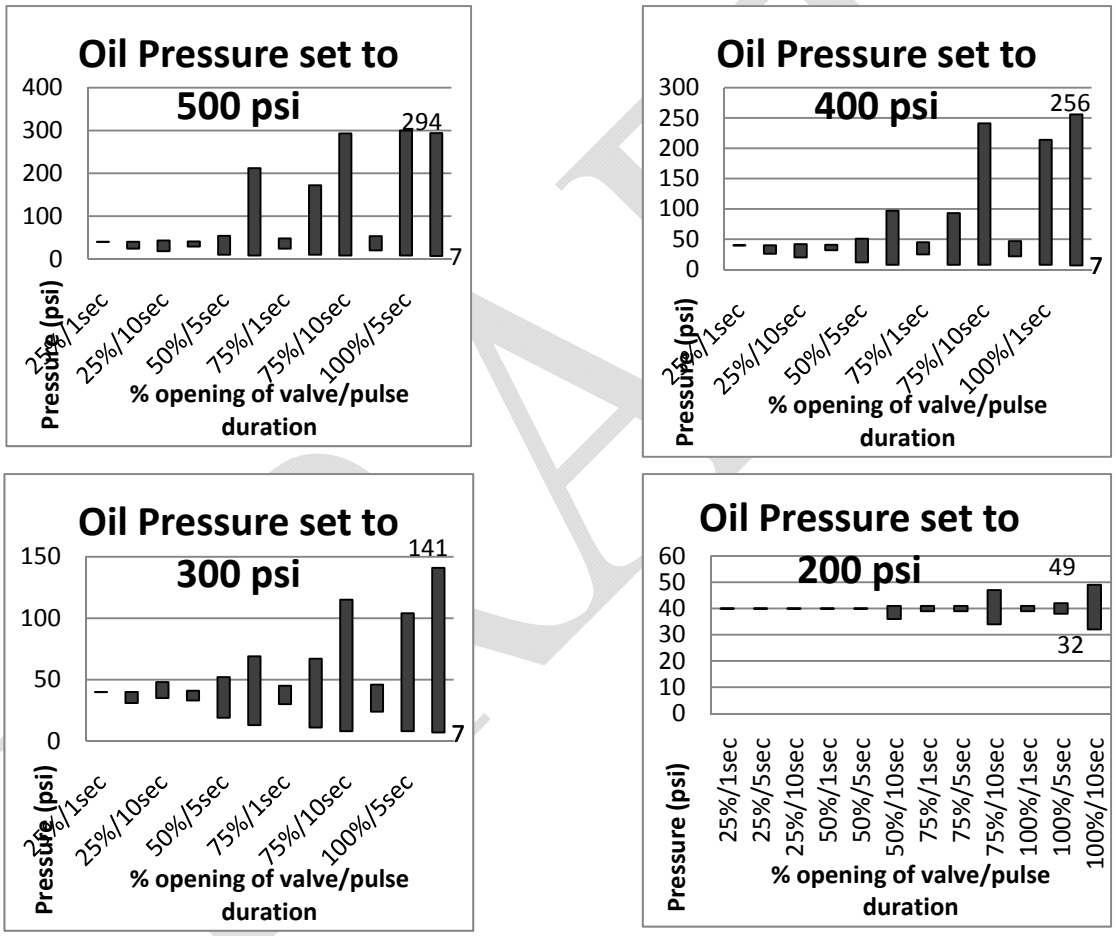

Figure 8. Results from parametric testing with pipeline initially pressurized to 40 psi.

From the parametric testing it was observed that for a fully flooded pipeline, the maximum pressure differential (260 psi) was developed applying the pulse with the following conditions: the hydraulic system was set to 500 psi, the valve was 100% open, and the valve open time was 5 seconds. The trend for all pressure differentials indicated that the percentage of the valve opening was the variable that had the strongest effect in the resulting pressure differential.

Evaluation of the APS

Using the results from the evaluation phase, a matrix of test pressures and frequencies was constructed. Testing of the APS first required that the pipeline was flooded and subsequently pressurized to 120 psi by introducing additional water using a manual pump. Once pressurized, four sets of tests were conducted: two using the a pulse having a sine wave profile and two using a pulse having a square wave profile. For each pulse profile, the pressure in the hydraulic unit was set to 300 and 500 psi. These pressures correspond to inlet pressures of interest (141 to 300 psi). The frequencies used for each set of tests were 0.125, 0.25, 0.5, 1, 2, 4, 6, 8, and 10 Hz. The recoding intervals of the data acquisition system was 1 ms and the approximate time of each trial was 20 seconds.

Figure 9 shows a 5 second interval of the pressure data elapsed on a fully flooded pipeline initially pressurized at using a sine wave profile of 1 Hz with an oil pressure of 500 psi. The figure clearly shows the asynchronous pressures achieved at the plug location providing a maximum pressure differential of 88 psi between the left and right side of the plug. Performance of the right cylinder limited the ability of the system to supply similar magnitudes of pressure from each side. Additionally, tests showed no significant degradation on the pressure pulses for a fully flooded pipeline between the inlet and the plug location.

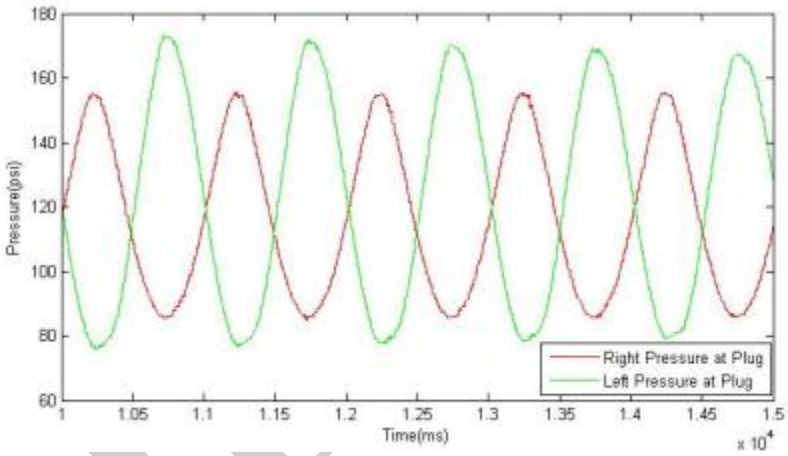

Figure 9. Pressure readings at the plug location for the left and right pipeline operated at 1 Hz using a sine wave profile.

Test performed with a square pulse profile provided similar results as those performed with a sine wave profile. Figure 10 shows the results of the pressure reading at the plug location resulting from generating a pressure pulse having a square profile.

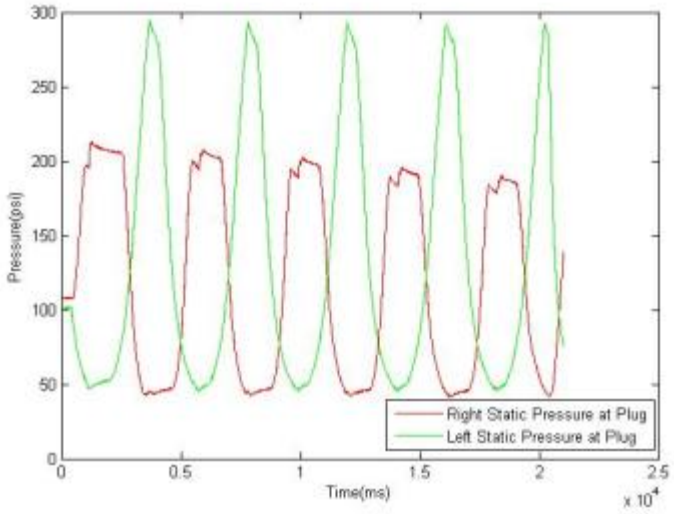

Figure 10. Pressure readings at the plug location for the left and right pipeline operated at 0.25 Hz using a square wave profile.

Tests performed at frequencies higher than 2 Hz did not provide conclusive results due to performance issues with one of the cylinders.

Tests performed at hydraulic oil pressures lower than 300 psi did not yield conclusive results due to the force required to overcome the friction prior to displacing the piston on the right cylinder of the system. Figure 11 shows the pressure reading of a trial performed with the hydraulic oil pressure set to 300 psi with a sine wave of 0.5 Hz.

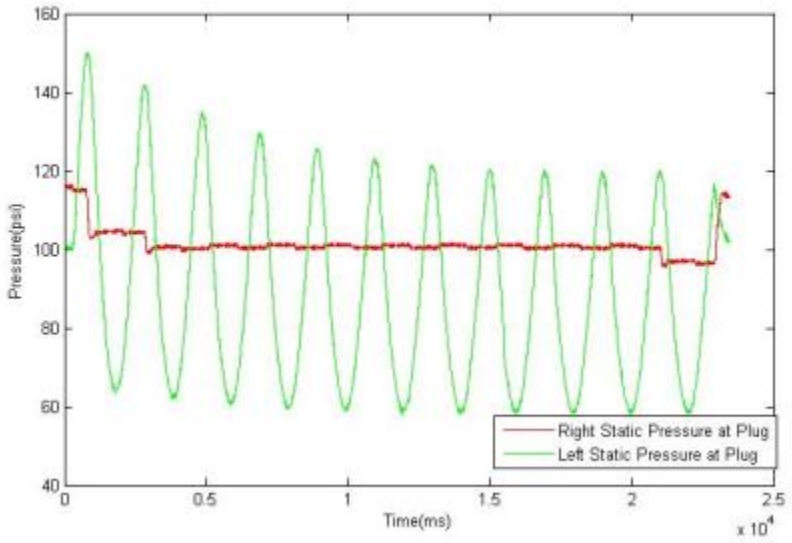

Figure 11. Pressure readings at the plug location for the left and right pipeline operated at 0.5 Hz using a sine wave profile.

The vibration data recorded by the accelerometers showed a clear correspondence to the pressure pulses generated. Figure 12 shows the vibration data for the x-axis (along the pipeline) for the trial shown in Figure 9. The figure clearly shows the corresponding vibration pulses created when the pressure differential is maxima between the left and right of the plug.

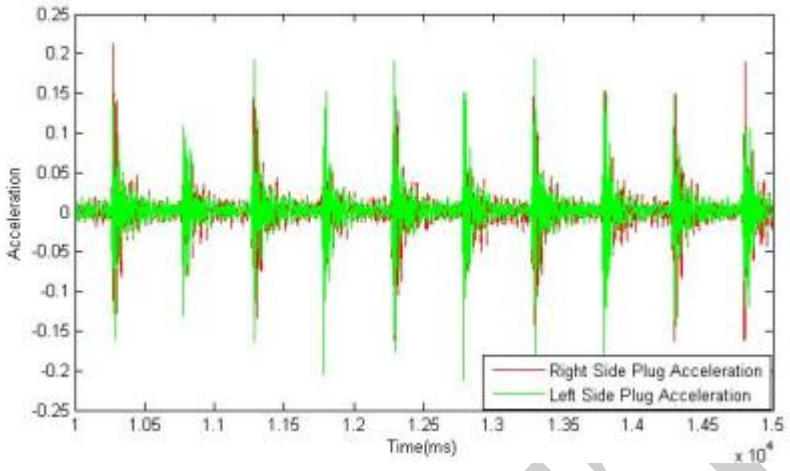

Figure 12. Accelerometer readings for the X-axis (along the pipeline) operated at 1 Hz using a sine wave profile.

Evaluation of Water Column Vibration

In an effort to resonate the water column, the hydraulic oil pressure was set to 300, 500, and 700 psi. All trials were performed using a sinusoidal pulse profile with an initial static pressure of approximately 120 psi. The range of frequencies tested was between 2 to 20 Hz. The effect of air entrained in the pipeline on the water column vibration was also evaluated. After conducting trials with a fully flooded pipeline tests were conducted with different water to air ratios. The pipeline was brought to atmospheric pressure and air was introduced by opening a relief valve and allowing water to exit through a drainage port. By measuring the amount of water that was removed from the pipeline, it was possible to determine the initial water to air ratio by volume in the system. The tests were performed for 12.5% and 25% air in the system. The effect of air entrained for the APS study can be determined by considering the lower frequency tests from these water column vibration tests. Figure 13, through Figure 15 show the results for with varying frequencies in the pressure pulses to the vibration recorded at the plug location.

Trials with the hydraulic oil set to 300 psi and 25% air demonstrated a significant increase in vibration response. This occurred at the 2-6 Hz range. In the 300 and 500 psi trials, the vibration response was similar for the fully flooded and 12.5% air tests. For the 700 psi trials, the fully flooded system had significantly lower responses than the partially flooded systems.

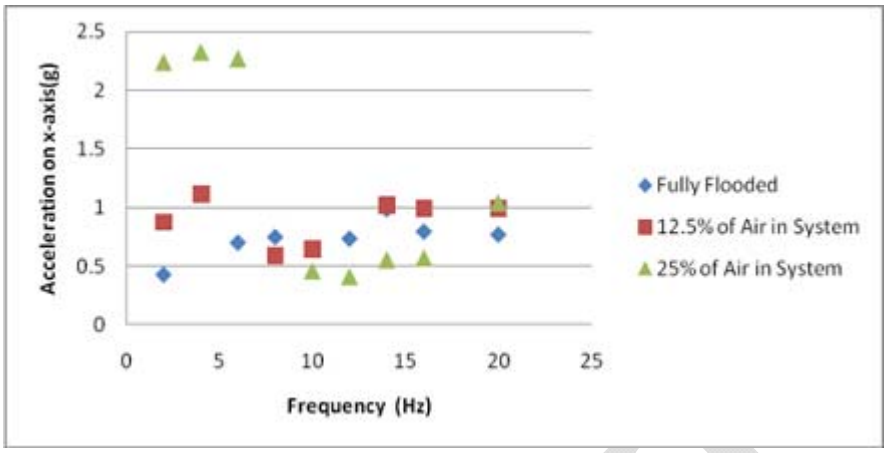

Figure 13. Results with hydraulic oil set to 300 psi.

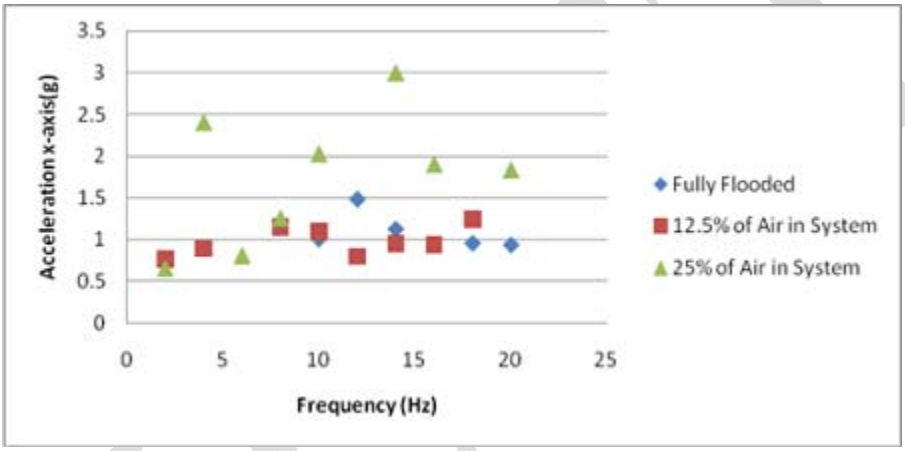

Figure 14. Results with hydraulic oil set to 500 psi.

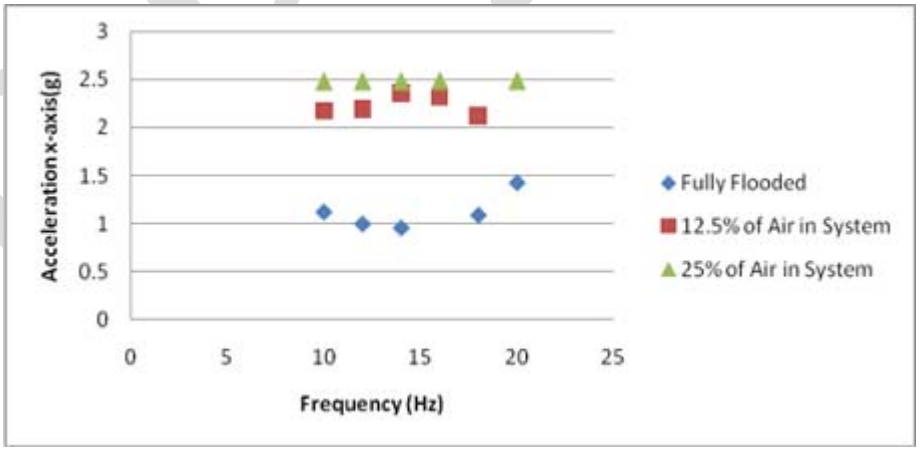

Figure 15. Results with hydraulic oil set to 700 psi.

EXPERIMENTAL TESTING OF THE SECOND GENERATION PERISTALTIC CRAWLER

Background

During FY10, FIU also designed, assembled and conducted experimental testing of the second generation peristaltic crawler. The experimental testing focused on determining the crawler's ability to navigate through a 90° elbow, speed achieved inside a pipeline, maximum pulling force, and unplugging ability. First, the improvement and rational behind the changes implemented from the first generation are presented and explained. The general set up of the control systems is also presented as well as details on the testbeds and results recorded during the experimental trials. Finally conclusions and recommendations of the design are provided.

The peristaltic crawler is a pneumatically powered crawler that propels itself by a sequence of pressurization/depressurization of cavities (inner tubes). The changes in pressure result in the translation of the vessel by peristaltic movements. The inner tubes are mounted on a flexible skeleton that allows it to navigate through elbows. The advantage of using a device that can successfully navigate inside pipelines is the ability to bring unplugging technologies closer to the blockage. Figure 16 shows a side view of the second generation crawler unit.

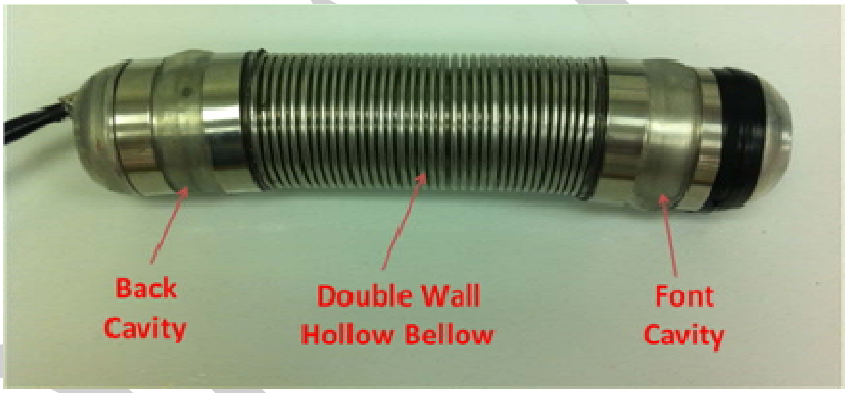

Figure 16. Side view of the peristaltic crawler.

The use of a peristaltic movement mechanism to propel a device inside a pipeline has been previously used in inspection devices. One example is the system presented by Shishido in the patent, “Pipe-Inspecting Apparatus Having a Self Propelled Unit” [2]. Another similar device with this propelling system was invented by Zollinger [3] which was designed to pull tethers behind underground boring devices.

The novelty of using peristaltic motion to successfully propel a device inside HLW lines creates the possibility of using the crawler as a vessel to carry unplugging technologies. By reducing the distance between the unplugging tool and the location where the plug formed, the success rate for removing the blockage is greatly increased. During the conceptual phase of this project, the peristaltic crawler was designed to have the capability of using interchangeable tool attachments depending on the type of blockage to be unplugged. Attachments are firmly bolted in place to the front rim of the unit. For all the attachments, the power source used is a pressurized water line that passes through the crawler. Figure 17 shows a side view of the crawler with the flow path of the removed portions of the plug.

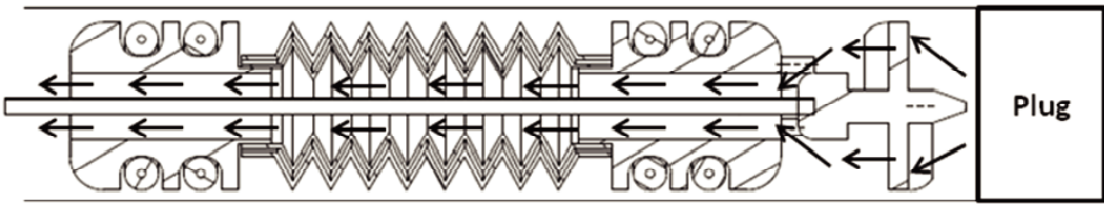

Figure 17. Section view of crawler with an auger attachment.

Principles of Motion

The device propels itself by the pressurization/depressurization sequence of the flexible cavities (balloons) located at the font, center, and back of the unit. Individual pressurization of the front or back cavities results in anchoring the system to the pipeline. This is a result of the linear relationship between the normal force imposed by the balloon on the inner surface of the pipeline and the resulting friction force.

The sequence of motion starts by inflating the rear cavity of the unit to anchor the device to the pipeline. The center cavity is then inflated to increase its volume which pushes the front end of the unit forward. Finally, the front cavity of the unit is inflated and then the center and rear cavities are deflated to complete once cycle of peristaltic motion.

Overview of Pneumatic/Hydraulic Control Systems

As noted previously, the motion of the crawler is powered by pressurizing air into flexible cavities. Figure 18 shows the basic schematic of how the hydraulic system is used to propel the crawler. Pressurized air is provided from an air reservoir and is regulated down to the desired maximum pressure of the system (REG 4). The pressure is then directed to the manifold consisting of 3 valves controlled via a computer. Additionally, vacuum pressure is provided to the manifold. The position of each of the valves determines whether positive pressure or vacuum pressure is provided to each of the lines that power the cavities of the crawler (C_LINE 1, C_LINE 2, C_LINE 3). The sequence in which the valves are activated/deactivated dictates the forward or backward motion of the crawler in the pipeline.

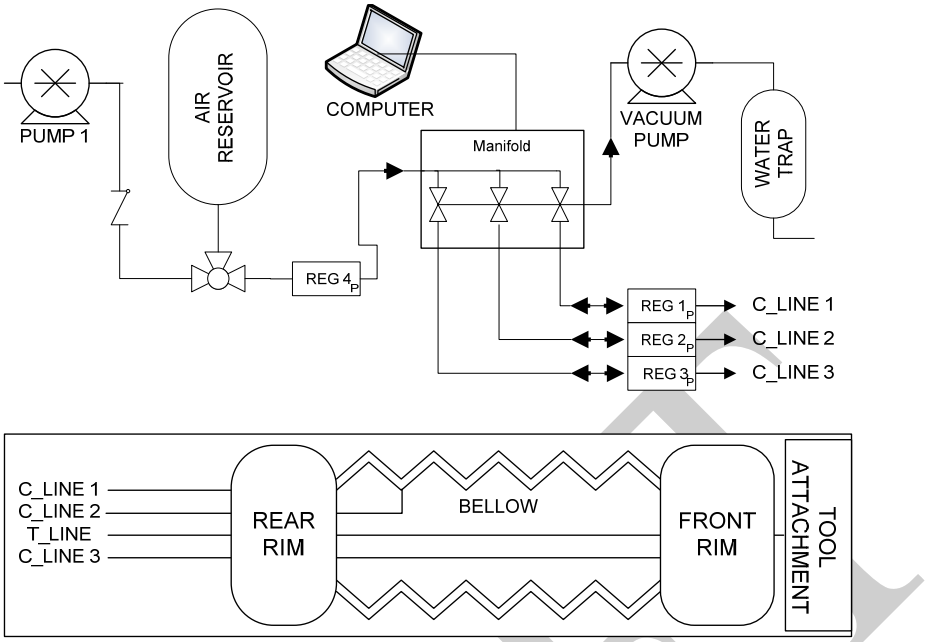

Figure 18. Schematic of pneumatic system for the crawler.

The unplugging tool attached to the front of the unit is power by pressurized water. Figure 19 shows a schematic of the hydraulic system utilized to perform the unplugging operations. The tether being pulled by the crawler includes the hydraulic line (T_Line) which is connected to the tool attachment.

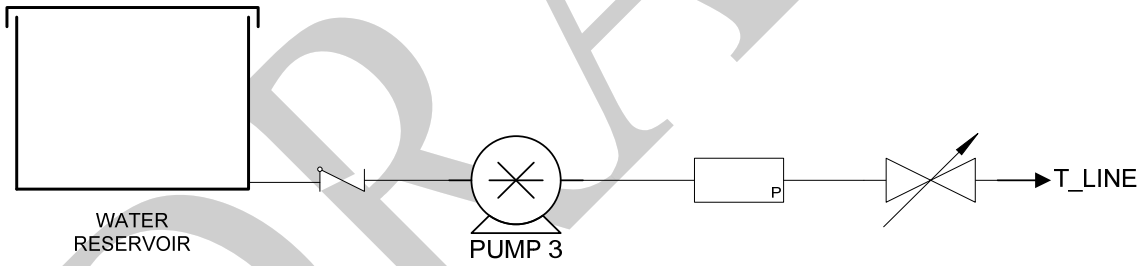

Figure 19. Pneumatic system to power unplugging attachment.

First Generation Peristaltic Crawler

To experimentally test the principles of motion described during the proof of concept phase of the project, a first generation crawler was designed, assembled and tested. The first generation crawler consisted of two concentric wire-reinforced rubber bellows attached to aluminum cylindrical rims. One rubber sleeve slid over each of the rims to define the front and back balloon. All the parts were held together by metal clamps. Figure 20 shows a side view of the first generation peristaltic crawler.

Figure 20. Side view of first generation crawler.

The preliminary testing of the first generation crawler consisted on evaluation its motion on a 10 ft clear PVC pipe, ability to turn around a 90° elbow and maximum pulling force. The crawling speed of the unit was dependent upon two factors: the distance that it travels with every expansion and the speed at which it can expand or contract the rims and bellows. With the dimensions of the prototype, the difference between the collapsed and extended lengths was 5 inches. This means that regardless of how fast the crawler expands or contracts, it can only gain five inches per cycle. Small leakages in the prototype crawler likely reduced the recorded speed of the unit. The crawler proved to navigate through a 90° elbow efficiently. The maximum pulling force archived by the prototype during preliminary testing was 27.3 lbs. The maximum pressure of the system was 30 psi of air.

The unplugging ability of the first generation crawler was evaluated by assembling a testbed containing a 3 ft bentonite clay plug. The unit was then directed to the plug location and a 15° hydraulic nozzle mounted at the front of the unit was activated to begin the unplugging procedure. Initially, the face of the plug closest to the unit was eroded and the removed plug travelled efficiently through the crawler. However, as the distance between the water nozzle and plug face increased, only partial areas of the plug were removed. It was also noted that during a long unplugging procedure, the seals holding the parts together did not function properly and leaks occurred.

Second Generation Peristaltic Crawler

Applying the lessons learned from the first generation peristaltic crawler, an improved unit was designed, assembled and tested. The improvements focused on three areas: 1) increasing the maximum allowable pressure inside the bellow, 2) creating a more durable unit and 3) automating the controls for the crawler.

Bellows Tested for the SGPC

The material chosen for the bellow of the SGPC was stainless steel, due to its durability in HLW environments. There are two variations commercially available for this type of bellow: edge-welded bellows and hydro-formed bellows. Edge-welded bellows are assembled by welding thin stainless steel leafs to create each convolution. This process uses a welding procedure that is expensive and requires custom made molds and fixtures. Figure 21A) shows an example of an edge-welded bellow. Figure 21B) shows a cross section view of the welded leafs of an edge-welded bellow. Hydro-formed bellows are manufactured by welding a stainless steel thin plate to create a hollow cylinder that is then deformed plastically using an internal mandrill and an external mold. These deformations define the convolutions of the bellow. Figure 21C) shows an example of hydro-formed bellow.

Each of the manufacturing techniques produces a stainless steel bellow with different mechanical properties. The edge-welded bellow provides superior flexibility and expansion/contraction ratio but it does not allow for internal pressurization. On the other hand, the hydro-formed bellow has a spring ratio which increases exponentially with a decrease in the bellow diameter, making it harder for it to turn a 90° elbow but can be internally pressurized to relatively high pressures. For the SGPC, both types of bellows were studied and it was concluded that for our purposes, the hydro-formed bellow provides the best choice for the outer bellow.

A)  B) 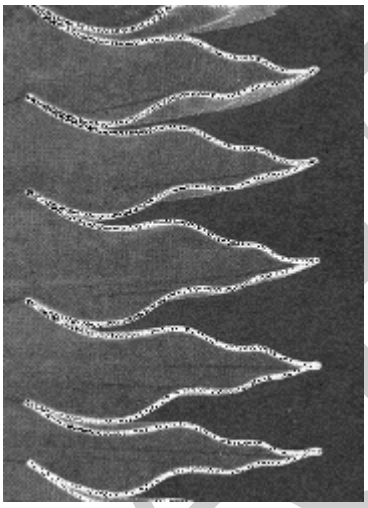 C) 

Figure 21. A) Edge-welded bellow B) detail cross section of edge-welded below C) hydro-formed bellow.

Bellows having dimensions compatible with those found in the pipeline at DOE sites were procured and their response to pressurization was tested. The bellow selected was the KF-40 from Ideal Vacuum Products which was 10 inches in length. Its bursting pressure was tested by submerging the bellow in a water tank and increasing the air pressure. It was found that the bellow could withstand a pressure of 150 psi but demonstrated plastic deformation as the elongation of the bellow reached 15 inches (Figure 22). This test showed that the bellow's maximum extension from its 1 atmosphere position should not exceed 1 inch.

Figure 22. Burst pressure test on hydro-formed bellow.

Following, an assembly comprised of two concentric hydro-formed bellows (one of smaller diameter) were welded together to create the double walled bellow. Its response was tested to determine the changes in length under vacuum pressure (Figure 23). It was determined that the assembly could retract to a maximum of 1.5 inches. The combination of the burst test and the vacuum test provides an accurate estimate of the reaction response of the bellow assembly.

Figure 23. Double walled bellow assembly contracted due to vacuum pressure.

Improvements of Front and Back Cavities

During the experimental testing of the first generation crawler, the primary factor that caused failure of the unit was the slippage or rupture of the flexible cavities. To correct the problem the rims and bellow of the SGPC are held together with the use of flanges and bolts. Additionally, different material and material thicknesses were tested to improve the crawler's durability. Figure 24A) shows a 0.25 in thick natural rubber membrane tested to 60 psi. Figure 24B) shows a 0.25 in thick flexible PVC membrane tested to 60 psi. These tests provided the required parameters to determine the expansion in diameter resulting from pressurizing of the front and back cavity.

A)  B) 

Figure 24. A) Natural rubber pressurize cavity, B) flexible PVC pressurize cavity.

To mitigate the possibility of leaks resulting from slippage of the flexible membranes from the clamps, the front and back rim were designed with grooves to accommodate 3/8 in wide stainless steel clamps. Figure 25A) shows the front rim prior to assembly. Figure 25B) shows the assembled front rim pressurized to 30 psi using a flexible PVC sleeve.

A)  B) 

Figure 25. A) Rim showing grooves for clamps, B) front rim assemble and pressurized.

Control Unit for the SGPC

An additional improvement implemented to the SGPC was the automation of the sequence of inflation/deflation of the cavities and bellow that dictates the forward and backward motion of the crawler. The pneumatic valves that direct the pressure or vacuum source to the crawler were connected to a programmable logic controller, OMRON ZEN-10C1AR-A-V2. By programming an appropriate sequence and timing of the opening and closing of the valves, the desired motion was achieved. Figure 26A) shows a screen capture of the software during forward motion. The programmable controller is incased in an air-tight fiberglass box that provides control of the unit via switches and a joystick. As shown on Figure 26B), the control station contains the regulator, electronics, and pneumatic controls that direct the pressure or vacuum of air into the unit.

B)

A) 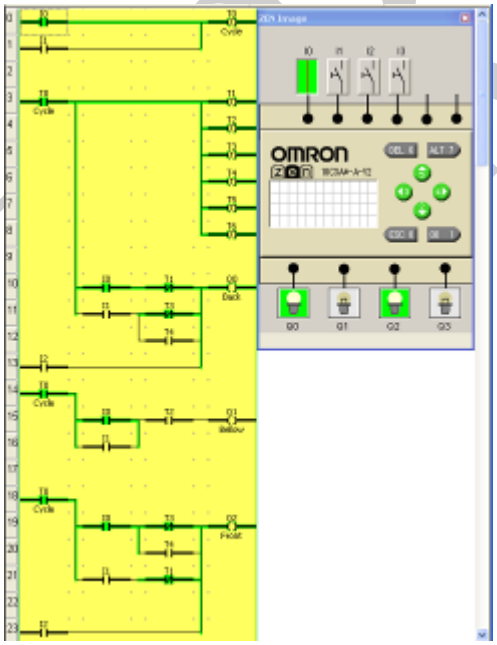

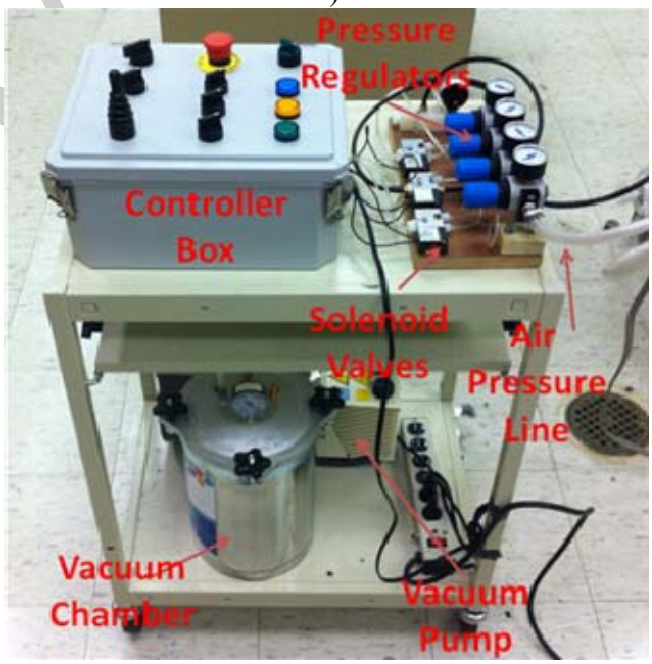

Figure 26. A) Screen capture of OMRON software, B) control unit and pneumatic system to control SGPC.

Pipeline Unplugging Attachments

During this evaluation phase, two unplugging attachments were tested. One was a high pressure rotating nozzle manufactured by Arthur Products Co with (Part# AP0062SJ-01). The second was a stationary high pressure 15° nozzle. Both of the unplugging attachments were powered using pressurize water at 2200 psi with a flow rate of 2.3 GPM. The rotating nozzle was designed with 3 orifices: 2 at a 45° angle forward of the crawler and 1 positioned directly forward to the crawler. Figure 27A) shows the rotating nozzle and B) shows the 15° nozzle.

A)  B) 

Figure 27. A) Rotating nozzle attachment, B) 15° nozzle attachment.

RESULTS - SECOND GENERATION PERISTALTIC CRAWLER

Experimental Testing of the SGPC

Pressurization and Sequencing Test

The unit was initially placed in a clear PVC pipe so that the cavities could be safely pressurized to different limits to find the optimal operational pressure with no load. The optimal pressure for the front and back cavities was 90 psi. The optimal pressure for the bellow was 20 psi. The sequencing of the inflation/deflation of the unit was controlled using a programmable logic controller. Several programs were tested to find a sequence that allowed full inflation and deflation of the cavities in a minimum time. Using the pressures previously presented, the optimal cycle time was found to be 16 seconds.

Crawler Speed Test

The speed of the crawler was measured using an 80 in long pipeline that was 3 inches in diameter. Figure 28 shows the setup of the clear PVC pipe used. Tests were conducted for a dry pipeline and then for a pipeline flooded with water. The shortest time recoded for the dry pipeline was 12 minutes 51 seconds. The shortest time for the flooded pipeline was 13 minutes and 22 seconds. Using these results, the approximate speed of the crawler in straight pipe was 0.5 ft/min.

Figure 28. Testbed used for the speed test.

Maneuverability Test

The crawler's ability to negotiate through elbows was tested on a testbed constructed using two straight 3 in pipes and one 90° elbow. It was found that the crawler could not turn in a Victaulic elbow (4.25 inches in radius) but it was able to turn in a PVC elbow having a radius of 5.6 inches. The time recorded for the crawler to clear the elbow was 7 minutes and 34 seconds. Figure 29 shows the sequence of the crawler turning on the 90° elbow.

Figure 29. Sequence of crawler turning through an 90° elbow.

Pulling Force Test

The pulling force test was conducted using a spring scale connected to a frame holding a clear PCV pipe (see Figure 30). Two trials of test were conducted, each one with a different spring scale. By using scales with different spring constants it was possible to determine the effect that the extension of the bellow has on the pulling force. The scales used were 1 in displacement per 13 lbs and 1 in displacement per 67 lbs. The maximum pulling force recorded was 110 pounds at 90 psi of pressure inside the bellow with an extension of the bellow of 1.64 inches. Figure 31 shows the results from the results using each spring scale.

Figure 30. Testbed used to measure the pulling force.

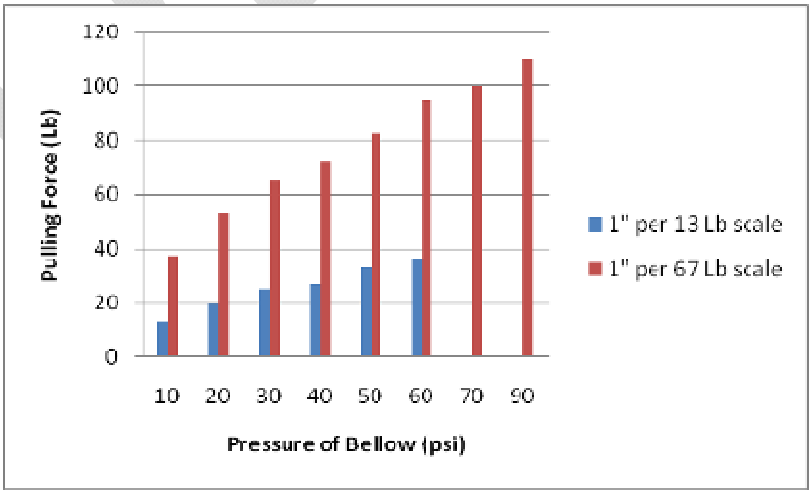

Figure 31. Pulling force vs. bellow pressure.

Unplugging Test

The unplugging tests were performed using two types of nozzles: a rotating nozzle having orifices oriented at 45° and a stationary nozzle having a 15° angle. The rotating nozzle was tested on a bentonite plug and was only able to erode away 2.5 inches of the face of the plug. The 15° nozzle was successful in performing the unplugging of a 3 ft bentonite plug in 56 minutes.

Additionally, the 15° nozzle was tested on a short sodium aluminum silicate plug. A 4.25 in length plug was fabricated inside a 3 in carbon steel pipe. The pipe was coupled to a clear PVC pipe so that the plug removal could be partially observed. Figure 32(a) shows the setup and waste collection structure used to perform the unplugging operation. The time required for unplugging was 6 minutes. Figure 32 (b) shows the pipe section after the unplugging operation.

Figure 32. (a) Setup used to perform the sodium-aluminum-silicate unplugging test, (b) pipe after unplugging operation.

CONCLUSIONS

Two technologies have continued to be developed and evaluated during the last period of performance. This includes APS and a peristaltic crawler.

Results from parametric testing of the APS showed for a fully flooded pipeline, the maximum pressure differential (260 psi) was developed applying the pulse with the following conditions: the hydraulic system set to 500 psi, the valve open 100%, and the valve open time set to 5 seconds. The trend for all pressure differentials indicated that percentage of the valve opening was the variable that had the strongest effect in the resulting pressure differential. An additional observation from the testing was that there was little degradation for the sine wave pulse in a fully flooded pipe, from the inlet to the plug. The lack of degradation in the signal was expected.

For frequencies higher than 2 Hz, asynchronous pulsing was not achieved. As the system became highly dynamic, it was not possible to control the positions of the cylinders to provide the desired response. This is likely due to performance limitations with one of the cylinders. This will be verified and remedied during the next performance period. Additionally, tandem pistons having a piston face ratio other than 1:1 could be used since the hydraulic unit operates best at higher pressures. This would improve the performance of the cylinder without exceeding the maximum pressure in the pipeline of 300 psi.

The pulse profile (sine or square) did not show a significant difference in the maximum pressure differential or vibration achieved. Further investigation is required to study the effects of the pulse profile on the plug/pipeline interaction.

For the water column vibration tests, only trials with the hydraulic oil set to 300 psi and 25% air demonstrated a significant increase in vibration response. Further investigations will be needed to determine whether water column resonance is a viable method for pipeline unplugging.

It was determined that the primary factor that limited the ability of the crawler to navigate through a 90° elbow was the stiffness of the bellow. Data from the manufacturer on hydro-formed bellows shows that the spring rate of the bellow dramatically increases as the diameter of the bellow decreases. The outer bellow used in the current design has a spring rate of 1.9 lb/in and the inner bellow had a spring rate of 27 lb/in. The high spring rate of the inner bellow made the bellow assembly more rigid and limited its ability to navigate through a 90° elbow. This high spring rate also affects the speed of the crawler since it requires higher vacuum to achieve the bellow's contraction.

For future versions of the crawler, different bellow designs that can provide a more optimal response will be investigated. One possibility is the using an edge-welded bellow for the inner bellow. Implementing this change will eliminate the spring rate for the inner bellow providing a more flexible assembly.

Another factor that affects the speed of the crawler is the diameter of the air line that is connected to the bellow. Test showed that using a 25 ft line with a 1/16 in diameter provided full contraction of the bellow in approximately 2.5 minutes whereas using a 0.17 in diameter line contracts the bellow in 8 seconds. Further investigation is required to determine the effect of minor loses in the crawler speed. The speed test showed that having a dry or wet pipeline does not have a significant effect on the speed of the crawler.

The pull force test showed that the extension of the bellow affects the available pulling force of the crawler. The maximum pulling force (110 lbs) was obtained with a displacement of 1.64 in. Results from the pulling test could be further analyzed to characterize the response of the bellow and also to determine the effective frontal area of the bellow.

The unplugging operations showed that the rotating nozzle does not provide enough water pressure to erode a bentonite plug. The cause of the loss in water pressure could be attributed to using a rotating nozzle of a small diameter (1/16 in). Further test using a rotating nozzle having the same diameter as the stationary nozzle (1/2 in) will be conducted to determine the effect that the nozzle diameter has in unplugging ability. The 15° nozzle proved effective in unplugging aluminum sodium silicate plugs. The waste from this type plug showed no constriction of flow through the crawler.

REFERENCES

1. Zollinger, W., & Carney, F. (2004). Pipeline blockage unplugging and locating equipment. *Conference on Robotics and Remote Systems- Proceedings*, (pp. 80 - 85). Gainesville.
2. Shishido Yoshio. United States Patent #5,090,259. Pipe-inspecting apparatus having a self propelled unit. Feb, 1992
3. Sollinger. United States Patent #5,758,731. Method and apparatus for advancing tethers. Jun, 1998.

TASK 12 FY10 YEAR END TECHNICAL REPORT Multiple-Relaxation-Time Lattice Boltzmann Model for Multiphase Flows

EXECUTIVE SUMMARY

The U.S. Department of Energy (DOE) Hanford Site is in need of computer software that can be used as a tool for understanding the physics of fluid flow in nuclear tanks during regular operations and retrieval tasks. Bubble generation due to chemical reactions and sludge mixing via air-bubble-lifters is an example of fluid-dynamics problems that must be investigated using accurate computer simulations to predict performance and avoid possible safety issues. In 2009, a new task was initiated as part of Florida International University's (FIU's) research efforts in order to develop a computational program, which is based on the lattice Boltzmann method (LBM) in order to simulate multiphase flow problems related to high-level waste (HLW) operations. In 2009, a thorough literature review was conducted to identify the most suitable multiphase fluid modeling technique in LBM and a single-phase multi-relaxation-time (MRT) code was developed. During this performance period, FIU identified and evaluated a multiphase LBM using a single-relaxation-time (SRT) collision operator and updated the collision process with the computer program with a MRT collision model. In this report, the findings of the multiphase LBM computer program with SRT and MRT collision operators are presented and the verification of the multiphase LBM computer code is shown for various fluid flow problems. For static bubbles, it was found that the SRT and MRT multiphase LBM were successful in capturing the surface tension force at the interface while the MRT results showed a slight increase in spurious velocities. In terms of dynamic bubbles, the bubble shapes obtained with the SRT and the MRT LBMs were found to be different caused by the relaxation parameters used in the MRT method. The accuracy of the two methods will be analyzed against analytical solutions of multiphase channel flow problem as future work.

INTRODUCTION

As a result of atomic weapons production, millions of gallons of radioactive waste was generated and stored in underground tanks at various DOE sites. DOE is currently in the process of transferring the waste from single shell tanks to double shell tanks, during which various waste retrieval and processing methods are being employed. The storage and mixing of the liquid waste requires understanding the hydrological and rheological properties of the fluid inside the waste tanks. The fluid inside the waste tanks is comprised of multiple phases in which bubble dynamics plays an important role. Gas bubbles can exist in the waste entrapped in the liquid phase, inside cracks within the solid waste or on the surface of the tank walls. They can also be generated inside the waste naturally caused by chemical reactions such as hydrogen production or can be externally supplied via mechanical mechanisms such as air-purging, pulsed-air mixing etc.

An understanding of the physical nature of bubble dynamics inside the waste and the effects of the air release process to the tank environment need to be gained by considering various waste conditions. Such an analysis can be made possible by developing a numerical method that can simulate the process of air bubble generation inside tanks and that can track accurately the interactions of the gas phase with the surrounding fluid and solid phases. The final computational program would serve as a tool for Site engineers and scientists to predict waste behavior and improve operational procedures during the storage, handling and transfer of liquid waste.

In this report, a numerical method, the lattice Boltzmann method (LBM), is presented, which can model multiphase flows accurately and efficiently. LBM is advantageous over traditional Navier-Stokes based computational models since surface forces are handled more effectively in LBM. LBM has been mostly employed using the Bhatnagar-Gross-Krook (BGK) collision operator with a single-relaxation-time to simulate multiphase flows. This has brought a limitation when the fluid viscosity is low, which makes the LBM simulations unstable. In order to avoid instability issues, multiple-relaxation-time (MRT) lattice Boltzmann models were proposed that use a collision operator that can adjust the bulk and shear viscosities independently. In addition, two-phase flows with high density ratios brings a computational challenge in terms of numerical instabilities to LBM simulations for multiphase flows with density ratios larger than 10. The instability is considered to be generated as a result of large pressure gradients in the interfacial region between two phases. Feasibility of SRT and MRT LBMs for multiphase flow simulations is investigated in this report.

The outline of the report is given as follows: first, the lattice Boltzmann method using the single relaxation time for the collision term is introduced in relation to the multiphase flows. Later, multiple relaxation time based lattice Boltzmann methods for multiphase flows are discussed. Verification cases for various laminar multiphase flow problems are presented using SRT and MRT LBMs. The results obtained are compared against analytical solutions. Finally, conclusions are drawn and discussions for future work are presented.

Numerical method

The lattice Boltzmann method developed for this task is based on the continuous Boltzmann equation given by

$$\frac{\partial f}{\partial t} + \boldsymbol{\xi} \cdot \nabla f + \boldsymbol{F} \cdot \nabla_{\xi} f = \Omega. \tag{1}$$

Here f is the single particle density distribution function, $\boldsymbol{\xi}$ is the particle velocity, $\boldsymbol{F}$ is the interfacial force and Ω is the collision term. The term $\nabla_{\xi} f$ can be approximated as,

$$\nabla_{\xi} f \approx \nabla_{\xi} f^{eq} = -\frac{\xi - \mathbf{u}}{\rho c_s^2} f^{eq}, \tag{2}$$

where f^{eq} is the equilibrium density distribution function, $\mathbf{u}$ is the macroscopic velocity, ρ is the density and c_s is the speed of sound. The continuous Boltzmann equation given in Eq. (1) can be discretized in the velocity space by expressing as

$$\frac{\partial f_{\alpha}}{\partial t} + \boldsymbol{\xi_{\alpha}} \cdot \nabla f_{\alpha} = \Omega + S_{f\alpha}, \tag{3}$$

where

$$e_{\alpha} \equiv \xi_{\alpha} = \begin{cases} (0,0) & , \quad \alpha = 0, \\ (\cos(\alpha - 1)\pi/2\,, \sin(\alpha - 1)\pi/2) & , \quad \alpha = 1,2,3,4 \\ \sqrt{2}(\cos\left(\frac{(\alpha-5)\pi}{2} + \frac{\pi}{4}\right), \sin\left(\frac{(\alpha-5)\pi}{2} + \frac{\pi}{4}\right)) & , \quad \alpha = 5,6,7,8 \end{cases} \tag{4}$$

and

$$S_{f\alpha} = \frac{(e_{\alpha i} - u_i)F_i}{\rho c_s^2} f_{\alpha}^{eq}. \tag{5}$$

In Eq. (4) α is the discrete particle velocity distribution using the D2Q9 lattice structure shown in Figure 33, *e* is the particle velocity between lattice points.

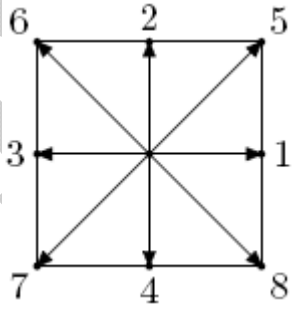

Figure 33. D2Q9 lattice structure.

In SRT LBM, the collision term Ω is represented using the BGK model that uses a single relaxation time parameter (λ), $\Omega_c = -\left(\frac{f_{\alpha} - f_{\alpha}^{eq}}{\lambda}\right)$. In the MRT LBM, using a collision matrix Λ, the collision term on the right hand side of Eq. (3) is represented by

$$\Omega = -\Lambda_{\alpha\beta}\left(f_{\beta} - f_{\beta}^{eq}\right). \tag{6}$$

The equilibrium distribution function, f_{α}^{eq}, is written as

$$f_\beta^{eq} = w_\alpha \rho \left[1 + \frac{e_{\alpha i} u_i}{c_s^2} + \frac{(e_{\alpha i} e_{\alpha j} - c_s^2 \delta_{ij}) u_i u_j}{2 c_s^4}\right], \tag{7}$$

where w_α is the weight function given by

$$w_\alpha = \begin{cases} 4/9, & \alpha = 0, \\ 1/9, & \alpha = 1,2,3,4, \\ 1/36, & \alpha = 5,6,7,8. \end{cases} \tag{8}$$

The force F_i in Eq. (5) is responsible for phase separation and is given by

$$F_i = \frac{\partial}{\partial x_j}(\rho c_s^2 - P)\delta_{ij} + \kappa \rho \frac{\partial}{\partial x_i} \frac{\partial^2 \rho}{\partial x_j \partial x_j}. \tag{9}$$

Here, P is the pressure and κ is the surface tension parameter which is related to the surface tension σ through the relation

$$\sigma = \kappa \int \left(\frac{\partial \rho}{\partial r}\right)^2 dr\,, \tag{10}$$

where r is the direction of integration normal to the interface. The force F_i is expressed by Lee and Lin [3] as

$$F_i = \frac{\partial \rho c_s^2}{\partial x_j}\delta_{ij} - \rho \frac{\partial}{\partial x_i}\left(\frac{\partial E_f}{\partial \rho} - \kappa \frac{\partial^2 \rho}{\partial x_j \partial x_j}\right). \tag{11}$$

E_f is the excess free energy at the interface over the bulk free energies and is obtained from an equation of state (EOS) expressed as follows (Lee & Lin, 2005):

$$E_f(\rho) \approx \beta\left(\rho - \rho_g^{sat}\right)^2 (\rho - \rho_l^{sat})^2\,, \tag{12}$$

where β is a constant and ρ_g^{sat} and ρ_l^{sat} are densities of gas and liquid phases at saturation, respectively. This EOS results in a density profile given by

$$\rho(z) = \frac{\rho_l^{sat} + \rho_g^{sat}}{2} - \frac{\rho_l^{sat} - \rho_g^{sat}}{2} \tanh\left(\frac{2z}{D}\right), \tag{13}$$

where z is the spatial location normal to the interface and D is the interface thickness.

The constant β along with κ can control D and σ through the relation

$$D = \frac{4}{\left(\rho_l^{sat} - \rho_g^{sat}\right)} \sqrt{\frac{\kappa}{2\beta}}, \tag{14}$$

and

$$\sigma = \frac{\left(\rho_l^{sat} - \rho_g^{sat}\right)^3}{6} \sqrt{2\kappa\beta}. \tag{15}$$

The evolution equations given above for the particle density distribution function is mapped into the moment space by multiplying the terms in Eq. (3) with the transformation matrix $\boldsymbol{T}$

$$\boldsymbol{T}^T = \left[\langle\rho|, \langle e|, \langle e^2|, \langle j_x|, \langle q_x|, \langle j_y\right|, \langle q_y|, \langle p_{xx}|, \langle p_{xy}|\right], \tag{16}$$

where

$$|\rho\rangle = |e_\alpha|^0, \tag{17}$$

$$|e\rangle_\alpha = -4|e_\alpha|^0 + 3(e_{\alpha,x}^2 + e_{\alpha,y}^2), \tag{18}$$

$$|e^2\rangle_\alpha = 4|e_\alpha|^0 - \frac{21}{2}(e_{\alpha,x}^2 + e_{\alpha,y}^2) + \frac{9}{2}(e_{\alpha,x}^2 + e_{\alpha,y}^2)^2, \tag{19}$$

$$|j_x\rangle_\alpha = e_{\alpha,x}, \tag{20}$$

$$|q_x\rangle_\alpha = \left[-5|e_\alpha|^0 + 3(e_{\alpha,x}^2 + e_{\alpha,y}^2)\right]e_{\alpha,x}, \tag{21}$$

$$\left|j_y\right\rangle_\alpha = e_{\alpha,y}, \tag{22}$$

$$\left|q_y\right\rangle_\alpha = \left[-5|e_\alpha|^0 + 3(e_{\alpha,x}^2 + e_{\alpha,y}^2)\right]e_{\alpha,y}, \tag{23}$$

$$|p_{xx}\rangle_\alpha = e_{\alpha,x}^2 - e_{\alpha,y}^2, \tag{24}$$

$$\left|p_{xy}\right\rangle_\alpha = e_{\alpha,x}e_{\alpha,y}. \tag{25}$$

The resulting evolution equation in moment space takes the form

$$\frac{\partial \hat{f}_\alpha}{\partial t} + \hat{\boldsymbol{\xi}}_{\boldsymbol{\alpha}} \cdot \nabla \hat{f}_\alpha = -\hat{\Lambda}_{\alpha\beta}\left(\hat{f}_\beta - \hat{f}_\beta^{eq}\right) + \hat{S}_{f\alpha}, \tag{26}$$

where

$$\hat{f}_\alpha = \boldsymbol{T} f_\alpha, \tag{27}$$

$$\hat{f}_\alpha^{eq} = \boldsymbol{T} f_\alpha^{eq}, \tag{28}$$

$$\hat{S}_{f\alpha} = \mathbf{T} S_{f\alpha}, \tag{29}$$

and

$$\hat{\Lambda} = \boldsymbol{T}\Lambda\boldsymbol{T}^{-1}. \tag{30}$$

The equilibrium distribution function in moment space is written as

$$(\hat{f}^{eq})^T = \left[\rho, e^{eq}, (e^2)^{eq}, j_x, q_x^{eq}, j_y, q_y^{eq}, p_{xx}^{eq}, p_{xy}^{eq}\right], \tag{31}$$

where the equilibrium distributions of the moments are given by

$$e^{eq} = \frac{1}{4}\alpha_2\rho + \frac{1}{6}\gamma_2(j_x^2 + j_y^2)/\rho, \tag{32}$$

$$(e^2)^{eq} = \frac{1}{4}\alpha_3\rho + \frac{1}{6}\gamma_4(j_x^2 + j_y^2)/\rho, \tag{33}$$

$$q_x^{eq} = \frac{1}{2}c_1 j_x, \tag{34}$$

$$q_y^{eq} = \frac{1}{2}c_1 j_y, \tag{35}$$

$$p_{xx}^{eq} = \frac{3}{2}\gamma_1\left(j_x^2 - j_y^2\right)/\rho, \tag{36}$$

$$p_{xy}^{eq} = \frac{3}{2}\gamma_3(j_x j_y)/\rho. \quad (37)$$

The constants in Eqs. (23-28) are selected as $\alpha_2 = -8$, $\alpha_3 = 4$, $c_1 = -2$, $\gamma_1 = \gamma_3 = 2/3$, $\gamma_2 = 18$ and $\gamma_4 = -18$.

The collision matrix in the moment space, $\hat{\Lambda}$, is given as

$$\hat{\boldsymbol{\Lambda}} = diag[s_1, s_2, s_3, s_4, s_5, s_6, s_7, s_8, s_9]. \quad (38)$$

The diagonal elements are inverses of relaxation times for the distribution functions in the moment space, $\hat{f}_\alpha$, and they are used to relax the equilibrium distribution functions in the moment space, $\hat{f}_\alpha^{eq}$. In this work, the diagonal elements are selected as $s_1 = s_4 = s_6 = 1$, $s_2 = 1.64$, $s_3 = 1.54$, $s_5 = s_7 = 1.7$. The parameters s_8 and s_9 are related to the single relaxation time, τ, in the single-relaxation-time LBM ($s_8 = s_9 = 1/\tau$) and are used to determine the viscosity, $\nu = \frac{1}{3}\left(\frac{1}{s_9}\right)$ and the Reynolds number, $Re = UD/\nu$.

As discussed in Lee and Lin [3], it is possible to compute the hydrodynamic variables of interest such as local density ρ, velocity $\boldsymbol{u}$, and pressure P, from f_α. This approach, however, is prone to numerical instabilities due to the steep density gradients involved in the computation of the source term $S_{\alpha\beta}$. Therefore, a separate distribution function g is introduced to compute pressure and momentum. We denote g in the lattice velocity direction α as g_α. A pressure function p is also defined, which varies smoothly across the interface. It is related to the actual pressure P through

$$p = P - \kappa\rho\frac{\partial^2\rho}{\partial x_k \partial x_k} + \frac{\kappa}{2}\frac{\partial\rho}{\partial x_k}\frac{\partial\rho}{\partial x_k}. \quad (39)$$

In the bulk phase, $p \cong P$ as density gradients are nearly zero. Use of p in the momentum equation increases the stability of the scheme at high density ratios. This definition of P and the choice of D in Eq. (13) are critical to the capability of the model to simulate high density ratios. Based on the definition of p in Eq. (39), Eq. (9) for F_i may be re-arranged as

$$F_i = \frac{\partial}{\partial x_j}(\rho c_s^2 - p)\delta_{ij} + \kappa\frac{\partial}{\partial x_j}\left(\frac{\partial\rho}{\partial x_k}\frac{\partial\rho}{\partial x_k}\delta_{ij} - \frac{\partial\rho}{\partial x_i}\frac{\partial\rho}{\partial x_j}\right). \quad (40)$$

However, within this framework of the MRT model, the pressure evolution equation must now be formulated to have a non-diagonal collision matrix.

To develop an evolution equation for pressure in moment space that is similar to Eq. (26), Lee and Lin proposed

$$\hat{g}_\alpha = \hat{f}_\alpha + \left(\frac{p}{c_s^2} - \rho\right)\hat{\Gamma}_\alpha(0)\,, \quad (41)$$

where

$$\hat{g}_\alpha = \mathrm{T}g_\alpha\,, \quad (42)$$

$$\Gamma_\alpha(\mathrm{u}) = \frac{f_\alpha^{eq}}{\rho}, \quad (43)$$

and

$$\hat{\Gamma}_\alpha(0) = \mathrm{T}\hat{\Gamma}_\alpha(0)\,. \tag{44}$$

From Eq. (41), the total derivative of $\hat{g}_\alpha$ can be written as

$$\frac{D\hat{g}_\alpha}{Dt} = \frac{D\hat{f}_\alpha}{Dt} + \frac{1}{c_s^2}\frac{Dp}{Dt}\hat{\Gamma}(0) - \frac{D\rho}{Dt}\hat{\Gamma}(0)\,, \tag{45}$$

which can be simplified to

$$\frac{D\hat{g}_\alpha}{Dt} = \hat{\Omega}_c + \hat{S}_{g\alpha} \tag{46}$$

where

$$\hat{S}_{g\alpha} = \mathrm{T}S_{g\alpha}\,, \tag{47}$$

$$\begin{aligned} S_{g\alpha} = {} & \frac{(e_{\alpha i} - u_i)\partial_i(\rho c_s^2 - p)}{c_s^2}(\Gamma_\alpha(u) - \Gamma_\alpha(0)) \\ & + \frac{(e_{\alpha i} - u_i)\left[\kappa\partial_i(\partial_k\rho\partial_k\rho) - \kappa\partial_j\left(\partial_i\rho\partial_j\rho\right)\right]}{c_s^2}\Gamma_\alpha(u)\,, \end{aligned} \tag{48}$$

and

$$\hat{\Omega}_c = -\hat{\Lambda}_{\alpha\beta}\left(\hat{f}_\beta - \hat{f}_\beta^{eq}\right). \tag{49}$$

To express Eq. (49) as a function of $\hat{g}$ we define

$$\hat{g}_\alpha^{eq} = \hat{f}_\alpha^{eq} + \left(\frac{\rho}{c_s^2} - \rho\right)\hat{\Gamma}_\alpha(0)\,. \tag{50}$$

From this we get the following pressure evolution equation in moment space as

$$\frac{D\hat{g}_\alpha}{Dt} = -\hat{\Lambda}_{\alpha\beta}\left(\hat{g}_\beta - \hat{g}_\beta^{eq}\right) + \hat{S}_{g\alpha}\,, \tag{51}$$

The macroscopic properties of density, momentum and pressure are obtained from the following relations:

$$\rho = \sum_\alpha f_\alpha\,, \tag{52}$$

$$\rho u_i = \sum_\alpha e_\alpha g_\alpha + \int_t^{t+\delta_t} \kappa\left[\frac{\partial}{\partial x_i}\left(\frac{\partial\rho}{\partial x_k}\frac{\partial\rho}{\partial x_k}\right) - \frac{\partial}{\partial x_j}\left(\frac{\partial\rho}{\partial x_i}\frac{\partial\rho}{\partial x_j}\right)\right]dt\,, \tag{53}$$

$$p = c_s^2\sum_\alpha g_\alpha + \int_t^{t+\delta_t} u_i\frac{\partial\rho c_s^2}{\partial x_i}dt\,. \tag{54}$$

RESULTS

In the first numerical test case presented here, a circular two-dimensional bubble was generated in a fluid domain by assigning an initial density profile. The fluid domain was 101x101 lattice units (lu) in size and the bubble radius was 25 lu. The surface tension was imposed as an input parameter. The density ratio was set to 1000 and the viscosity ratio between the fluids was 100. The initial pressure field in the fluid domain was uniform; however, as the system converged to an equilibrium state, a pressure difference between the fluid domain and the gas domain was created. The relaxation of the interface between the two fluids were tested against the Laplace's law that expresses the pressure difference between the inside and the outside of a bubble as a function of the surface tension and the radius as given in two-dimensions by, $\Delta P = \sigma/R$. The difference of pressure between the inside and the outside of the bubble, P_{diff}, was computed at every time step and the relative error against the exact value is calculated as, $P_{err} = (P_{diff} - \Delta P)/\Delta P$. The convergence of P_{err} was measured at every 10 iterations by $Conv(i) = (P_{err}(i) - P_{err}(i-1))$ and the simulation was assumed to converge to a steady state result when $\varepsilon = 0.1\sum_{i=1}^{10} Conv(i) < 0.005$. A parametric study was conducted in order to understand the effect of the interface thickness, D, on the error in ΔP (Figure 34) and the maximum parasitic velocity (Figure 35).

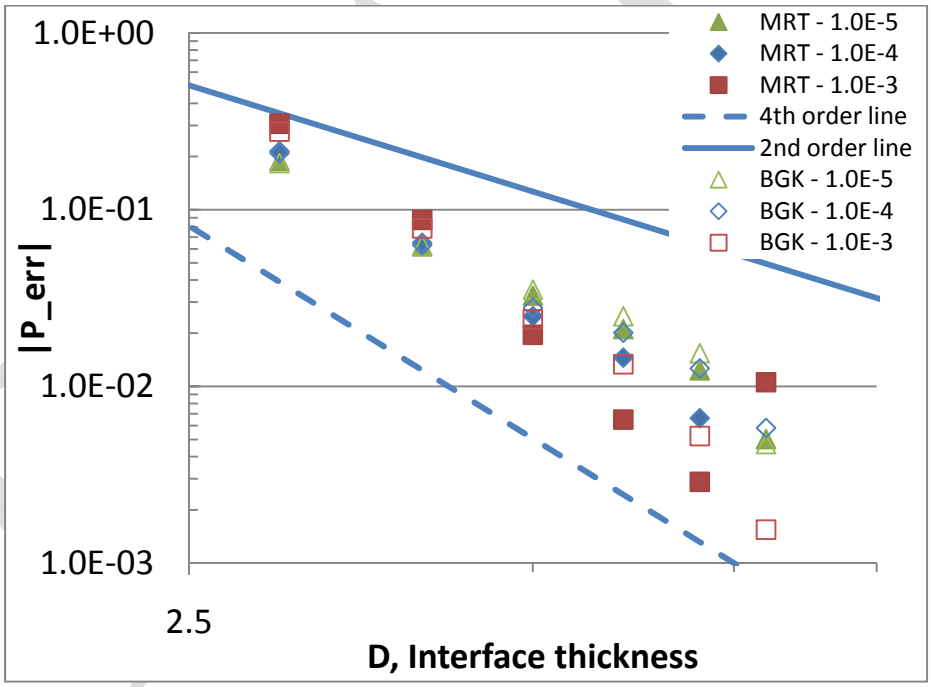

Figure 34. Effect of interface thickness on the pressure difference across the bubble interface at three different values of surface tension.

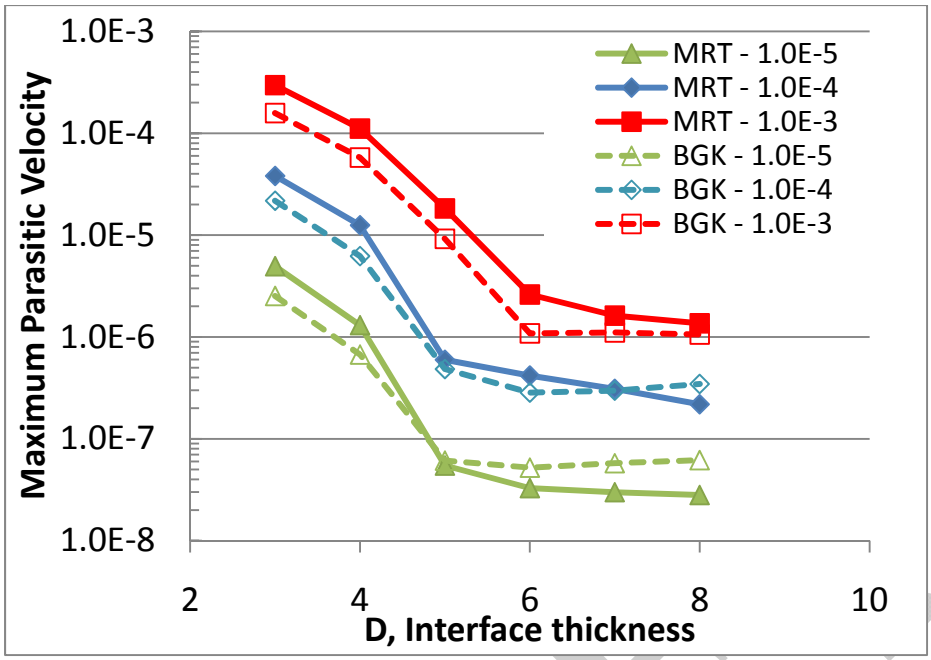

Figure 35. Effect of interface thickness on the magnitude of maximum parasitic velocity in the vicinity of the bubble interface at three different values of surface tension calculated with MRT and the BGK LBM.

The error between the pressure difference calculated by both MRT and the BGK methods and the analytical equation were found to reduce with increasing interface thickness. The BGK and the MRT results were found to be comparable.

For static bubbles a spurious or parasitic velocity field is obtained along the interface of the bubble, which is an artifact of the numerical discretization in the computational model that is used. For accurate simulations, the value of spurious velocities needs to be kept small as compared to the characteristic velocity of the problem. The parametric study presented here has shown that the maximum magnitude of parasitic velocity drops significantly with an increase in interface thickness both using MRT and the BGK method; however, the MRT method did not bring any improvement on the spurious velocity except at very low surface tensions and thick interfaces.

In the second test case presented in this study, a circular two-dimensional bubble was generated in a fluid domain by assigning an initial density profile. The fluid domain was 101x201 lattice units (lu) in size and the bubble radius was 25 lu. The surface tension was imposed as an input parameter ($\sigma = 0.2$). The density ratio was set to 10 and the viscosity ratio between the fluids was 10. Wall boundary conditions were applied at the top and bottom of the computational domain and slip wall boundary condition was applied at the sides. The gravitational force was applied by modifying the macroscoping velocity with the additional buoyancy force term, $-\rho g$.

The deformation of bubbles are characterized by the non-dimensional Eotvos (*Eo*), Morton (*M*) and Archimedes (*Ar*) numbers, which are given as

$$\mathrm{Eo}=\frac{g\Delta\rho D^2}{\sigma},\ \mathrm{M}=\frac{g\Delta\rho D^2}{\sigma},\ \mathrm{Ar}=\frac{\sqrt{gD^3}}{\upsilon}.$$

For bubbles and drops moving freely in an infinite media, Clift et al. have prepared a shape regime chart as a function of the *Eo* and *M* numbers [2]. Bhaga and Weber later updated this

chart with more specific regions [1]. For the *Eo* and *M* numbers tested in this study (*Eo* = 9, *M* = $6x10^{-4}$), the expected bubble shape is oblate ellipsoidal which was observed to be in agreement with the LBM results with the BGK method. The MRT solution resulted in an ellipsoidal bubble shape rather than an ellipsoidal cap when the same parameters were used in the MRT code as compared to the BGK (Figure 36). The difference was found to be caused by the relaxation parameters in the MRT collision matrix $\Lambda = diag[s_1, s_2, s_3, s_4, s_5, s_6, s_7, s_8, s_9]$ used in the MRT code, which were $s_1 = s_4 = s_6 = 1$, $s_2 = 1.64$, $s_3 = 1.54$, $s_5 = s_7 = 1.7$ and $s_8 = s_9 = 1/\tau$ where τ was the relaxation parameter used in the BGK code. This result is represented in Figure 36 where the MRT result using the relaxation parameters given above is shown on the left and the BGK results using a single relaxation parameter is given on the right. At the same iteration number, the bubble shape obtained using BGK is ellipsoid cap while it is ellipsoidal for MRT. The BGK method is a subset of the MRT model where all of the hydrodynamic modes are assumed to relax at the same rate. When the relaxation parameters in MRT are equal to the same parameter then the BGK collision model is obtained. The result obtained with this approach is given in the middle picture in Figure 36 which is the identical solution with the one obtained using BGK.

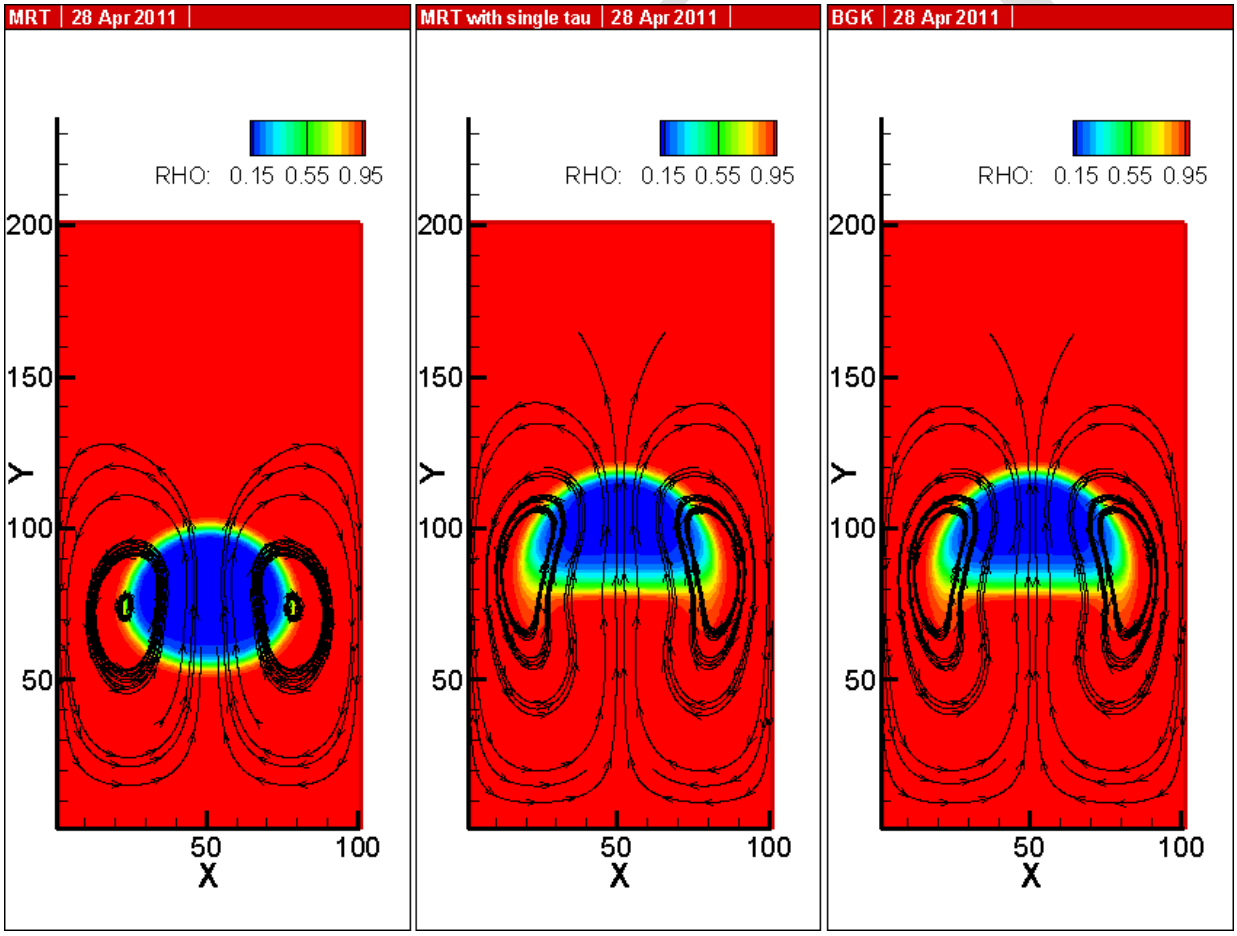

Figure 36. MRT and BGK solution for the evolution of a rising bubble at Eo=9, M=$6x10^{-4}$.

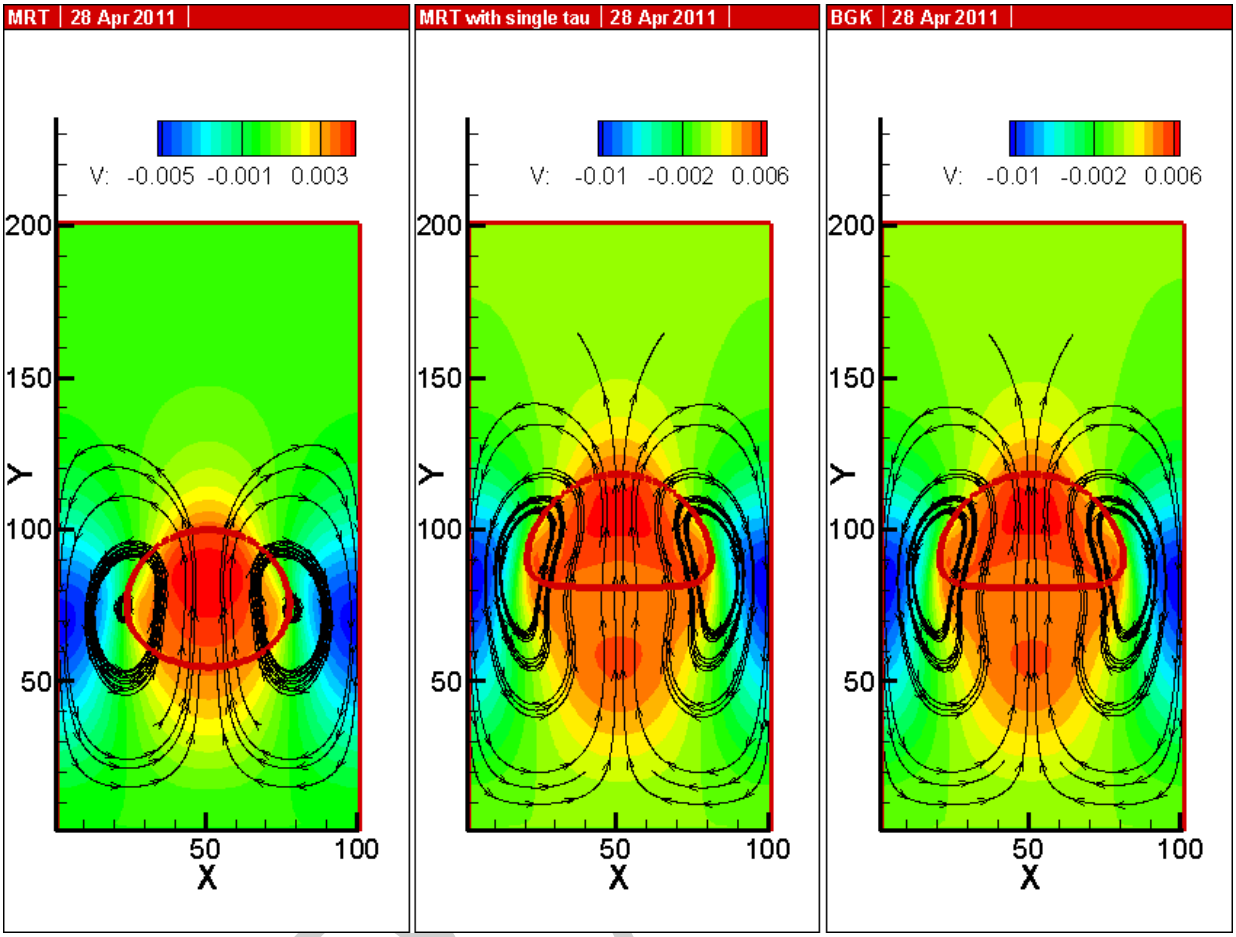

Figure 37. Vertical velocity component calculated using MRT and BGK methods.

Figure 37 shows a similar analysis for the vertical velocity field. The circulation created around the bubble and the velocity magnitude was almost identical with the BGK method and the MRT method using a single relaxation time; however, the MRT method yields a different solution when the relaxation parameters are changed to the values recommended in the literature. The vertical velocity magnitude found by the MRT method was twice as small as the BGK method.

OVERALL PROJECT CONCLUSIONS

In this study, the implementation of BGK and MRT LBMs based on the Lee and Lin multiphase model was presented for static and dynamic bubbles. The multiphase LBM shown here was found to be capable of capturing gas-fluid interactions accurately and it is advantageous that this method allows imposing fluid properties such as the surface tension and interface thickness, density and viscosities as input parameters. It was observed that the flow features related to bubble dynamics such as the bubble deformation and fluid circulation depended on the relaxation parameters used in the collision matrix. Validation cases against analytical solutions for problems such as two and three layered stratified channel flow can be used to validate the MRT and the BGK methods. The BGK results for bubble rising simulations were also found to be dependent on the liquid density value used, which brings difficulty in matching benchmark non-dimensional numbers and having similitude between the LBM results and the physical units. This issue needs to be clarified in the future as well.

REFERENCES

1. Bhaga, D., & Weber, M. (1981). Bubbles in viscous liquids: shapes, wakes and velocities. *Journal of Fluid Mechanics , 105*, 61-85.
2. Clift, R., Grace, J. R., & Weber, M. E. (2005). *Bubbles, Drops, and Particles*. Mineola: Dover Publications, Inc.
3. Lee, T., & Lin, C.-L. (2005). A stable discretization of the lattice Boltzmann equation for simulation of incompressible two-phase flows at high. *Journal of Computional Physics , 206*, 16-47.

TASK 13 FY10 YEAR END TECHNICAL REPORT Hydrodynamic Properties and Rheology of High-Level Waste Fluids

EXECUTIVE SUMMARY

The current flow sheet of the WTP includes the use of pulse jet mixers (PJMs) throughout the plant to provide adequate mixing of the process fluids. Studies conducted to date at SRS (Savannah River Site) and PNNL (Pacific Northwest National Laboratory) have addressed mostly steady state behavior of gas hold up in completely mixed fluids while transient behavior, which is significant for loss of power events, has not been much investigated. Furthermore, previous experimental work conducted at both 1/4 scale testing at PNNL and at the M12 PEP testing facility indicated abnormally slower rates of release of bubbles in low yield stress waste (lower than 5 Pa) compared to waste with yield stress greater than 5 Pa. The objective of the experimental program initiated at Florida International University was to extend previous research and address the gap of knowledge in transient behavior and abnormal rates of gas release in waste fluids with yield stress lower than 10 Pa.

Initially tests were planned with four simulants: kaolin-bentonite, AZ-101, laponite and xanthan-gum; however tests with xanthan gum and laponite were cancelled as they did not meet the site's minimum requirements of wt% of solids concentration (>20 wt%) to achieve the targeted yield stress. The experimental program used in-situ generated oxygen generated by decomposing hydrogen peroxide catalyzed by a mixture of ferrous iron and EDTA to provide data about the volumes of retained gas and the release rates from the gelled simulant. Testing with AZ-101 required some kaolin-bentonite to be mixed with it in a ratio of 1:2 as the drums sent by the site contained a batch AZ-101 mixture which caused excessively high decomposition rates of hydrogen peroxide. The bench scale experiments were carried out using mixtures of kaolin-bentonite and AZ-101 in which yield stress was the primary controlling variable. Testing with kaolin-bentonite and AZ-101 mixtures that include antifoaming agents (AFA) was also completed and the data was analyzed to investigate the effects of AFA on gas retention. The experimental work used a six foot column with diameter of six inches. The column was connected to a mass spectrometer to provide high resolution time series of gas release. The retention potential of each simulant and the signature of the released gas (such as total volume, shape, and peak intensity) were determined. The experimental data were analyzed to provide information about the equilibrium mass of oxygen contained in the gelled simulant and the initial rates of release of retained gas. The test results showed an increase in gas hold-up by 10% for clay simulants and 33% for AZ-101+clay mix simulant with the addition of AFA for tests with yield stress less than 5 Pa. About 60-90% of the gas was released in the first 20 minutes and the remaining gas within 180 minutes. The release curve was characterized by two different regions; each region had a first order decay with respect oxygen mass released. The observed faster release rate of the order of first 15 minutes was attributed to the process of mobilization and release of larger bubbles within the column contents. The slower release rate (typically next 45 minutes) was attributed to release of dissolved oxygen. The rate constants and the initial rates of release were correlated with the physicochemical properties of the simulant.

INTRODUCTION

The U.S. DOE Hanford Tank Waste Treatment and Immobilization Plant (WTP) will pretreat and vitrify the waste retrieved from underground storage tanks. The WTP consists of three primary facilities: pretreatment, low activity waste vitrification, and high-level waste vitrification. The facilities generate process streams, which are characterized with relatively high concentrations of solids and a non-newtonian rheology (generally described with a Bingham plastic model). The current flow sheet of the WTP includes the use of pulse jet mixers (PJMs) throughout the plant to provide adequate mixing of the process fluids. PJMs consist of large cylindrical tubes with one end tapered down to a jet nozzle. The other end of the pulse tube is connected to an air/vacuum line. In slurry mixing applications, several PJMs are immersed into the mixing vessel and operated either in series or in parallel to achieve the desired mixing without moving mechanical parts. In addition to the mixing provided by the PJMs, for the most concentrated slurries, hybrid mixing systems using air spargers and/or steady jets provide the mixing strategy.

During normal operation, the mixing systems (PJM's, air spargers, recirculation) in the WTP vessels (including non-newtonian waste slurries) must achieve safe, controllable release of flammable gases including hydrogen). Previous experimental studies using PJM mixing systems identified a formation of active mixing caverns at the bottom of the mixing vessels and a lack of mixing at the upper portion of the vessel, which may result in accumulation of gas produced by radiolysis in the stagnant fluid or gel. During loss-of-power events, PJMs may be operated intermittently on backup power for extended periods, which can result in gelling of the slurry and accumulation of hydrogen or other flammable gases in the gelled slurry. Upon restart of the PJMs, the mass of released hydrogen gas and rate of release must not create flammable conditions in the vessel headspace. Furthermore, the process flow sheet will consider the addition of an anti-foam agent (AFA) to the process streams to prevent surface foaming, which may modify the gas retention and release patterns of the waste fluids.

conducted by PNNL [1, 2] and SRS [3] . Previous studies conducted by PNNL [1, 2] and SRS [3] provide detailed investigation of the steady state gas hold up and the subsequent gas release behavior in normal operations for simulants with yield stress greater than 10 Pa, however, additional experimentation is needed to provide a better understanding of the gas dynamics in the loss of power events or transient conditions especially in a low yield stress range of 0-10 Pa. The experimental program initiated at Florida International University extends experimental studies previously conducted at SRS and PNNL by addressing the transient behavior of gas release, retention and release patterns for mixtures with yield stress parameter ranging from 2-13 Pa

EXPERIMENTAL

Objective

The primary objective of the tests conducted at FIU was to:

a) Evaluate and test the gas retention and release characteristics of low yield stress waste simulants (0-10 Pa) with and without AFA after simulant gelling.
b) Determine how the variations in yield stress alter the gas retention and release behavior.
c) Correlate the retained gas fraction as a function of key variables such as:
    i. Simulant type (Kaolin-Bentonite, AZ-101)
    ii. Simulant properties (viscosity, yield stress)
d) Determine, measure, and correlate key physico chemical variables of the fluid and identify effects of AFA.

Experimental Set-up

The experimental setup shown in Figure 38 consisted of the following major components: (1) test vessel with inner diameter of six inches and height of seventy-two inches made of clear plastic, (2) a millimeter wave level detection probe/system that measured 0.5% level change, (3) inlet and outlet ports at the top to purge the headspace with argon, injection ports for hydrogen peroxide and iron mixture and inlet ports of nitrogen air sparging system, (4) two mass flow meters/controllers to measure the mass of gas entering and leaving the system, (5) mechanical mixer with three impellers and a sparging system consisting of four spargers and (6) mass spectrometer to measure the concentration of the gases in the effluent stream.

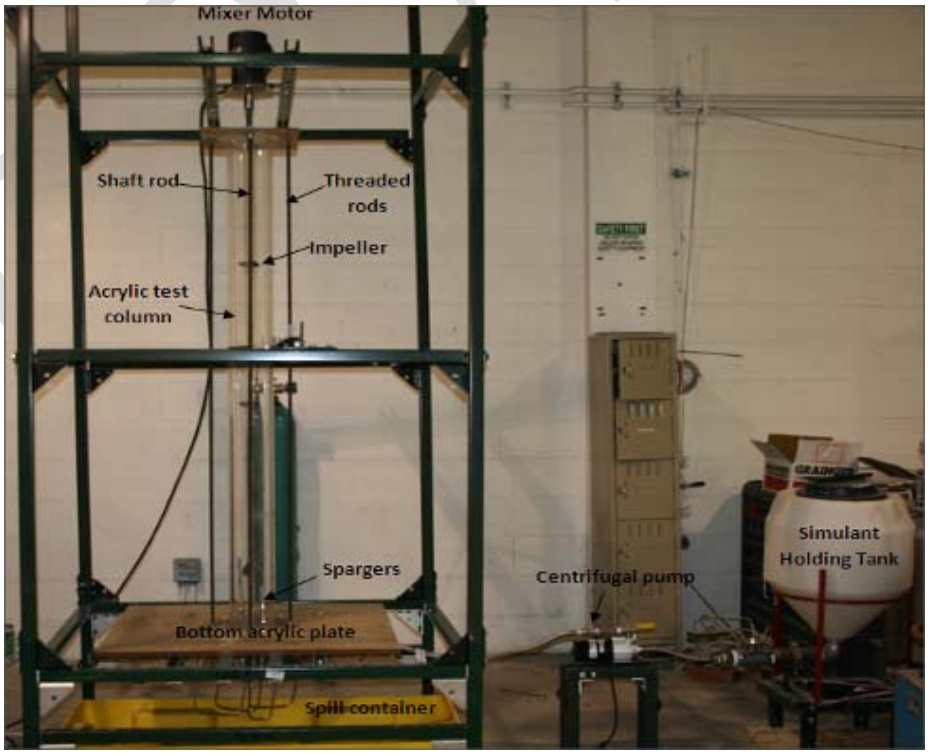

Figure 38. Experimental set-up.

Column Set-Up

The column set-up consisted of an acrylic test column (6 inch OD x 72 inch height) capped on both ends with two 12 inch x 12 inch acrylic plates that are held together with four ½" threaded rods. In order to create a stable test column, the base was supported by a 48 inch x 48 inch x 24 inch frame made of unistrut channels as shown in Figure 39 below.

Figure 39. Test column set-up.

Mixer System Set-Up

The mixing system consisted of three impellers on a common shaft. A "rake" or sweep-impeller was added below the lower impeller to improve mixing in the volume below the lower impeller. This sweep impeller, design shown below, had an overall diameter of 4 inches. The impellers were located on a single 1/2-inch shaft supported at the top by the packed seal and at the bottom by a teflon bushing located at the top of the radial flow deflector. The shaft was driven through a flexible coupling to allow for ease of alignment of the motor drive and the shaft. The pitch orientation for both impellers was selected for upflow displacement of fluid during mixing, and the impellers were placed on the shaft to avoid gas entrapment in the vortex under well-mixed conditions. The vessel contents were considered well mixed when movement of fluid at the walls of the vessel could be observed. In other words, the entire fluid volume was fully sheared. In this regards, visual observations of fluid movement at the walls and the shape of the surface vortex was used to guide setting the mixer speed. The mixer shaft speed was monitored continuously with a laser tachometer and controlled manually. In addition to impellers, a set of spargers were

used to aid in mixing. The spargers were fitted via a cross connector and nitrogen gas was injected from the bottom through a stainless steel tube to ensure mixing across the entire test vessel. The injected bubbles were directed at the tip of the lower impeller to break up the larger bubbles into smaller bubbles. The sparger flow rate was controlled by a mass flowmeter. Figure 40 below shows the FIU designed rake impeller and the spargers installed in the test column.

Figure 40. Rake impeller (left) and spargers (right).

Integrating System Components

The inlet and outlet connections to mass flowmeters, ball valves and test column were made with compression fittings. Copper tubing (1/4" OD) was used to transport the argon purge gas as well as the gas to the gas analyzer. A peristaltic pump was used to pump hydrogen peroxide into the tank via Teflon tubing. Stainless steel tubing was used to transport the nitrogen sparging gas at the bottom of the third impeller. A centrifugal pump transferred the simulant (around 8 gallons) into the tank and a three way valve was installed to function as a transport valve when pumping the simulant and a drain valve when draining the simulant out of the column.

Test Procedure

The in-situ generation and release tests used oxygen generated through decomposition of H_2O_2 as the surrogate gas for hydrogen. The level of oxygen hold-up in the gelled simulant was controlled by the amount of H_2O_2 added to the simulant before gelling. The in-situ gas retention and release tests consisted of the addition of hydrogen peroxide (H_2O_2) to the simulant and mixing it over a period of about 2 minutes to assimilate the peroxide into the simulant. The mixing was then ceased and the oxygen generated in-situ from peroxide decomposition was allowed to accumulate in the simulant. The simulant was allowed to gel for 18 hours. At the end of the 18-hour gel period, the simulant was mixed to measure the gas release rate. The physical characteristic of the in-situ generated gas through peroxide decomposition was presumed to resemble that of hydrogen accumulated from radiolysis in the gelled waste. The test procedures are described in detail in [5].

Figure 41 illustrates the gas flow during purging and simulant conditioning. Simulant conditioning was essential before gas injection into the simulant. The following operating procedure was applied for conditioning the simulant: the mixer speed was increased very

gradually without cavitation or cavern formation until the predetermined mixing speed was reached.

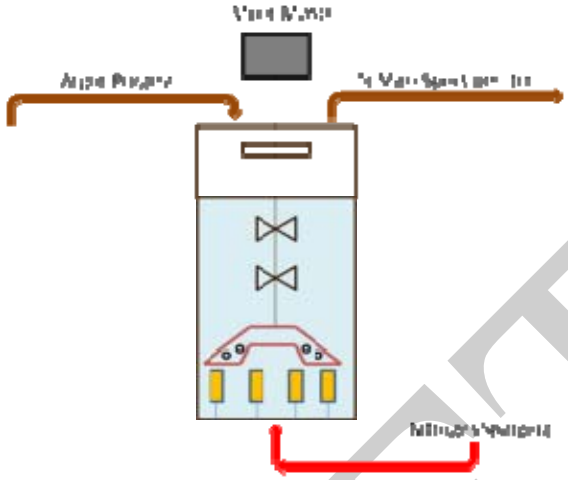

Figure 41. Gas flow during purging and simulant conditioning.

Figure 42 illustrates the gas flow during hydrogen peroxide injection. The gas hold-up in the simulant was determined by the change in the volume of the simulant in the vessel. A predetermined amount of hydrogen peroxide was injected into the vessel after completing simulant conditioning. The purging gas and oxygen concentration were monitored and recorded via mass spectrometer.

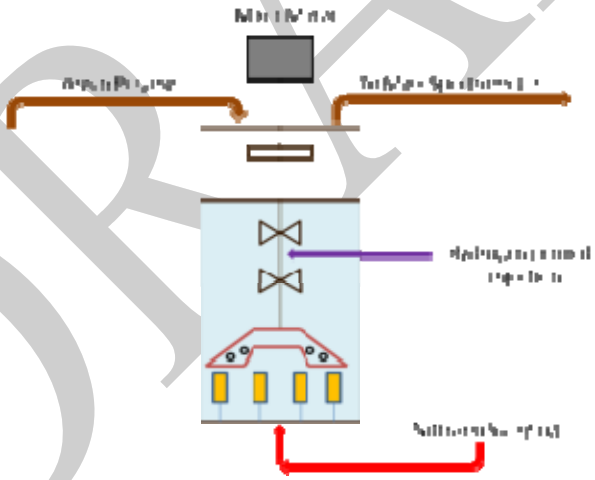

Figure 42. Gas flow during hydrogen peroxide injection.

Figure 43 illustrates gas flow for the gas release from a gelled simulant. The headspace was continuously purged with argon gas overnight and the simulant was allowed to gel at least 18 hrs. The release of oxygen from the simulant was measured in two steps:

1. At the end of the gel period, the purge gas rate was set at 1500 ml/min. The oxygen accumulated overnight in the overhead space in the vessel was measured and recorded until the oxygen concentration has reached the background level.
2. The mixer was started and the mixer speed was gradually increased to the predetermined value. The concentration of the oxygen gas in the effluent was monitored (including the

purge gas and effluent gas flow rates). The end of the experiment was assumed when the asymptotic value of oxygen over a 2-hour period had approached the detection limits.

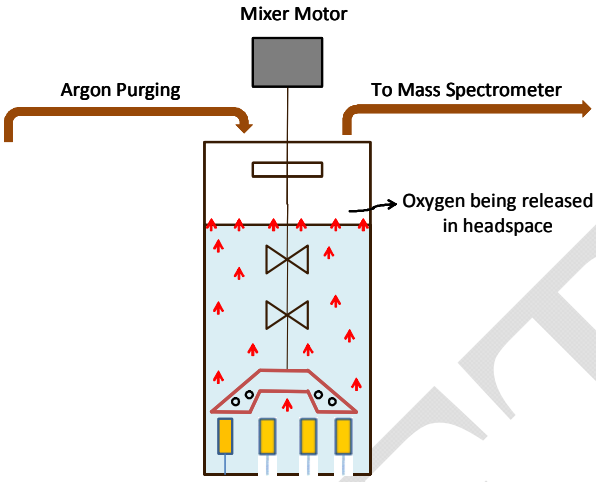

Figure 43. Gas flow during release of oxygen from gelled state.

Gas Hold-Up from In-Situ Generation

Peroxide dosage was determined by calculating the oxygen gas released from the catalytic decomposition of hydrogen peroxide according to the following reaction:

$$2H_2O_2 \leftrightarrow 2H_2O + O_2 \quad (55)$$

The released oxygen diffuses through the simulant and supersaturates the fluid. Further decomposition of H_2O_2 leads to bubble nucleation and bubble growth as O_2 continues being released in the simulant.

Gas Release from Gelled Simulant

The gel release tests with in-situ generated gas bubbles had 2 separate periods for oxygen monitoring: (i) release during the overnight 18-hour gelling period, and (ii) gel release upon mixing the gelled simulant. It was essential to know the volume of oxygen released during the initial and overnight gelling periods to estimate the volume of oxygen retained in the gel prior to initiating the mixing gel release. The mixer was initially operated at a low speed in the range of 50 to 75 RPM for the first 1 to 2 minutes before increasing the speed to the value selected for the test. This procedure was adopted to avoid damage to the mixer motor from torque overload, and to facilitate a less-than violent release of the large volume of gas released at the start of mixing. It was believed that this may approximate (but certainly not represent) the start of mixing in a vessel equipped with PJMs during the first cycle pulse when mixing is incomplete. The oxygen and nitrogen concentrations in the effluent gas were recorded until the minimum measurement concentration for oxygen was reached.

Simulant Selection

The simulants for the gas retention and release tests were selected following the guidelines provided by Poloski et al. [4]. Properties such as yield stress, consistency, shear strength, safety, thixotropy, ease of preparation, expense, transparency and stability were considered. For evaluating the simulants on the basis of the above mentioned properties, Poloski et al. [4] used a

scoring system in which the simulants were evaluated on a scale of 1–3, where 1 is poor, 2 is fair, and 3 is good. Weighting factors were applied to the criteria such that significant weight was placed on factors that directly affected test success. The scores from each category were multiplied by the weighting factors and summed. These values were normalized to the high score value of 3.

The test program required the simulant to be safe to use as loading, unloading and sampling of the simulant could expose the personnel to the simulant and working in protective equipment for several hours would add undesirable complications. Yield stress was the primary control variable for the proposed tests; hence a simulant whose non-newtonian rheological properties varied by dilution with water was required. Because testing was going to take over several months, the simulant needed to exhibit constant rheological properties and be stable. Due to a large numbers of tests proposed to be conducted, an inexpensive simulant was also desired to minimize the impact on project costs. Table 1 shows the rheological parameters for the experimental program

Table 1. Significant Simulant Properties for Hybrid Mixing Systems and Goal Values

Property	Goal Values
Density	1.2g/ml
Bingham Yield Stress	0-10 Pa
Bingham consistency	10 cP

The test program required four different simulants whose non-newtonian rheological properties varied by dilution with water. Hence kaolin-bentonite, laponite, xanthan gum and AZ-101 were selected as they tend to meet the rheology criteria of the experimental program and tests were planned using these four simulants. However after talks with the site personnel it was determined that laponite and xanthan gum did not meet the site's minimum requirements of wt% solids (>20 wt %) that were needed to reach the target yield stress and hence they were removed from consideration. The simulants used in the test program are shown in Table 2 below.

Table 2. Simulants Used in the Test Program

Simulant	Yield Stress Pa	Solids Concentration %
Kaolin-Bentonite Mix	2-13	22-28
AZ-101 (provided by site)	4-13	NA

Two drums of AZ-101 were provided by the site: (1) A 40 gallon drum with AFA. The drum with AZ-101 mixed with AFA had very low concentrations of solids and yield stress considerably lower than 1, therefore, this batch was not used for testing and (2) a 55 gallon drum without AFA. This drum contained noble metals such as palladium nitrate, rhodium nitrate, ruthenium chloride and silver nitrate mixed in AZ-101. Testing with AZ-101 from this drum resulted in an instantaneous (within the first few minutes) decomposition of 30 wt% hydrogen peroxide. In order to slow down the reaction rate, the hydrogen peroxide was diluted to 0.5 wt% and kaolin-bentonite was added to AZ-101 in the ratio of 2: 1.

Test Matrix - Kaolin-Bentonite

For the estimation of the gas release parameter in clay simulants, clay simulants with varying rheology were tested for gel release behavior with and without AFA: (i) 14 wt % clay simulant (2 Pa yield stress), (ii) 17 wt % clay simulant (4 Pa yield stress), (iii) 18.5 wt % clay simulant (7 Pa yield stress), (iv) 21 wt % clay simulant (10 Pa yield stress) and (v) 22 wt% (13 Pa yield

stress). The 2 Pa tests were repeated thrice to validate the repeatability of their gas retention and release properties for the selected yield stress. A Haake RS150 rheometer was used to measure the rheology before and after test. The initial conditions, including the targeted gas hold-up based on stoichiometric calculations assuming completion of hydrogen peroxide decomposition, are given in (Table 3).

Table 3. Summary of In-situ Gas Retention and Release Test Conditions Using Peroxide without AFA

Test	Simulant	Yield Stress Pa	$V_{simulant}$ L	V_{oxygen} L	Holdup L	Holdup %	T °C	Mixer speed RPM
C01	Clay	2	21.98	2.09	2.01	8.42	24-25	335-350
C02	Clay	2	21.98	2.10	2.02	8.43	24-25	335-350
C03	Clay	2	21.98	2.09	2.02	8.43	24-25	335-350
C04	Clay	4	21.98	2.28	1.50	6.45	24-25	335-350
C05	Clay	7	22.02	2.41	0.85	3.74	22-23	335-350
C06	Clay	10	22.02	1.81*	0.77	3.41	23-24	335-350
C07	Clay	13	22.05	1.84*	0.58	2.57	24-25	335-350

*A minute quantity of hydrogen peroxide got leaked while injecting via the injection port due to the back pressure of the simulant and hence less volume of oxygen was generated.

For the tests with AFA, Q2-3183A AFA was diluted with 3 to 10 parts water and mixed with the prepared simulant prior to the commencement of testing.

Table 4. Summary of In-situ Gas Retention and Release Test Conditions Using Peroxide with AFA

Test	Simulant	Yield Stress, Pa	AFA ppm	$V_{simulant}$ L	V_{oxygen} L	Holdup L	Holdup %	T °C	Mixer speed RPM
D01	Clay	2	350	21.98	2.09	2.01	8.42	24-25	335-350
D02	Clay	4	350	21.98	2.28	1.50	6.45	24-25	335-350
D03	Clay	7	350	22.02	2.41	0.85	3.74	22-23	335-350
D04	Clay	10	350	22.02	1.81*	0.77	3.41	23-24	335-350
D05	Clay	13	350	22.05	1.84*	0.58	2.57	24-25	335-350

*A minute quantity of hydrogen peroxide got leaked while injecting via the injection port due to the back pressure of the simulant and hence less volume of oxygen was generated.

Test Matrix - AZ-101

For the testing with AZ-101+clay mix, tests were planned with five different rheologies: 2, 4, 7, 10 and 13 Pa. But the dilution of hydrogen peroxide from 30% to 0.5% required a large quantity of water which when added to the column contents, diluted the slurry and changed the rheology. Moreover, the rheology could only be determined after a particular test had finished. Hence it was only possible to do testing with three different rheologies. Table 5 and Table 6 show the test matrix for tests with AZ-101+clay mix with and without AFA.

Table 5. Summary of In-situ Gas Retention and Release Test Conditions Using Peroxide without AFA

Test	Simulant	Yield Stress Pa	$V_{simulant}$ L	V_{oxygen} L	Target Holdup %	Act. Holdup %	T °C	Mixer speed RPM
A01	AZ-101 +clay	4	22.02	2.48	10	4.50*	23-25	350-375
A02	AZ-101 +clay	7	21.98	2.34	10	4.00*	23-25	350-375
A03	AZ-101 +clay	13	21.98	2.18	10	3.59*	23-25	350-375

***** The actual hold-up is less than the target hold-up as oxygen gas was released during hydrogen peroxide injection due to high iron content of the bad AZ-101 batch

Table 6. Summary of In-situ Gas Retention and Release Test Conditions Using Peroxide with AFA

Test	Simulant	Yield Stress Pa	AFA ppm	$V_{simulant}$, L	V_{oxygen}, L	Target Holdup, %	Act. Holdup %	T °C	Mixer speed RPM
B01	AZ-101 +clay	4	350	22.02	2.85	10	5.22	23-25	350-375
B02	AZ-101 +clay	7	350	21.39	2.90	10	6.17	23-25	350-375
B03	AZ-101 +clay	13	350	21.98	2.65	10	4.32	23-25	350-375

Rheology Measurements

As yield stress was the primary controlling variable for the gas retention and release tests, it was easier to dilute the simulant with water to achieve the target yield stress than evaporation. The rheology measurements were made before and after testing with the Haake RS 150 rheometer. Flow curve measurements were obtained using the Z41 cylindrical rotor. A sample volume of approximately 15 ml was added to the sample cup and then the rotor and sample cup were installed onto the rheometer. Next, the rheometer drove the rotor into the predetermined bottom off-set position of 3-mm. A cooling bath was used to control the sample temperature at 25°C. Yield stress measurements were made by linearly increasing the shear rate from 0 to 1000 s^{-1} over 300 s. Each measurement was made in triplicates and fit to Bingham Plastic model. Table 7 and Table 8 show the yield stress and viscosity measurements taken before and after each tests for kaolin-bentonite tests with and without AFA.

Table 7. Yield Stress and Viscosity Measurements for Kaolin-Bentonite Simulant without AFA

Target Yield Stress, Pa			**Run 1**	**Run 2**	**Run 3**
2	Before Test	Yield Stress (Pa)	2.21	2.62	2.29
		Viscosity (Pas)	0.03	0.04	0.04
2	After Test	Yield Stress (Pa)	2.52	2.14	2.11
		Viscosity (Pas)	0.04	0.04	0.04
4	Before Test	Yield Stress (Pa)	4.22	4.03	4.10
		Viscosity (Pas)	0.07	0.07	0.07

4	After Test	Yield Stress (Pa)	3.37	3.53	3.62
		Viscosity (Pas)	0.06	0.06	0.06
7	Before Test	Yield Stress (Pa)	7.17	7.90	7.75
		Viscosity (Pas)	0.06	0.07	0.07
7	After Test	Yield Stress (Pa)	6.99	6.56	6.41
		Viscosity (Pas)	0.06	0.06	0.04
10	Before Test	Yield Stress (Pa)	10.15	10.59	10.31
		Viscosity (Pas)	0.06	0.07	0.07
10	After Test	Yield Stress (Pa)	10.23	10.01	9.95
		Viscosity (Pas)	0.06	0.07	0.06
13	Before Test	Yield Stress (Pa)	14.20	14.30	14.02
		Viscosity (Pas)	0.11	0.11	0.12
13	After Test	Yield Stress (Pa)	13.44	13.90	13.43
		Viscosity (Pas)	0.13	0.14	0.14

Table 8. Yield Stress and Viscosity Measurements for Kaolin-Bentonite Simulant with AFA

Target Yield Stress, Pa			**Run 1**	**Run 2**	**Run 3**
2	Before Test	Yield Stress (Pa)	2.28	2.09	1.95
		Viscosity (Pas)	0.04	0.04	0.04
2	After Test	Yield Stress (Pa)	2.23	2.01	2.01
		Viscosity (Pas)	0.03	0.03	0.03
4	Before Test	Yield Stress (Pa)	3.96	4.21	4.01
		Viscosity (Pas)	0.06	0.05	0.06
4	After Test	Yield Stress (Pa)	3.52	3.92	3.63
		Viscosity (Pas)	0.06	0.06	0.06
7	Before Test	Yield Stress (Pa)	7.46	7.27	7.26
		Viscosity (Pas)	0.06	0.07	0.07
7	After Test	Yield Stress (Pa)	5.66	5.80	5.56
		Viscosity (Pas)	0.05	0.05	0.05

10	Before Test	Yield Stress (Pa)	9.96	9.89	10.07
		Viscosity (Pas)	0.07	0.07	0.08
10	After Test	Yield Stress (Pa)	9.10	9.21	9.34
		Viscosity (Pas)	0.08	0.08	0.08
13	Before Test	Yield Stress (Pa)	12.33	12.87	12.97
		Viscosity (Pas)	0.15	0.15	0.14
13	After Test	Yield Stress (Pa)	11.56	11.39	11.8
		Viscosity (Pas)	0.12	0.11	0.12

Table 9 and Table 10 provide the before and after test yield stress and viscosity measurements for the tests done using AZ-101+clay mix with and without AFA. As a large amount of water was added to dilute the hydrogen peroxide from 30 % to 0.5%, the rheology was only measured once the test had finished and was considered to represent the targeted rheology.

Table 9. Yield Stress and Viscosity Measurements for AZ-101+Clay Mix without AFA

Target Yield Stress, Pa			**Run 1**	**Run 2**	**Run 3**
4	Before Test	Yield Stress (Pa)	7.11	7.17	6.88
		Viscosity (Pas)	0.05	0.05	0.05
4	After Test	Yield Stress (Pa)	4.52	4.72	4.75
		Viscosity (Pas)	0.04	0.04	0.04
7	Before Test	Yield Stress (Pa)	10.01	10.36	10.67
		Viscosity (Pas)	0.06	0.05	0.05
7	After Test	Yield Stress (Pa)	7.11	7.17	6.88
		Viscosity (Pas)	0.05	0.05	0.05
13	Before Test	Yield Stress (Pa)	15.87	16.01	16.42
		Viscosity (Pas)	0.09	0.09	0.08
13	After Test	Yield Stress (Pa)	12.78	12.81	12.59
		Viscosity (Pas)	0.06	0.05	0.05

Table 10. Yield Stress and Viscosity Measurements for AZ-101+Clay mix with AFA

Target Yield Stress, Pa			Run 1	Run 2	Run 3
4	Before Test	Yield Stress (Pa)	7.12	7.21	7.34
		Viscosity (Pas)	0.06	0.07	0.07
4	After Test	Yield Stress (Pa)	4.01	4.89	4.64
		Viscosity (Pas)	0.04	0.05	0.05
7	Before Test	Yield Stress (Pa)	10.12	10.21	10.34
		Viscosity (Pas)	0.07	0.07	0.08
7	After Test	Yield Stress (Pa)	7.01	6.89	6.64
		Viscosity (Pas)	0.05	0.06	0.07
13	Before Test	Yield Stress (Pa)	16.01	15.95	16.12
		Viscosity (Pas)	0.09	0.08	0.08
13	After Test	Yield Stress (Pa)	9.34	9.58	9.72
		Viscosity (Pas)	0.08	0.09	0.08

A power law correlation was developed by fitting the rheometer data points as shown in Figure 44.

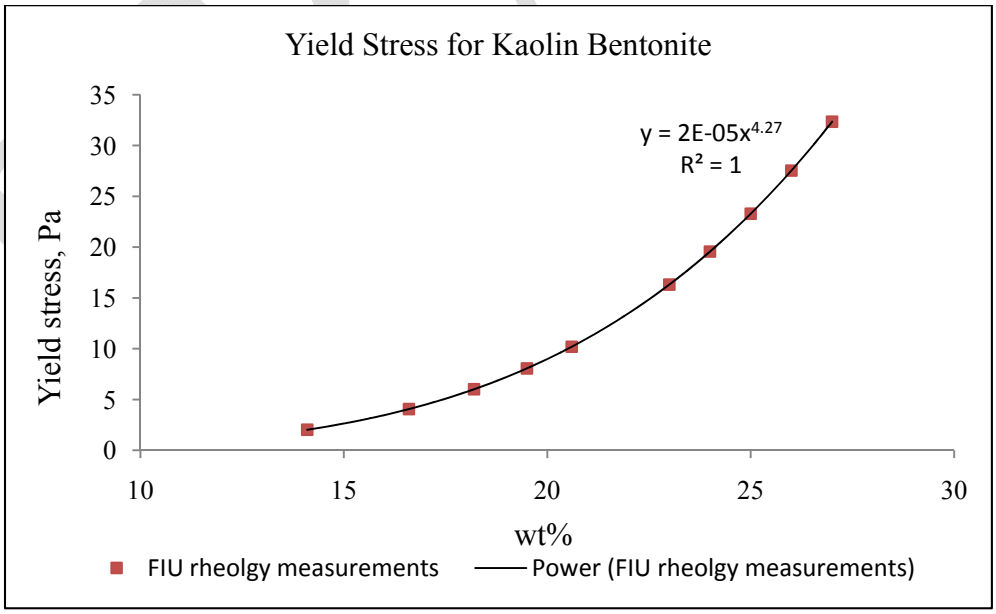

Figure 44. Correlation between Bingham yield stress and kaolin-bentonite concentration at 25 °C.

A National Institute and Technology (NIST) traceable newtonian oil standard was used to verify the operability of the rheometer at a measurement temperature of 25°C every day when flow curve measurements were made.

RESULTS

Kaolin-Bentonite Simulant

Repeatability Tests

Three tests were conducted using the 2 Pa simulant to validate the repeatability of the retention and release characteristics at a given yield stress. The slurry was reused for the subsequent tests. Similar hold-up levels and release rates were observed as seen in Figure 45. The results showed similar gas retention (approx 9 % in all three cases) and similar release constants. A mean relative percent error comparing the three test data was computed to be of +/- 3% concluding that the tests results are repeatable.

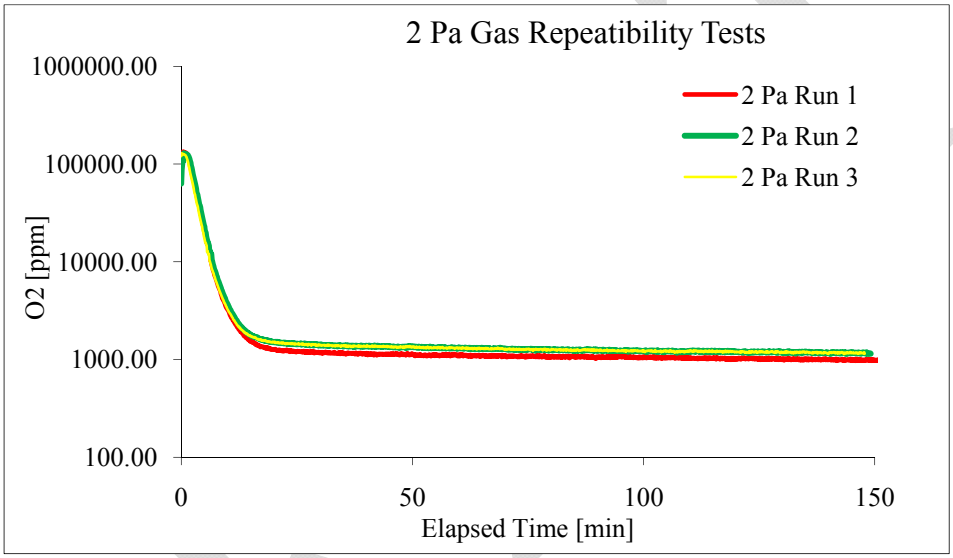

Figure 45. Repeatability tests with 2 Pa slurry.

Without AFA

The level of oxygen hold-up in the gelled simulant was controlled by the amount of hydrogen peroxide added to the simulant before gelling. The gel hold-up levels achieved during these tests and released volumes are summarized in Table 11. These were estimated from the effluent gas oxygen and nitrogen concentrations and the purge gas injection rates.

Table 11. Summary of In-situ Gas Retention and Release Test Results for Kaolin-Bentonite without AFA

Test	Simulant	Yield Stress Pa	Holdup L	Initial Holdup %	Final Holdup after release %	O2 released %
C01	Clay	2	2.01	8.4	<1	97.8
C02	Clay	4	1.50	6.5	<1	98.5
C03	Clay	7	0.85	3.7	<1	98.2
C04	Clay	10	0.77	3.4	<1	96.6
C05	Clay	13	0.58	2.6	<1	98.1

The mixer was operated at 350 rpm which was based on tests with a fluorescent die. An analysis of the release signature curve, as seen in Figure 46 for a 2 Pa yield stress test, shows that the gas is released at two different rates representing two different regions; a faster release rate with a shorter time constant due to direct mobilization of the slurry wherein the majority of the gas gets released followed by a slower release rate with a longer time constant representing release of dissolved oxygen.

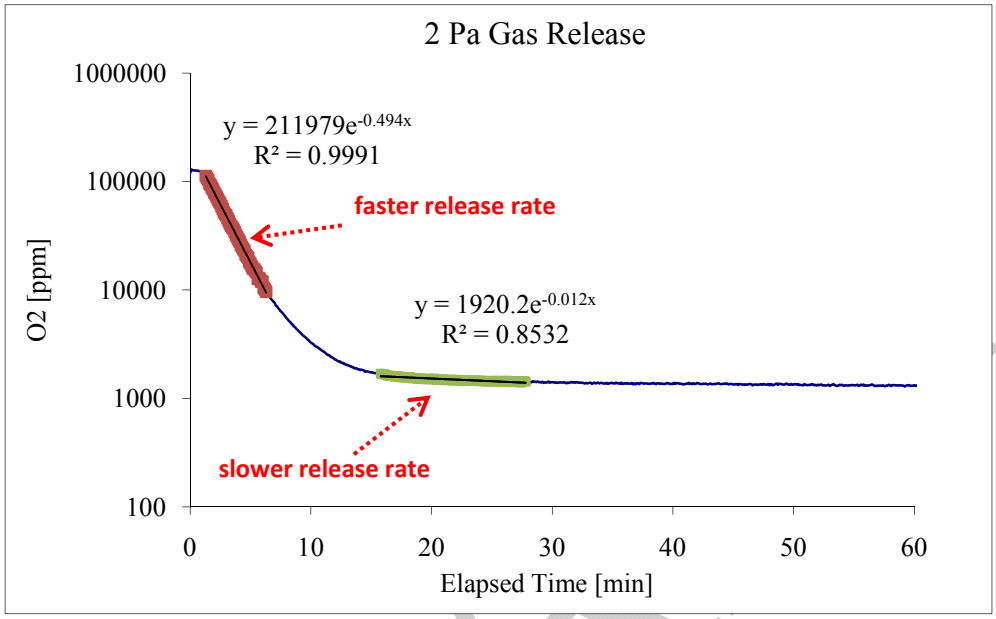

Figure 46. Release curve of the 2 Pa slurry at 350 rpm.

The total oxygen released from the initial hold up while doing the release test after 18 hour retention is shown in Figure 47.

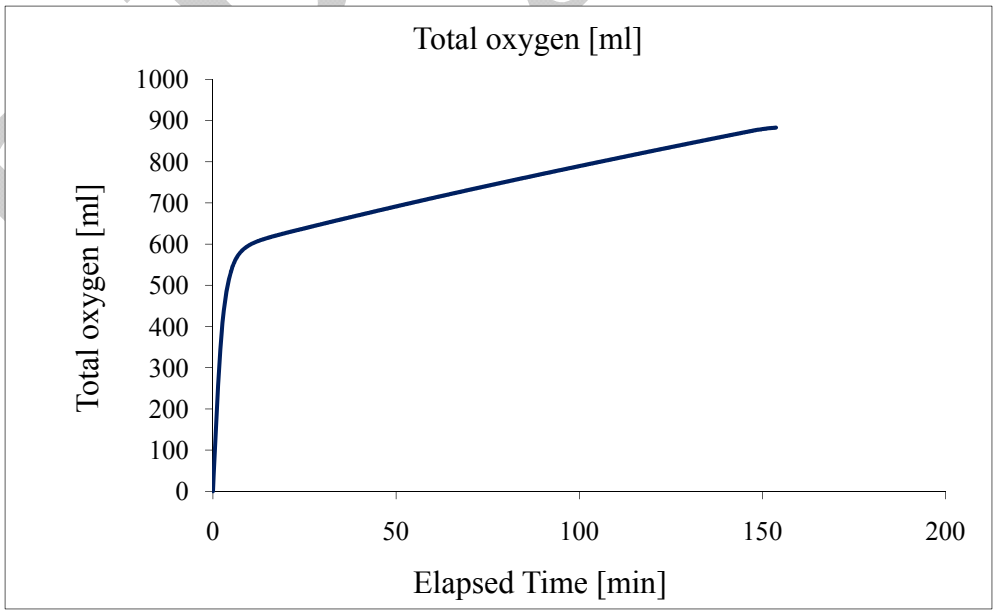

Figure 47. Total oxygen released for the 2 Pa test.

The initial rates of release for the kaolin-bentonite tests for the yield stress range of 2-13 Pa were calculated by fitting the release signature curve by an exponential trend. The release curve followed the first order kinetics. It was assumed that the gas released is the combination of two release rates each with a different peak rate and time constant.

It was noted that as the yield stress increased, the amount of oxygen gas released during gelling also increased. Figure 48 below shows a comparison of the release curves for the 2-13 Pa tests.

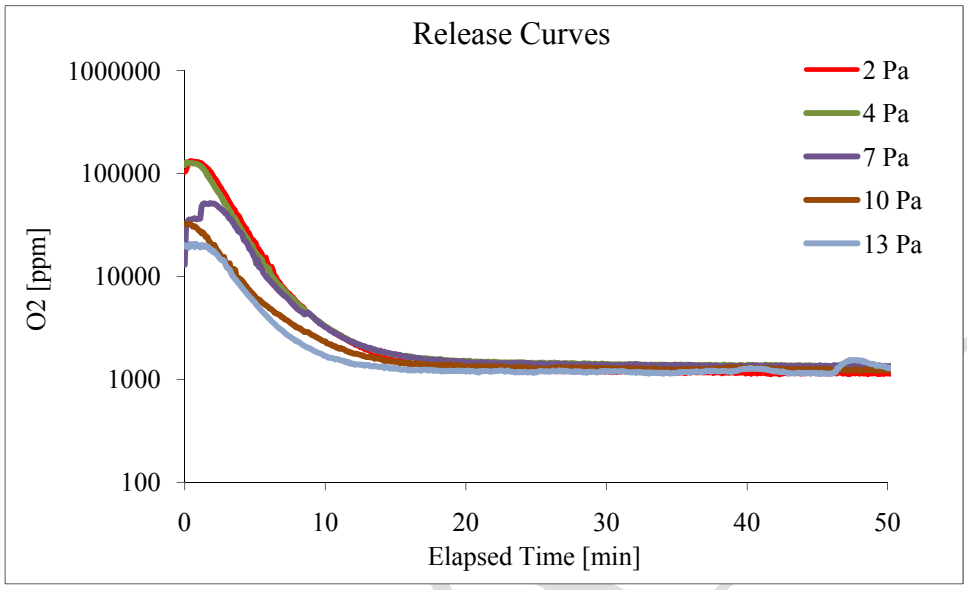

Figure 48. Oxygen concentration during release.

However, when the release curve data was selected to represent the first 15 minutes of the testing as shown in Figure 49, a clear distinction of the gas release could be observed with the varying rheology. It should be noted that as the yield stress increased, the gas hold-up decreased considerably. A majority of the gas got released during the retention period; this trend was more prominent as the yield stress increased.

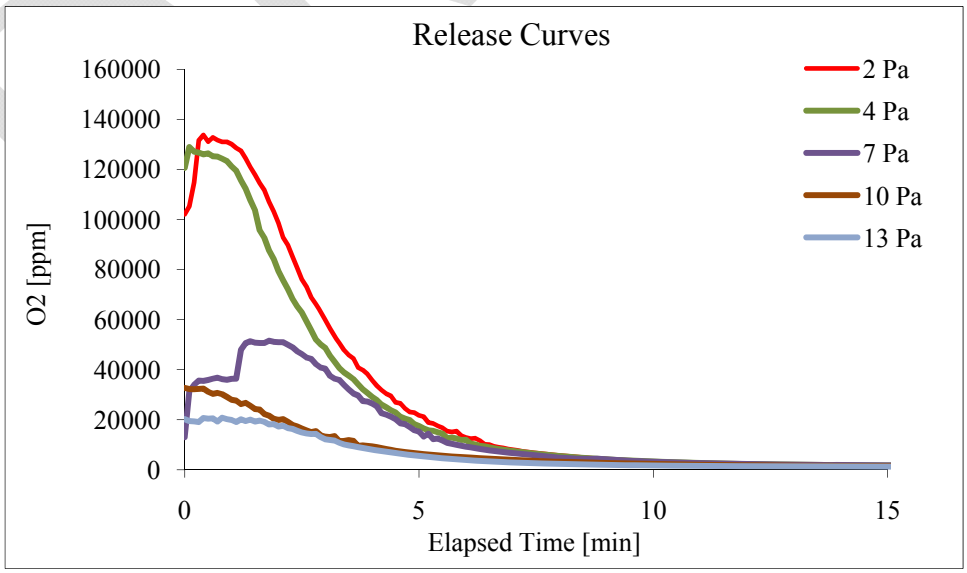

Figure 49. Oxygen concentration during the first 15 minutes.

During the 2 Pa test, 2.09L of oxygen gas was generated stoichiometrically by injecting 20 grams of 30 wt% hydrogen peroxide. Out of that, 1.187 L of oxygen gas was released during the gelling period leaving approximately 0.883 L of gas trapped in the gelled simulant. As the yield stress increased, the amount of oxygen gas released during the gelling period also increased. For example during the 13 Pa test, 1.523 L of oxygen gas was released compared to the 1.187 L released for the 2 Pa test during the gelling period. This left little amount of gas in the gelled state for release as the yield stress increased. The 2 Pa test released 0.883 L of oxygen gas compared to the 0.300 L released by the 13 Pa as seen in Figure 50. In terms of gas hold-up, a 2.50% of hold-up was observed for 13 Pa vs. 8.42% observed for the 2 Pa test.

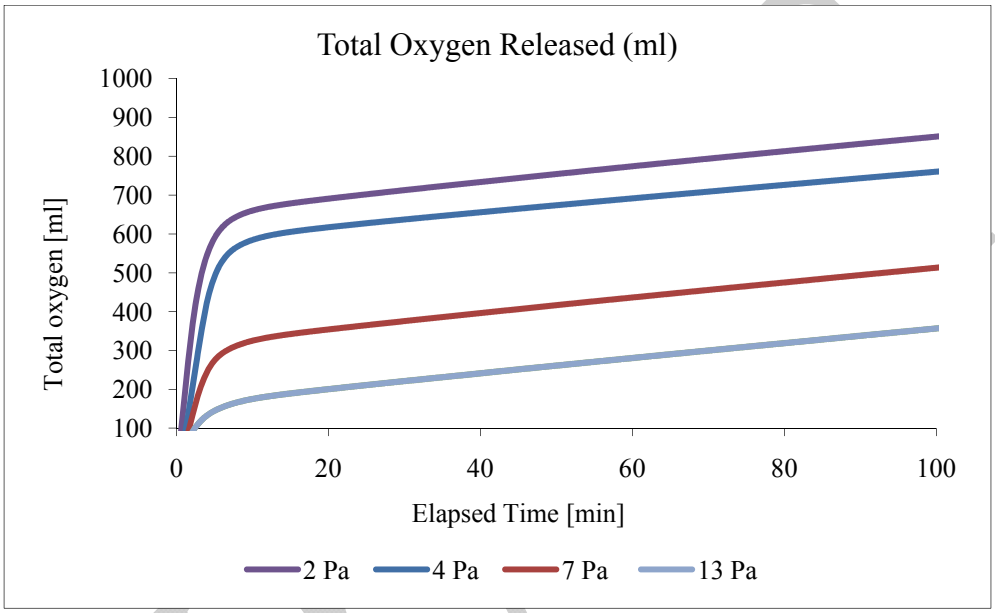

Figure 50. Comparison of the total oxygen gas released.

The estimated gel release rates for the clay simulant from the 1 hold-up levels are shown in Figure 51. It can be inferred that the 2 Pa released gas at a faster rate of 0.50 min^{-1} compared to the slower rate of 0.38 min^{-1} for the 13 Pa clay simulant.

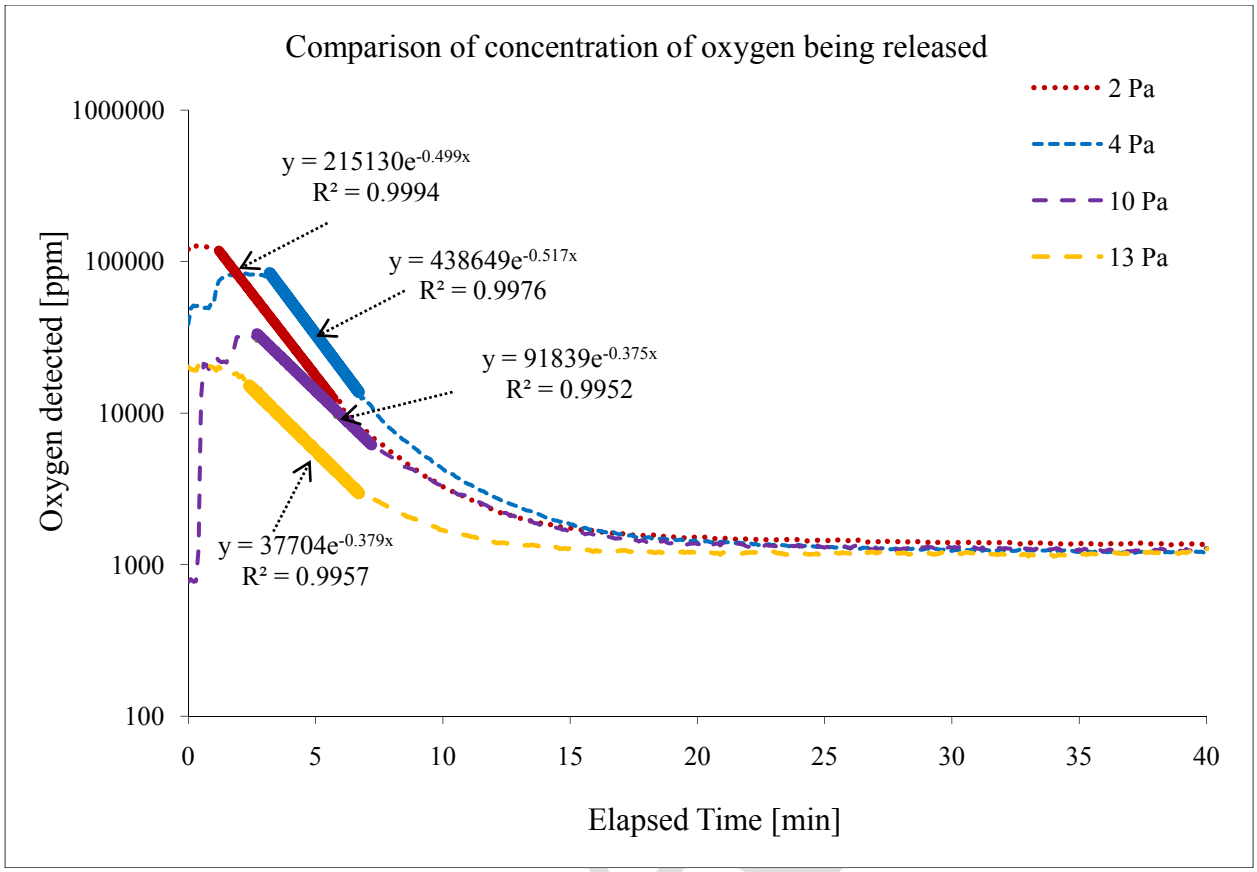

Figure 51. Comparison of oxygen concentration in the effluent stream.

.

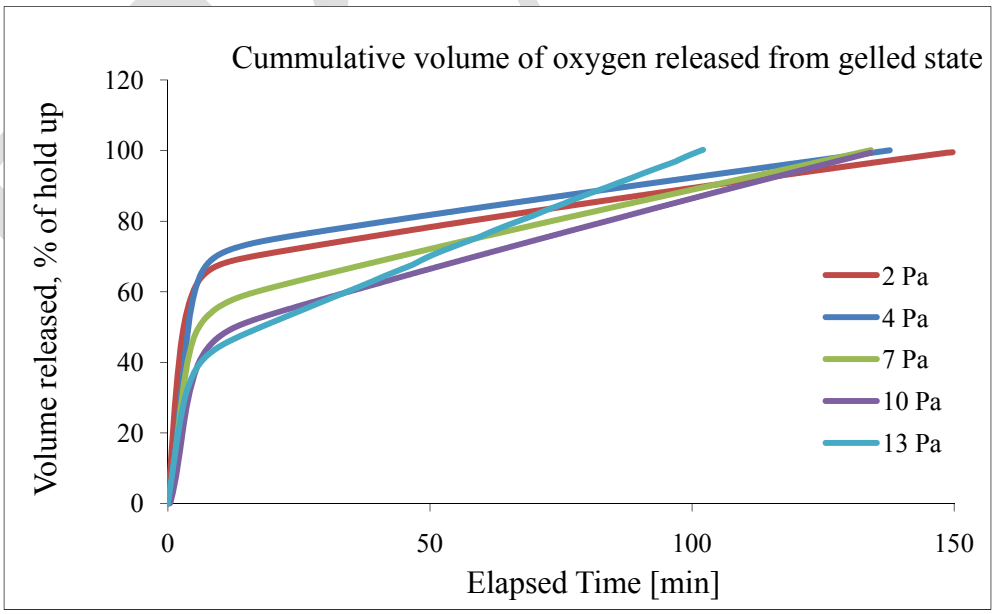

Figure 52. Percentage of oxygen released over the course of the test.

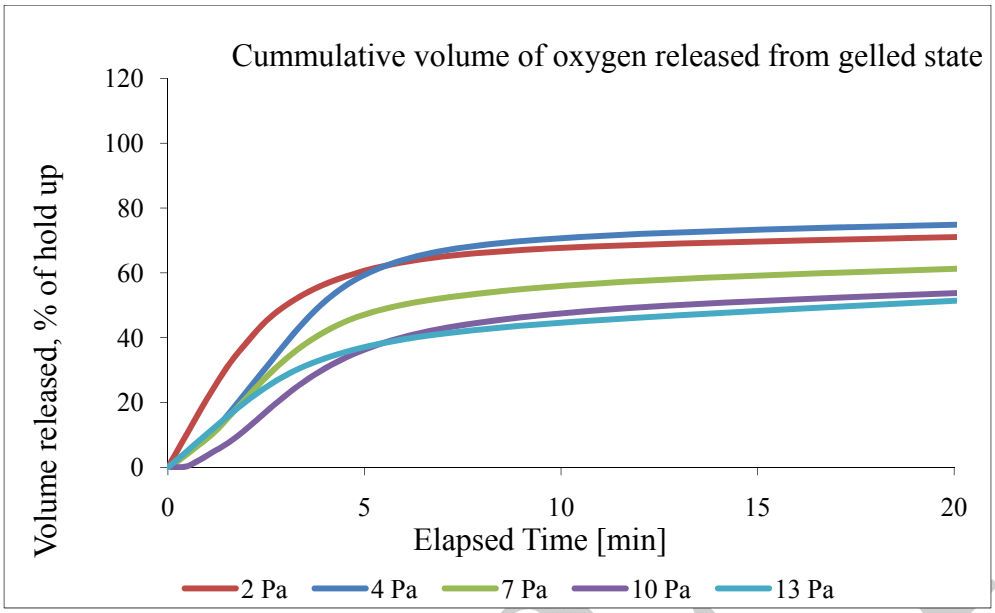

Figure 53. Percentage of oxygen released in the first 20 minutes.

In the initial surge of gas release upon commencement of mixing, a greater fraction of the hold-up was released with lower yield stress simulants. Table 12 summarizes the more important parameters that were determined from the experimental program.

Table 12. Summary of Release Parameters

Test	Simulant	Yield Stress Pa	k_1 min^{-1}	k_2 min^{-1}	Final Holdup %	O_2 released[1] %
C01	Clay	2	0.49	0.01	8.4	75
C02	Clay	2	0.50	0.01	8.4	75
C03	Clay	2	0.49	0.01	8.4	75
C04	Clay	4	0.51	0.02	6.5	73
C05	Clay	7	0.44	0.01	3.7	58
C06	Clay	10	0.37	0.01	3.4	40
C07	Clay	13	0.37	0.01	2.6	35

With AFA

The gel hold-up levels achieved during these tests and released volumes are summarized in Table 13. These were estimated from the effluent gas oxygen and nitrogen concentrations and the purge gas injection rates.

[1] Percentage of oxygen released in the first 15 minutes.

Table 13. Summary of In-situ Gas Retention and Release Test Results for Kaolin-bentonite with and without AFA

Test	Simulant	Yield Stress, Pa	AFA concentration ppm	Holdup L	Final Holdup without AFA %	Final Holdup with AFA %	Final Holdup after release %
D01	Clay	2	350	2.01	8.4	7.2	<1
D02	Clay	4	350	1.50	6.5	7.2	<1
D03	Clay	7	350	0.85	3.7	6.6	<1
D04	Clay	10	350	0.77	3.4	5.8	<1
D05	Clay	13	350	0.58	2.6	5.8	<1

A typical release signature curve is shown in Figure 54 for a 7 Pa yield stress test with AFA and compared with the 7 Pa test without an AFA. The total oxygen released from the initial hold up during the release test after 18 hours of retention is shown in Figure 55.

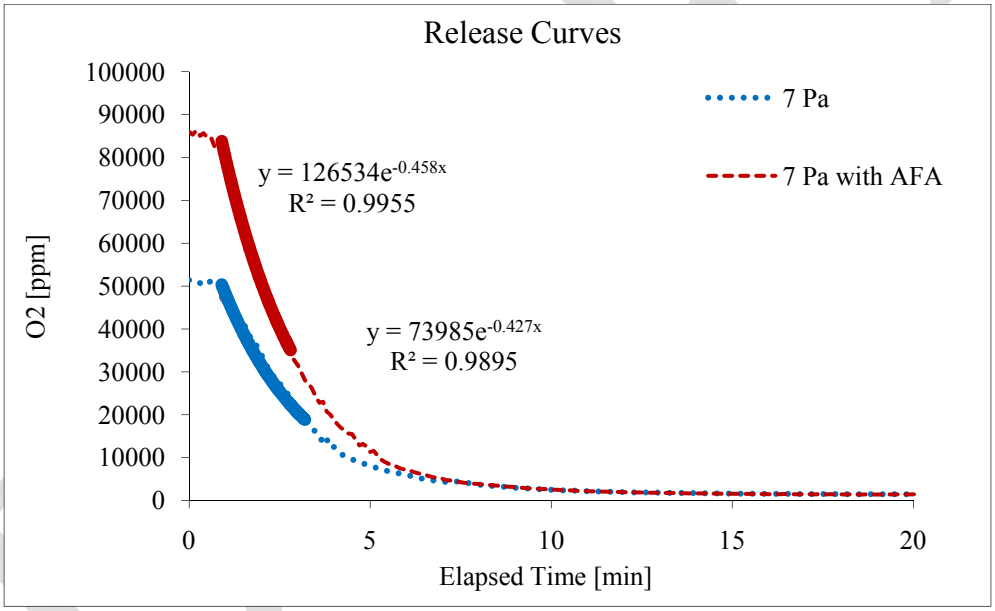

Figure 54. Comparison of release curves with and without AFA for 7 Pa.

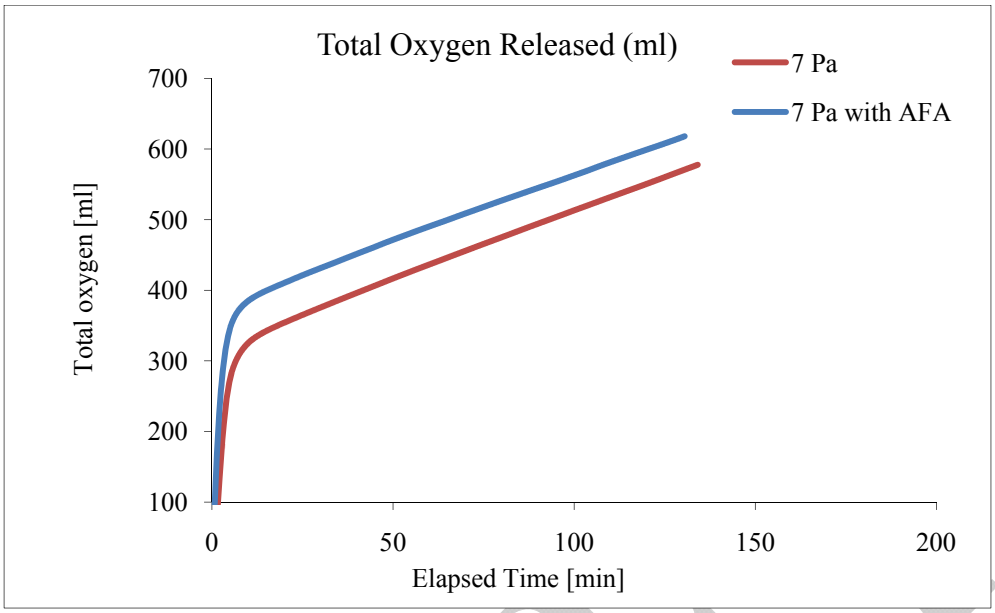

Figure 55. Total oxygen released during the release test for 7 Pa.

The estimated gel release rates for the clay simulant with AFA from the 1 hold-up levels are shown in Figure 56

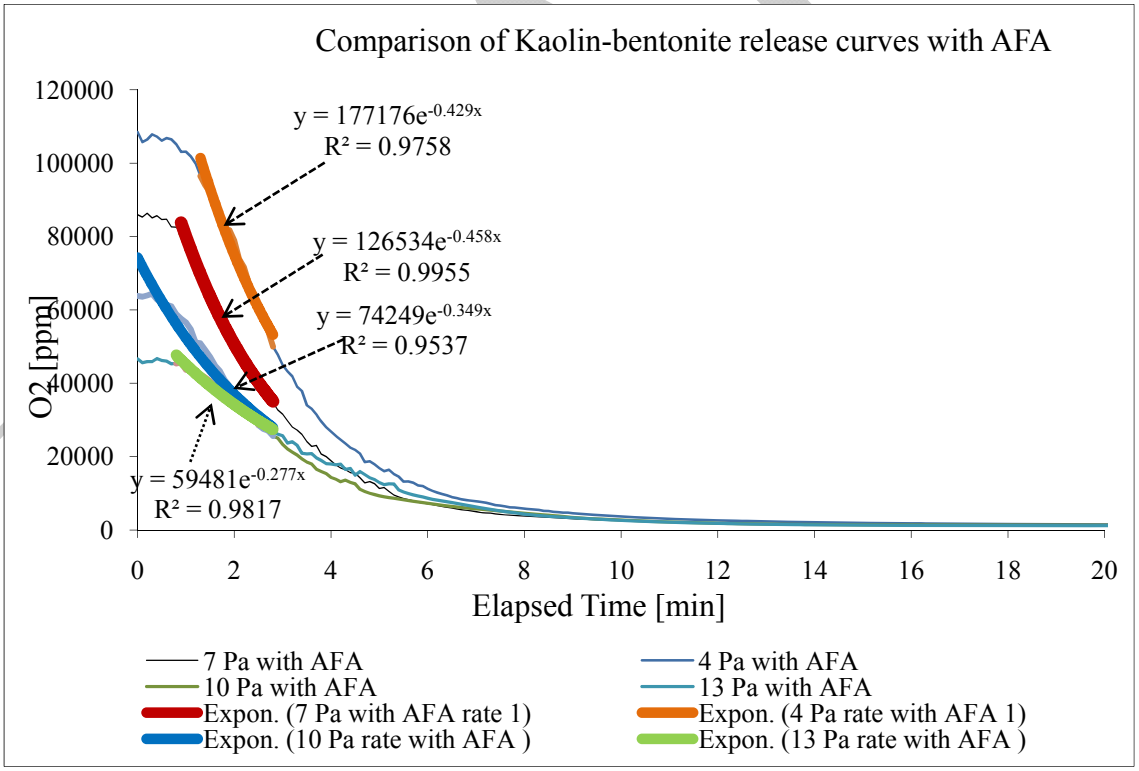

Figure 56. Comparison of release curves for Kaolin-bentonite tests with AFA.

In the initial surge of gas release upon commencement of mixing, a greater fraction of the hold-up was released with lower yield stress simulants. Table 14 summarizes the more important parameters that were determined from the experimental program.

Table 14. Comparison of Release Parameters of Kaolin-Bentonite with and without AFA

Test	Simulant	Yield Stress Pa	k_1(without AFA) min^{-1}	k_1(with AFA) min^{-1}	k_2(without AFA) min^{-1}	k_2(with AFA) min^{-1}
D01	Clay	2	0.49	0.51	0.12	0.12
D02	Clay	4	0.51	0.45	0.13	0.12
D03	Clay	7	0.44	0.46	0.09	0.10
D04	Clay	10	0.37	0.39	0.12	0.18
D05	Clay	13	0.37	0.32	0.11	0.16

AZ-101 Simulant

The AZ-101 simulant was mixed with kaolin-bentonite in the ratio of 1:2 to mitigate the violent decomposition of hydrogen peroxide. In order to determine the ratio to mix, lab scale testing was carried out with 100 ml samples. The lab tests were done for the 1:1 and 1:2 ratio with different concentrations of hydrogen peroxide (0.5%, 1%, 3%, 10% and 30%). It was found from lab tests that the 1:2 ratio of AZ-101 to kaolin-bentonite with the hydrogen peroxide concentration of 0.5% was the most feasible option.

Without AFA

The level of oxygen hold-up in the gelled simulant was controlled by the amount of hydrogen peroxide added to the simulant before gelling. The gel hold-up levels achieved during these tests and released volumes are summarized in Table 15. These were estimated from the effluent gas oxygen and nitrogen concentrations and the purge gas injection rates.

Table 15. Summary of In-situ Gas Retention and Release Test Results for AZ-101-Clay Mix without AFA

Test	Simulant	Yield Stress Pa	Holdup L	Initial Holdup %	O2 released %
A01	AZ-101+Clay	4	2.48	4.5	99.0
A02	AZ-101+Clay	7	2.34	4.0	98.9
A03	AZ-101+Clay	13	2.18	3.6	96.2

Figure 57 shows the oxygen peaks detected in the effluent stream by the mass spectrometer during hydrogen peroxide injection.

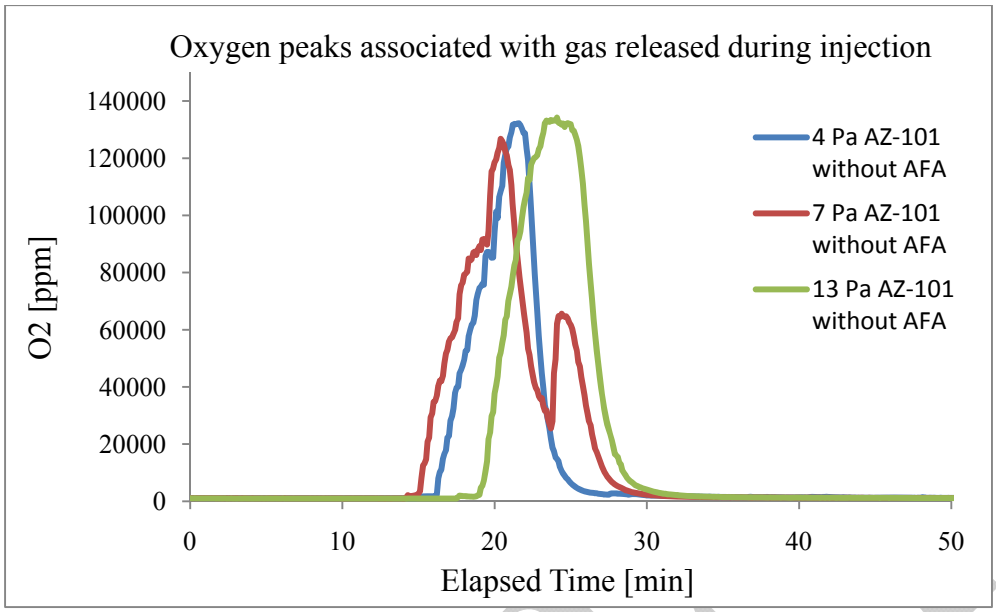

Figure 57. Oxygen peaks detected during hydrogen peroxide injection for AZ-101+Clay mix tests.

The initial rates of release for the AZ-101+clay tests for the yield stress range of 4-13 Pa were calculated by fitting the release signature curve by an exponential trend on a log scale The release curve followed the first order kinetics. It was assumed that the gas released was the combination of two release rates each with a different peak rate and time constant (Figure 58).

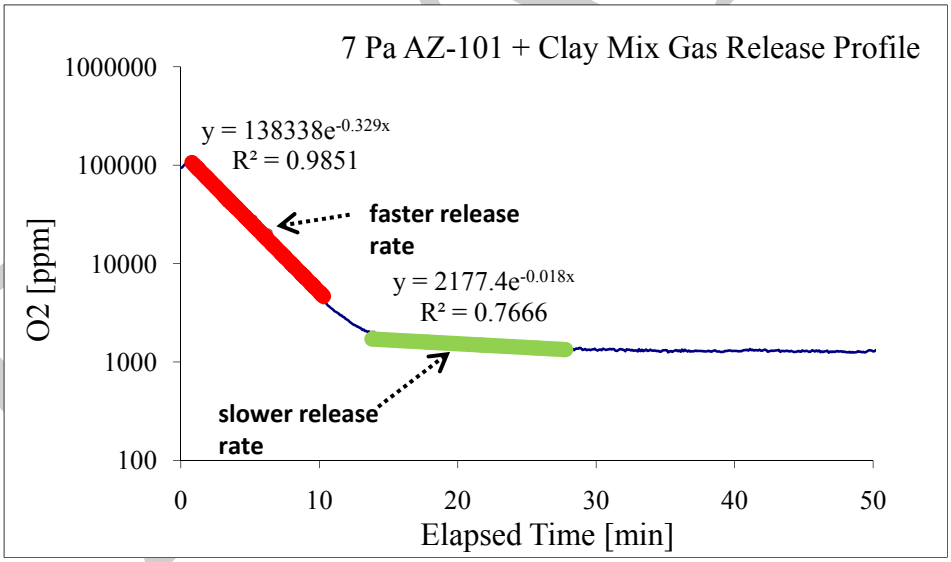

Figure 58. Release curve of 7 Pa AZ-101+Clay mix at 350 rpm.

During the 7 Pa test, approximately 2.41 L of oxygen gas was generated by injecting 1380 grams of 0.5 wt% hydrogen peroxide. Out of that 1.463 L of oxygen gas was released during the gelling period. The initial hold up observed visually was 4.6%. The total oxygen released from the initial hold up while doing the release test after 18 hour retention is shown in Figure 59.

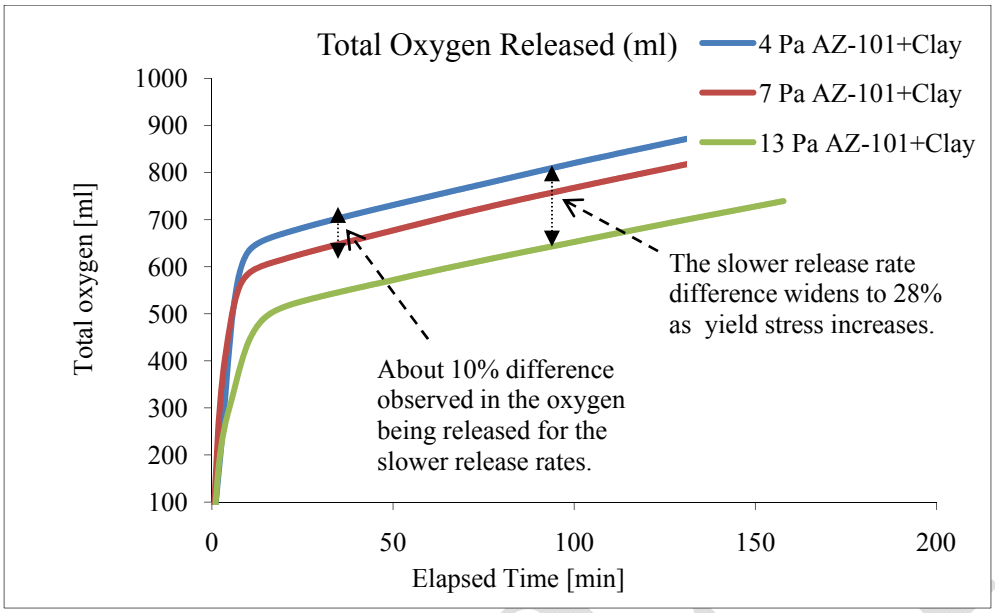

Figure 59. Total oxygen released during the release test of 4 Pa and 7 Pa for AZ-101+Clay mix.

Table 16 summarizes the more important parameters that have been determined from the experimental program.

Table 16. Summary of Release Parameters for AZ-101+Clay Simulant

Test	Simulant	Yield Stress Pa	k_1 min^{-1}	k_2 min^{-1}	Final Holdup without AFA %	O_2 released[2] %
A01	AZ-101+Clay	4	0.36	0.01	4.6	66
A02	AZ-101+Clay	7	0.32	0.02	4.0	70
A03	AZ-101+Clay	13	0.18	0.03	3.6	65

With AFA

The gel hold-up levels achieved during these tests and released volumes are summarized in Table 17 and compared with the results of tests without AFA. The hold-up levels were estimated from the effluent gas oxygen and nitrogen concentrations and the purge gas injection rates.

[2] Percentage of oxygen released in the first 15 minutes.

Table 17. Summary of In-situ Gas Retention and Release Test Results for AZ-101+Clay Mix with AFA

Test	Simulant	Yield Stress Pa	AFA concentration ppm	Final Holdup without AFA %	Final Holdup with AFA %
B01	AZ-101+clay	4	350	4.59	5.22
B02	AZ-101+clay	7	350	4.00	6.17
B03	AZ-101+clay	13	350	3.59	4.32

A typical release signature curve is shown in Figure 60 for the 4 Pa test with AFA.

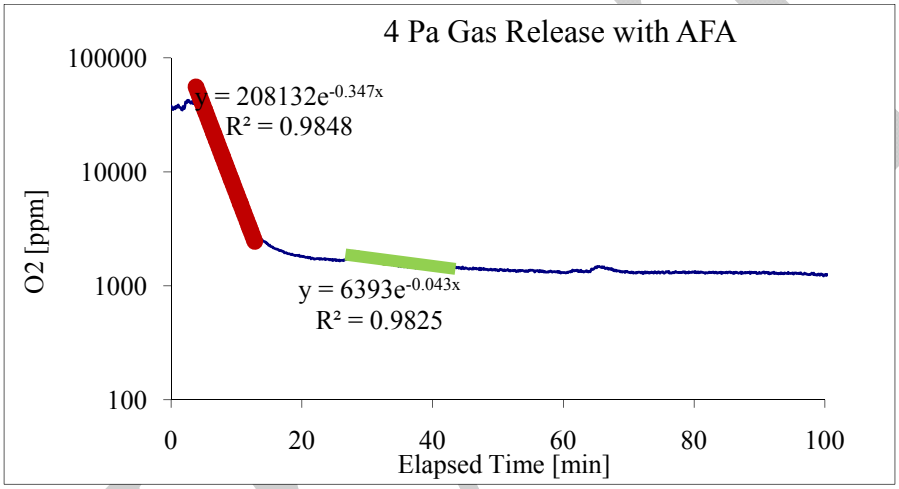

Figure 60. Release Profile of the 4 Pa with AFA Test.

Figure 61 shows the comparison of the release profiles for the 4 Pa test with and without AFA.

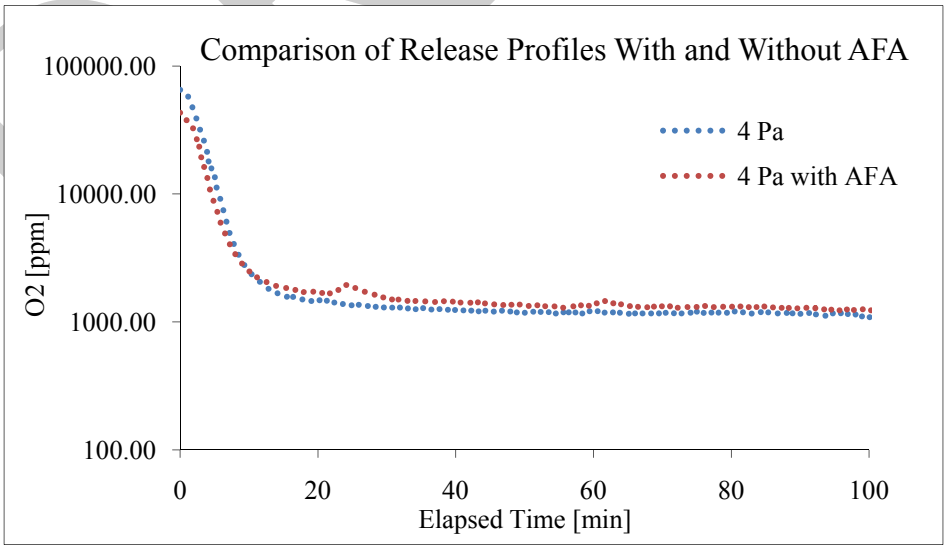

Figure 61. Comparison of release curves with and without AFA for 4 Pa.

The release rates for the tests with and without AFA for 4 Pa were very similar. The 4 Pa without AFA released the gas at the rate of 0.38 min^{-1} compared to the rate of 0.36 min^{-1} observed in the tests with AFA. A majority of the gas was released within the first 10 minutes in both cases (Figure 62).

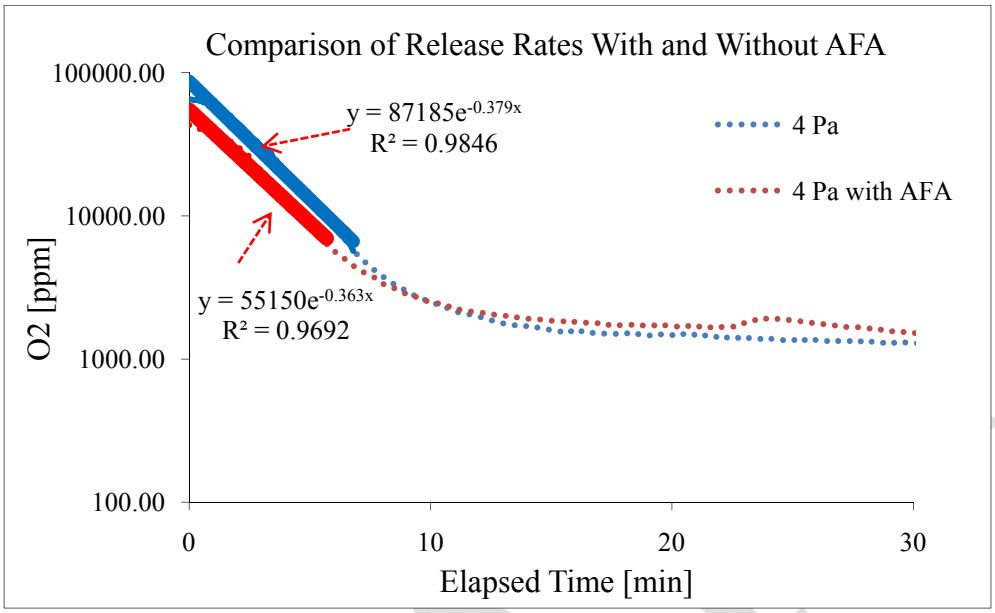

Figure 62. Comparison of release rates for 4 Pa tests with and without AFA.

Figure 63 shows the comparison of the cumulative volume of oxygen released from the gelled state for the 4, 7 and 13 Pa tests with AFA. The profiles look very similar even though the simulants vary in rheology.

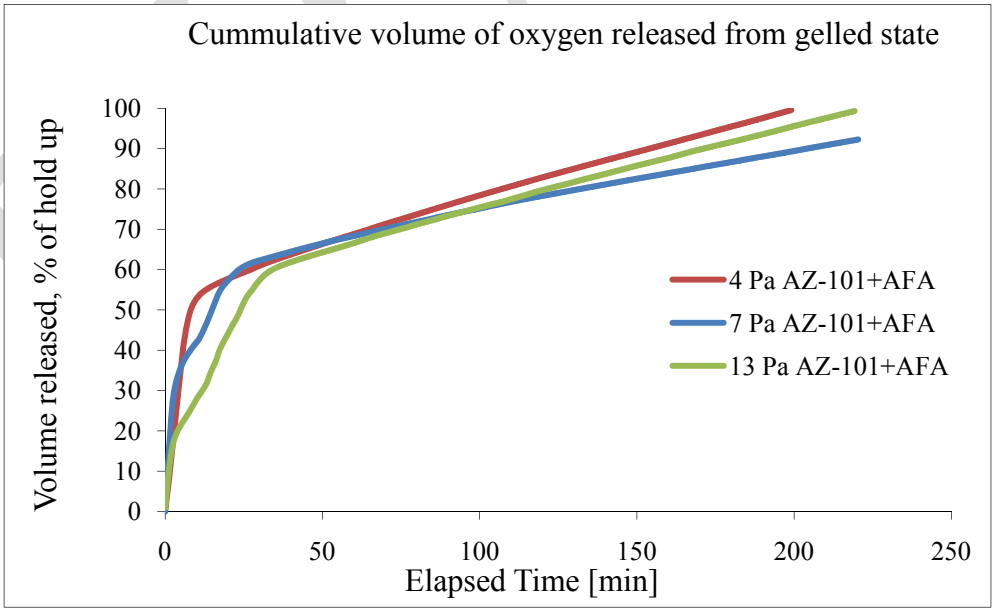

Figure 63. Comparison of release profiles for tests with AFA.

Even though the profiles of the total volume of oxygen released with AFA looked similar (Figure 63), when the results of tests with AFA were compared with the results of tests without AFA, a

clear trend could be observed. Table 18 summarizes the more important parameters that have been determined from the experimental program.

Table 18. Comparison of Release Parameters of AZ-101+Clay Mix with AFA

Test	Simulant	Yield Stress Pa	k_1(without AFA) min^{-1}	k_1(with AFA) min^{-1}	k_2(without AFA) min^{-1}	k_2(with AFA) min^{-1}
B01	AZ-101+clay	4	0.36	0.35	0.01	0.01
B02	AZ-101+clay	7	0.33	0.38	0.01	0.02
B03	AZ-101+clay	13	0.176	0.43	0.02	0.03

The following observations were made from the 4-13 Pa tests with AZ-101+clay mix with AFA:

- The tests with AFA revealed that the in-situ generated gas was released at two different rates each with its own peak and rate constant. The faster rate was associated with the mobilization of column contents and the slower rate was associated with the dissolution of the gas.
- The addition of AFA increased the gas hold-up by 33% for the 4 Pa tests, by 11% for the 7 Pa and 20% for the 13 Pa tests compared to the results of tests without AFA.
- The gas release rates for tests with AFA were faster than the tests without AFA. The 13 Pa test without AFA released gas at the rate of 0.17 min^{-1} compared to the 0.43 min^{-1} with AFA. The release rates for the 4-7 Pa test were similar.

OVERALL PROJECT CONCLUSIONS

The experimental program initiated at FIU extended experimental studies previously conducted at SRS and PNNL by addressing the transient behavior of gas release, retention and release patterns for mixtures with yield stress parameter ranging from 2-13 Pa. Two simulants with varying rheology were tested: (s) kaolin-bentonite (2, 4, 7, 10 and 13 Pa) and (b) AZ-101+clay mix (4, 7 and 13 Pa). The tests aimed to quantify the gas retention and release characteristics for these low yield stress non-newtonian simulants.

The following observations were made from the test program:

Release rates:

- The in-situ generated gas release was characterized by two release rates, each with a different peak rate and time constant: (1) a faster release rate with a shorter time constant due to direct mobilization of the slurry and release of the larger bubbles (2) a slower release rate with a longer time constant representing release of dissolved oxygen gas.
- For clay simulants, the 2 Pa clay simulant had an initial hold-up of 8.4% and released the gas at the rate of 0.49 min^{-1} compared to the 2.6% observed at 13 Pa which released the gas at a much slower initial rate of 0.37 min^{-1}.
- The gas release rates for tests with AFA were faster than the tests without AFA for clay simulants. The 7 Pa clay simulant with AFA took about 10 minutes to release 90% of the total hold-up compared to 75% of the gas released by the 7 Pa simulant without AFA.
- About 60-90% gas was released within the first 20 minutes upon commencement of mixing of the gelled simulant and all of the gas was released within 200 minutes.

Rheology:

- As the yield stress increased the gas hold-up decreased for both clay and AZ-101+clay simulants.
- The gas hold-up achieved was less for the AZ-101+clay simulant compared to the clay simulant for similar yield stress and testing conditions. The 4 Pa clay simulant had an initial gas hold up of 6.5% compared to the 4.5% observed in the AZ-101+clay simulant.

Addition of AFA

- The addition of AFA increased the gas hold-up by 10% for the 2 and 4 Pa test and about 50% for the 7, 10 and 13 Pa tests for clay simulants compared to the tests without AFA.

Tests with AZ-101+clay mix simulants reported an increase in the gas hold-up by 33% for the 4 Pa tests, by 11% for the 7 Pa and 20% for the 13 Pa tests compared to the results of tests without AFA.

REFERENCES

1. C. W. Stewart, P.A. Meyer, M.S. Fountain, C.E. Guzman-Leong, S.A. Hartley-McBride, J.L. Huckaby, and B.E. Wells, "Effect of Anti-Foam Agent on Gas Retention and Release Behavior in Simulated High Level Waste," WTP-RPT-147 Rev. 0, Battelle – Pacific Northwest Division, Richland, Washington, 2006.
2. C. W. Stewart, C.E. Guzman-Leong, S. T. Arm, Butcher, M.G. Butcher, E.C. Golovich, L.K. Jagoda, W.R. Park, R.W. Slaugh, Y.Su, C.F. Wend, L.A. Mahoney, Alzheimer, J.M. Alzheimer, J.A. Bailey, S.K. Cooley, D.E. Hurley, C.D. Johnson, L.D. Reid, H.D. Smith, B. E. Wells, S. T. Yokuda, " Results of Large Scale Testing on Effects of Antifoam Agent on Gas Retention and Release, "PNNL-17170, WTP-RPT-156 Rev. 0, 2008.
3. H. Guerrero, M.M. Fowley, C.C. Crawford, M., M. Restivo, and R.R. Leishear, "Effects Of Alternate Antifoam Agents, Noble Metals, Mixing Systems And Mass Transfer On Gas Holdup And Release From Non-Newtonian Slurries," WSRC-STI-2007-00537, 2007.
4. A. P. Poloski et al. "Non-Newtonian Slurry Simulant Development and Selection for Pulse Jet Mixer Testing," WTP-RPT-111 Rev 0, pp. 41-47, 2004.
5. D. Roelant et al. "Chemical Process Alternatives for Radioactive Waste," FY09 Year End Technical Report, pp. 174-178, 2010.

APPENDIX A.

1. Calibration of Mass Spectrometer

Calibration for the mass spectrometer from Hidden Analytical Instruments (HA-085-005) was performed on April 15, 2010 in the Slurry lab (EC 2110) by Romani Patel. The calibration gases were purchased from Air Gas Instruments. Statistical values are provided in Table 19, Table 20 and Table 21 for each of the three mixtures tested.

The following mixture of argon gas in nitrogen was used to calibrate the instrument.

1. 100 ppm of Ar
2. 500 ppm of Ar
3. 5000 ppm of Ar

Table 19. Statistical Values for 100 ppm of Argon in Nitrogen

	Statistical Values
Mean	6.95E-05
Standard Error	8.61E-07
Median	6.92E-05
Mode	#N/A
Standard Deviation	1.13E-05
Sample Variance	0
Kurtosis	3.666769
Skewness	0.960436
Minimum Range	4.95E-05
Maximum Range	0.00013
Sum	0.011941
Count	171
Confidence Level(95.0%)	1.69E-06

Table 20. Statistical Values for 500 ppm of Argon in Nitrogen

	Statistical Values
Mean	0.000681526
Standard Error	2.44556E-06
Median	0.000681
Mode	#N/A
Standard Deviation	2.84148E-05
Sample Variance	8.074E-10

Kurtosis	-0.832252304
Skewness	0.167173076
Minimum Range	0.000625
Maximum Range	0.000749
Sum	0.092006
Count	135
Confidence Level(95.0%)	4.7932E-06

Table 21. Statistical Values for 5000 ppm of Argon in Nitrogen

	Statistical Values
Mean	0.00652
Standard Error	1.16E-05
Median	0.0065
Mode	#N/A
Standard Deviation	0.000149
Sample Variance	2.21E-08
Kurtosis	0.648894
Skewness	0.807107
Minimum Range	0.00628
Maximum Range	0.00703
Sum	1.06925
Count	164
Confidence Level (95.0%)	2.27E-05

A calibration curve was determined between argon concentration in the calibration gases and argon/nitrogen ratio value as shown in Figure 64.

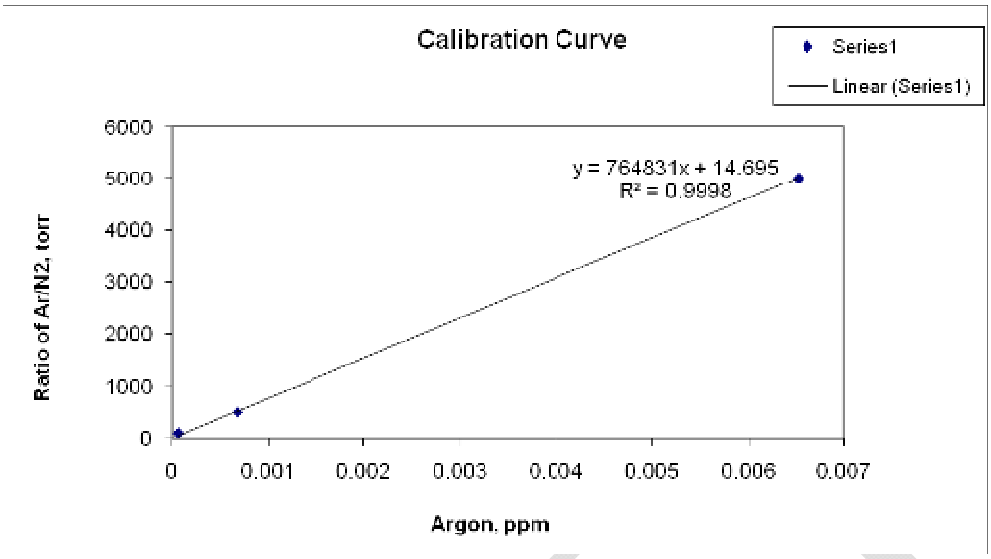

Figure 64. Calibration curve of argon in nitrogen at various concentrations.

2. Mass Balance of Gases

Mass balance of argon and nitrogen gases was done in order to account for the gases entering and leaving the experimental set-up. The column was filled with 60 inches of water and argon was passed into the column at the flow rate of 1500 ml/min and nitrogen over a range of 3000-5000 ml/min. A steady state was achieved within 3 minutes. The inlet flow rate was controlled via a Brooks mass flow controller, whereas the effluent flow rates were recorded via a flow meter by Omega. Figure 65 and Figure 66 show the mass balance for argon and nitrogen, respectively, and Figure 67 shows the mass balance for the mixture of the two gases.

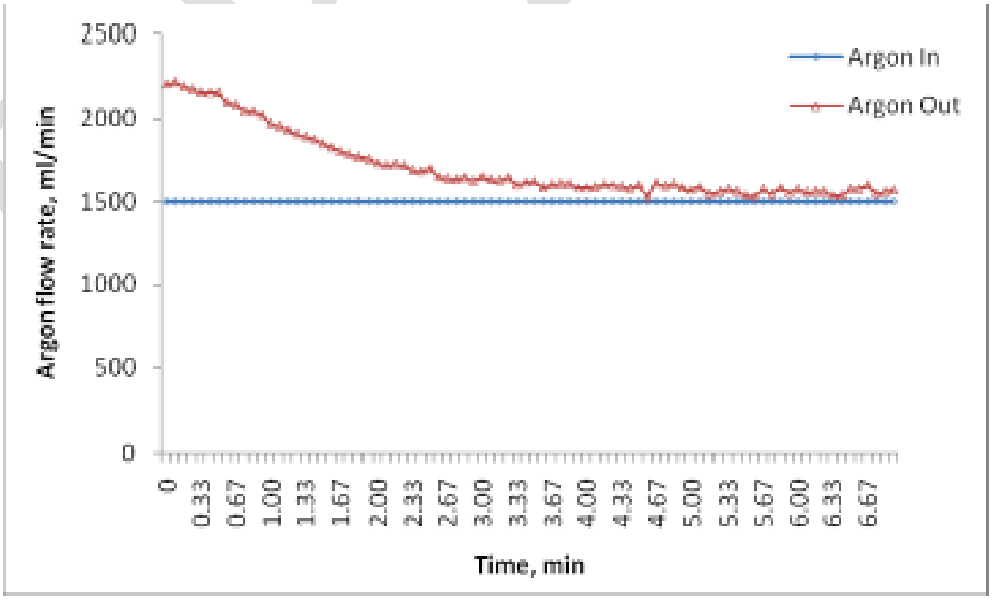

Figure 65. Mass balance of argon.

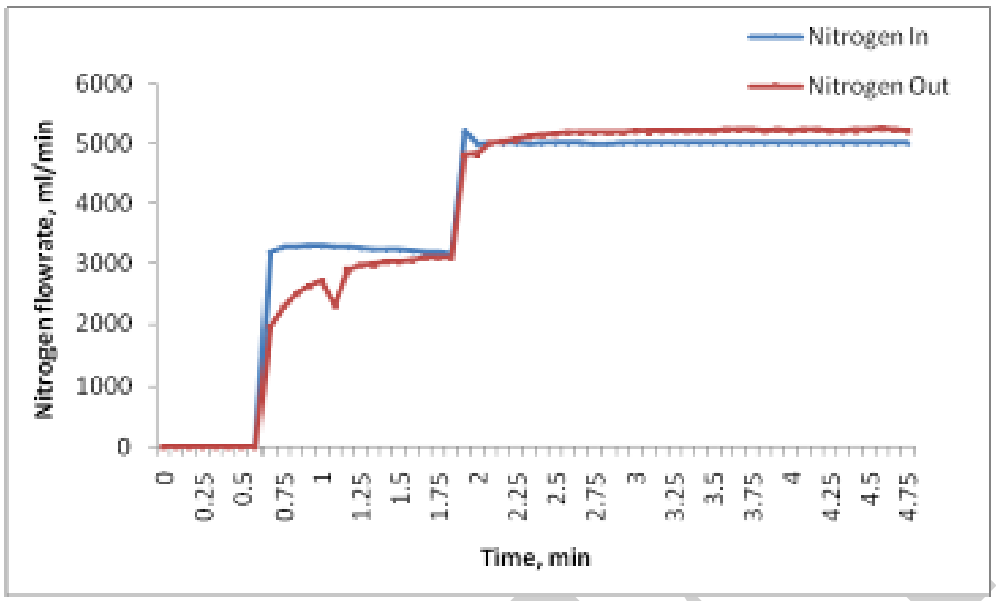

Figure 66. Mass balance of nitrogen.

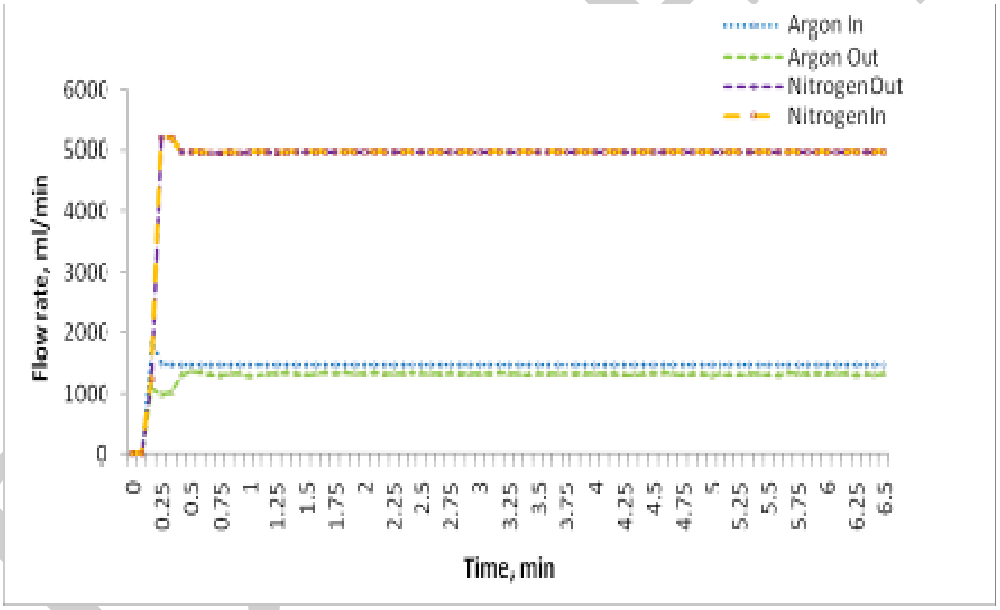

Figure 67. Mass balance of argon-nitrogen mix.

TASK 15 FY10 YEAR END TECHNICAL REPORT Evaluation of Advanced Instrumentation Needs for HLW Retrieval

EXECUTIVE SUMMARY

As the DOE's Hanford site begins preparations for the transfer of high-level waste (HLW) from double-shell tanks (DST) to the Waste Treatment and Immobilization Plant (WTP), the influence of waste feed consistency on the final stabilized waste form is currently under analysis. In order to characterize feed consistency, a suite of instrumentation will be required to monitor the waste preparation and mixing process in real time. FIU has focused its instrumentation efforts during this performance period on the improving the in-situ, near-real time monitoring of the mixing process. This task worked with personnel responsible for the preparation of waste feed into the WTP in identifying innovative technologies applicable for in-tank monitoring during the mixing process.

This task began with a review of the current state of technology applicable to the monitoring of HLW feed during the mixing and transfer process. The review examined the previous works by PNNL, the site contractors, and academia in identifying and implementing technologies that can monitor critical physical and rheological parameters of the waste. Discussions with site representatives established the current technology implementation plan for the double-shell tanks that will be used to stage waste feed for WTP; these discussions were also a reference to minimize duplicative efforts into areas that had already been evaluated by other parties.

After the current technology baseline plan and previous research efforts were reviewed, FIU began an extensive literature and technology search for applicable systems that could provide waste parameters within the HLW tank environment. The literature search focused on available methodologies for in-situ analysis of slurries, emulsions and suspensions applied in all industries. In particular, the monitoring of bulk density and/or particle concentration/characteristics measurements was the focus of the search. For the technology search, vendors of applicable techniques were identified and contacted. The searches resulted in several academic, commercial and governmental reports/articles applicable to the monitoring needs of the HLW tanks. Instrumentation specifications were collected and reviewed to identify the technology capabilities and limitations. These capabilities were also used for a comparative analysis between technologies. Based on the information, all the technologies were down selected to five applicable systems/methods that could provide useful information if deployed in a HLW tank. The five applicable methods applicable to the in-situ monitoring of the waste feed consistency were focused beam reflectance measurement (FBRM), optical back-reflectance measurement (ORM), ultrasonic spectroscopy (USS), Lamb/Stoneley wave viscosity measurement, and vibration-based densitometers. Based on literature results and commercial options, the ultrasonic and vibration-based techniques showed the most promise for developing a technology that could be used for in-situ measurements within the aggressive environment of a HLW tank. Specifically, the vibration-based and USS systems can provide information on the density and concentrations of the mixed slurry. These techniques can be engineered for monitoring at various depths within the tank.

Once the most promising techniques were selected, an experimental approach was defined. The approach would look at technology monitoring limitations in two phases; phase I would determine how the technologies could measure the slurry parameter, and how that measurement compared to laboratory or baseline techniques. This phase would be used as a go/no-go point to determine if further investigation into the technology is warranted. The second phase (in FY11) would focus on which specific factors and interactions would influence the measurement (particle size, carrier fluid density, etc). The USS would be compared to a commercially available density meter that utilizes an accurate and repeatable technique for density measurement. A setup was conceived that allowed the testing of the USS and a commercially-available Coriolis mass flow meter side-by-side. The setup used a 10-gallon tank for agitation of the simulated slurry mixtures, with both systems sampling at the same location; the USS system probe was lowered into the tank, while a pick-up tube was used to transfer mixture to the Coriolis meter. In addition, the USS was subjected to several tests using a benchtop setup for more controlled evaluations of its concentration tracking capabilities. Both these systems were subjected to solutions and suspensions that would simulate the extreme bounds of the physical and rheological properties of the HLW slurry found in AZ-102. The simulated slurries consisted of one to three distinct solids suspended in a water or $NaNO_3$ solution as the supernatant.

The USS system was installed, and training performed by ITS employee in early April. The system had several technical issues at the outset, particularly relating to the software performance. The USS was subjected to concentration ladders of solid $Al(OH)_3$ in a ultrapure reverse osmosis/de-ionized water supernatant to evaluate its ability to tracks changes in concentration in a suspension. Several of the tests determined that software issues were calculating incorrect values for the separation and delay in the time-of-flight measurements, giving large errors in ultrasonic group velocity measurement. The technical issues delayed the completion of phase I testing the USS. The testing will continue into the early part of FY11, with possible follow-up phase II testing that will focus on the effects of particle physical characteristics on performance of the system. In addition, an engineering evaluation of the system in its current incarnation will be performed to determine the necessary changes before the system could be deployed in a HLW tank.

INTRODUCTION

The US Department of Energy's (DOE) Hanford site is completing development of the Waste Treatment and Immobilization Plant (WTP), and preparing for the processing of over 54 million gallons of high-level radioactive waste (HLW). This waste shall be mixed within storage tanks, transferred to staging tanks, and processed by the WTP for final disposal. As the WTP development is completed, the window to integrate additional instrumented systems into the process loop will close. One such area that could benefit from additional instrumentation is the HLW tanks where this waste is currently stored. These +1M gallons of waste must be mixed into slurry that can be retrieved via pipelines to other tanks, or to WTP. The ability to characterize slurry in-tank would greatly optimize the mixing and retrieval processes. After several years of experience in the development of remote monitors for HLW tanks, FIU has undertaken a task to evaluate additional characterization and monitoring technologies that could be scaled-up for deployment inside the HLW tanks at Hanford.

As Hanford and PNNL perform laboratory testing of the slurry mixing phenomenon with various technologies, as well as the effect of slurry rheology on the mixing process, the inability to maintain a homogeneous mixture in a larger scale is evident. The recent analysis of AZ-101 transfer performed in 2001 concluded that less than a third of the particulate required for a homogeneous mixture were actually suspended during mixing [1]. When this is looked at from the perspective of a HLW feed that will be provided to WTP, the potential for variability in the slurry properties as it enters WTP could greatly impact the process throughput, even for waste from the same tank.

The Process Technology hot cells at WTP currently do not hold sufficient instrumentation to perform the types of analysis necessary for feed pre-qualification. Also, no pre-qualification criteria for the feed slurry has been defined as of yet. Several waste slurry characterizations have been recommended for compositional analysis and rheological properties [2]. In order to accomplish these characterizations prior to retrieval, an instrumented flow loop located above the tank will be added to the output from the tank feed pump. This would allow for characterization of several rheological properties as the waste is being mixed, retrieved, and proceeds to staging tanks at WTP. Also, additional sampling and laboratory analysis of samples extracted from the mixed tank shall also be used for compositional and rheological characterization. Technologies such as laser diffraction, ultrasonic doppler velocitometry (UDV), ultrasonics (US) densitiometry, Coriolis meters, Raman spectroscopy and XRD will be included in these two sampling scenarios.

The two characterization methods can be supplemented with additional capability for in-tank characterization. The ability to either compare retrieve slurry with in-tank measurements, or provide supplemental information on slurry composition/properties could potentially save time and costs in the WTP process loop by allowing operators to make changes to mixed slurry – or the mixing process itself - prior to staging at WTP. The appropriate technology deployed in the HLW tanks could estimate the amount of mixing that is occurring within the tank in real-time, which can help address issues with solids level suspension, as well as characterization of the mixture as a function of tank height. This supplemental characterization and monitoring scenario is the focus of this task. Specifically, this task will search evaluate and test potential technologies that could be deployed within the tank to provide slurry parametric data to site operators.

Based on the discussions with the site representatives from WRPS, several general instrumentation guidelines were established. FIU used these to evaluate promising in-situ candidate technologies. The guidelines were focused on deployment and operation in the HLW tanks. The guidelines were,

- Operate in an in-tank configuration within the chemical, physical and radiological-aggressive tank environment
- Sample and characterize while tank mixers are operating (fluid motion, electrical/acoustic noise, vibration, etc)
- Work around/with air lift circulators
- Bench-scale performance can be correlated to real-world scaled-up operation
- Ability to measure vertical profile of a particular parameter (e.g. solids concentration, bulk density); ability to use data from multiple probe locations to generate parameter maps (interpolation can be used)
- Ability to measure solids parameters of those being suspended from those stationary (size, composition, density, etc)

LITERATURE & TECHNOLOGY REVIEW

A reference literature review was initially performed to determine what techniques or technologies had been tested in the past. Also, a review of technologies planned for deployment in a planned instrumentation loop and hot cell was also performed to better understand what types of systems have been validated for the HLW environments. This provided a framework for operating principles that could be viable in-situ.

A list of possible analysis scenarios were used as the search queries in several information repositories [provided in Appendix A]. Although this list is not all-encompassing, it covered the general topics that had been found as part of the reference information and initial technology literature review. When the technology guidelines were discussed with Hanford, it was within the context of commercial systems that could be deployed into HLW tanks in the near-future (< 3 years). The initial literature search found many techniques that could be applicable if additional research and development efforts were dedicated to them. These techniques were not discounted from the candidate lists, and were left as possible long term (> 3 yr) techniques that can be further evaluated within a laboratory setting.

The literature search was performed using several information repositories available on the World Wide Web (WWW). These repositories are accessible through a main search engine provided by Google. The Scholar engine (scholar.google.com) performs full-text queries on all major academic information repositories, as well as national laboratory and patent document repositories. The Scholar engine was used with the search queries list developed. In addition, the US DOE's OSTI Information Bridge and Science Accelerator was also used to perform search queries. Finally, use of the State of Florida library system journal article search was also employed.

The literature search yielded several techniques and technologies that can be used for in-situ analysis of suspensions, emulsions and slurries. The literature search results were reviewed within the framework of what could be deployed in a practical configuration for the tank. Techniques that required either on-board electronics, precise optics near the measurement window, or power/energy sources within the tank were not considered. Techniques that had the potential for reconfiguration for in-tank deployment were also reviewed, as additional research effort could lead to a useful technology.

Based on the literature search, thirteen techniques/technologies were found that showed promise for the in-situ application, although their measurement results fell into three distinct categories. The results could provide measurement of particle physical characteristics (microscopic characterization), chemical composition (signature), or slurry characteristics (macroscopic characterization). The technologies relied on electromagnetic, acoustic or optical principles for their main transduction process. Also, the candidate technologies lacked comparable characteristics on which to evaluate side-by-side on the potential for in-tank application. The evaluation was performed as an individual, stand-alone qualitative assessment of possible in-situ performance based on the literature obtained during the search.

The candidate technologies described below have been reviewed through literature review, communication with commercial vendors, and/or interaction with academic contacts that have worked with the technologies. A more detailed review spreadsheet is provided, which contains

all the technologies that were reviewed. The technologies/techniques provided herein show the greatest promise in moving from their current incarnation into a scalable technology for the HLW tanks.

Focused Beam Reflectance Measurement (FBRM)

The FBRM technique focuses an infrared (IR) laser beam through a sapphire window in contact with the system to be measured. The laser optics are rotated at a controlled high-speed so the focused beam can scan across the system in a circular path. This focused beam reflects light when it traverses along the body of particles passing through the scanning circle. The reflection time, when used in conjunction with the scanning velocity, can be used to calculate a chord length for the particles. Several thousand of these measurements can be taken per second, providing a chord distribution length (CLD) along 128 pre-defined channels. Various analytical techniques have been used to correlate the CLD to a particle size distribution (PSD). Some of the major advantages of the technique are: the in-situ capabilities, the limited components to deploy, and the simplicity of the process. Major disadvantages with the system are: windows exposed to medium can foul, which will lead to erroneous CLD; larger particles can block the detection of smaller particles, leading to a CLD skew towards larger particle ranges; accurate CLD requires window to be in dominant flow direction. This technique has been previously deployed in-line at ORNL and Hanford for slurry monitoring. No information was found on the current use of the technology at Hanford in the in-tank configuration.

Optical Back-Reflectance Measurement (ORM)

The ORM technique focuses a rotating laser beam to preset ranges outside of a window, which is in contact with the system to be measured. The laser setup is configured for a single scan mode, thereby reducing the multi-scattering effects of systems that are focused at the sensing window. An additional capability of selective multi-depth focus (3D SMF) allows for the focus to be adjusted by changing the laser pulse characteristics. This technology shares many similarities with the FBRM with the distinction being with the use of small (4 um) single-mode fiber for the optical transmission/reception. This could potentially reduce the noise and scattered light that can be injected into a multi-mode fiber. The major advantages for this technology are: smaller focused beam leads to detection of smaller particle sizes; available in an in-situ packages; and contains limited components in deployment form. Major disadvantages are the same as FBRM, also no information on technology deployments could be found.

Ultrasonic Spectroscopy (USS)

Method measures the change in ultrasonic signal per unit distance at various interrogation frequencies. For the ultrasonic method, the USS can measure the absolute frequency-dependent velocity and attenuation of liquids and soft solids. This is accomplished by measuring the change in ultrasonic amplitude and phase of the wave over a known path length. In addition, the system also measures reflection of the ultrasonic wave, a value that can be used to determine the density of the media under test. The interaction of the wave with the material is a function of the material structure including hydrodynamic and the thermo-elastic properties. Therefore, ultrasonic spectroscopy data can be used to characterize any process which modifies these parameters including the process kinetics, solids concentration, rheological behavior and changes in particle size or material structure. The technology (Figure 1) is in the form of an in-situ probe that can be placed directly into the process vessel. A small sensing zone at the bottom of the probe (Figure

2) provides the transducer pair necessary for velocity time-of-flight and attenuation measurement, as well as a temperature sensor for measurement correction. This causes an energy loss in the wave that is characteristics of the material properties, namely viscosity and density. This technique has been applied in several in-situ applications for dairy products mixing. Similar to other US techniques for slurry characterization, this is not limited by the opacity and solids loading of the mixture. This technique can be applied in an in-situ configuration, although the commercially available system has only been deployed in small beakers and reactors. Major advantages for this technology are: performs direct bulk density and viscosity measurement, requires simple transmitter-receiver pair configuration, and data can be used for trending on mixing process homogeneity. Major disadvantages include: lack of in-situ system for tank application, requires reference standards for determination of appropriate waste parameters, and susceptible to electrical noise from pump operation.

Figure 68. USS Probe

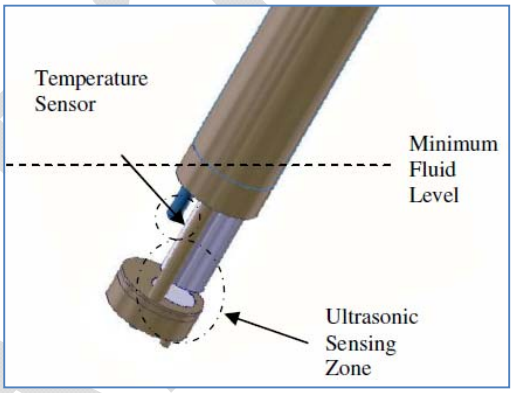

Figure 69. Probe close-up drawing of sensing zone (Courtesy of Industrial Tomography Systems plc).

Lamb (Stoneley) Wave Viscosity Measurement

This method utilizes shear waves along the interface between liquid and solid media and the wave equation to determine viscosity of the liquid media. Waves can be applied as a Lamb wave (at end of a waveguide), or completely along the interface (Stoneley). This technique has been used in a laboratory for viscosity measurement of a liquid media by submerging the waveguide into the media. Major advantages include: requires simple sensing electrode and electronics modules and no field calibration necessary. Major disadvantages include: no in-situ configuration currently available, limited viscosity ranges tested to date and unknown impact of the multi-phase media on performance of technology.

Vibration-based Density Measurement

The vibration-based density measurement is a technique that utilizes the damping caused by the test material on a vibrating object(s) to determine the material properties. This method that has been utilized in industry for some time in several incarnations; these include tuning forks, twin-tube and Coriolis-force based meters. Major advantages to this method include the simplicity of the measurement principle, can be deployed in chemically aggressive environments and most systems include temperature and viscosity compensation (for slow changes of those parameters). Major disadvantages are that on-board electronics are required for temperature and viscosity

compensation/correction, fouling of the vibrating element can lead to sensitivity loss, specific types have a limited density range (tuning fork type sensors), the flow-through types can become plugged with heavy slurries, bubbles/composition changes within measurement area can cause errors, and flow pattern changes/stray currents (due to jet flow) can cause measurement errors. A tuning fork-type technology can be lowered into a mixed vessel and provide information on the density of the target. This device has a simple operating configuration that can be easily deployed with a tank/vessel. Unfortunately, the device has limited density ranges (3 g/mL maximum), which limits its usability for this particular application. Another vibration-based technology has been developed into a HLW-tank deployable configuration by FIU. This technology provides not only the slurry bulk density, but can also provide the solids concentration of the slurry sample. The in-tank solids monitor (ITSM) sampling system consists of two Coriolis meters, a crossflow filter, and a flow control valve. The operating principle behind the Coriolis meter is that when a fluid enters a vibrating tube, it will accelerate/decelerate as it reaches/leaves the central point of the tube. This applied force causes a deflection, or twist, that is directly proportional to mass flow [6]. The Coriolis meters measure the density, mass flow, viscosity, and temperature of the fluid under test. This unit can be modified to only collect information on the bulk density of the slurry solution.

Commercial Options

Based on the literature results, a commercial vendor search was also performed for the techniques found. Several vendors that fabricated technologies utilizing these techniques were identified. Several vendors had existing technology whose state of maturity suggested the potential for a tank deployable system within the near-term (< 3 yrs). Some examples are the FBRM system developed by Mettler-Toledo AutoChem, the ORM ("Lasertrack"/"iPas") from HEL Group/Sequip, the USS system from ITOMS, and vibration-based monitors from various manufacturers. Both optical systems are used in industrial reactors (albeit small ones), and can be scaled up for large scale tanks (as per company representatives). The primary drawbacks with their current manifestations are the ability to monitor various tank depths, as well as the correlation of CLD to PSD. There are several engineering challenges facing a tank-deployable version that allows for multi-depth measurement; the fiber-based signals cannot be easily decoupled for vertical movement of the probe. The USS technique lacks a large-scale in-situ configuration, although engineering efforts to develop a multi-detector "tank-friendly" configuration seems feasible, based on discussions with ITOMS representatives. Several in-situ systems have been developed utilizing the vibration-based method. A commercial system that consists of a tuning fork arrangement is available from Emerson Process for in-tank measurement. Another system utilizing this method is the ITSM that has been developed by FIU for in-situ solid concentration monitoring. This system deploys two Coriolis meters into the tank for near-real time slurry and filtrate density monitoring.

Most other techniques had some commercial technologies associated with their operating principle, although they lacked a configuration that would be feasible as an in-tank technology. This would require additional monetary investment and engineering effort to develop a prototype that could then be tested for viability, before looking at the scale-up aspects of the technology. Several technologies lacked the versatility to operate in anything other than controlled environments.

Lab-stage Options

The primary lab-stage technique, which requires additional research to validate the viscosity detection capabilities within the ranges required by Hanford Site operators is the Lamb (Stoneley) wave. This technique shows promise as a simple, yet robust method for viscosity measurement in-situ. The operating principle is simple enough that it could provide an additional "tree" for detecting viscosity changes at various depths. Unfortunately, only preliminary work has been performed in the application of Lamb (Stoneley) wave as a method for viscosity measurement.

Based on the literature results and commercial options, the ultrasonic and vibration-based techniques showed the most promise for developing a technology that can be used for direct measurement in-situ. Specifically, the vibration-based and USS systems can provide information on the density and viscosity of the mixed slurry. These techniques can be useful in-situ methods for collecting additional data on the slurry conditions at various depths in the tank.

EXPERIMENTAL APPROACH

A test strategy was developed that could assess how a technology could handle the physical characteristics of the slurry media in which it would be deployed, before evaluating the technology readiness aspects of the system. The tests to perform would consist of a first phase that determines how accurate a technology can determine slurry characteristics, followed by a second phase – as necessary - that determines what factors and interactions most influence the measurement principle, as implemented in the technology. The first phase would act as a discrete, go/no-go stage to determine which the technologies could provide the most useful and accurate measurements for slurry characteristics, and how those measurements compare to laboratory-based measurements. The details of this test strategy are summarized below.

Operating Principles

In order to perform additional laboratory-scale qualification of the candidates, a review of the factors that could influence the technology performance was performed. Specifically, the changes in the physical, chemical and rheological properties of the target media that could influence the resulting measurement were investigated. For ultrasonic measurement systems within a suspension, it is critical to understand the media impact of the ultrasonic wave velocity, as well as the factors that influence attenuation of the pressure wave. From a phenomenon perspective [3] ultrasonic wave velocity changes within the media are directly related to changes in the effective bulk density ρ_{eff} and effective compressibility K_{eff} of the medium,

$$V = (\rho_{eff} K_{eff})^{-1/2}$$

where

$$\rho_{eff} = \varphi\rho_s + (1 - \varphi)\rho_l - 2(\rho_s - \rho_l)^2\varphi(1 - \varphi)Q/(Q^2 + U^2)$$

and

$$K_{eff} = \varphi K_s + (1 - \varphi)K_l$$

ρ and K denote the density and compressibility (subscripts s and l denote solid and liquid phases, respectively), φ denotes the volume fraction, Q and U are two values calculated utilizing density, fluid viscosity, angular frequency of ultrasound, and the mean particle size.

Ultrasonic attenuation α can be described by the simplified equation

$$\alpha = \varphi\bar{\sigma}$$

where φ denotes the volume fraction and $\bar{\sigma}$ denotes the total cross section for the scatterer(s). Assuming an average particle size smaller than the ultrasonic wavelength, the total cross section of the scatterer(s) would depend on ratio of particle size to ultrasonic wavelength. Clearly, velocity changes and attenuation of the ultrasonic signal within a suspension of solid particles in a liquid media are influenced by volume fraction of particles, fluid viscosity, particle size and shape, temperature and inter-particle forces. Both these equations are very strongly influenced by particle size, as well as volume concentration. If the particle size starts to get close to the ultrasonic wavelength, or the volume concentration exceeds 10%, the effects of multiple scattering can greatly influence ultrasonic measurement performance.

For a vibration measurement system, the calculation of density is based on the following simplified equation,

$$\rho = \frac{c}{4\pi^2 V} P^2 - \frac{M}{V}$$

where c is the spring constant of the system, V is the measurement volume, P is the natural period of oscillation, and M is the mass of the vibrating element. This equation assumes a uniform mass and impact force [4]. In reality, the effect of fluid viscosity can lead to a change in flow pattern based on the movement of the vibrating element. This flow pattern change can lead to different inertial forces being exerted on the elements, which can lead to different oscillation frequencies. Also, this will be dependent on the presence of particles in the liquid. Another potential influence is the possibility of deposits forming on the surface of the vibrating element, which can lead to measurement drift based on the change of mass and measurement volume. Any concentration differences within the suspension, trapped bubbles, or stray currents (due to jet flow) can influence the resulting measurement.

Based on the influencing factors on the measurement techniques, the phase I approach is to evaluate the accuracy in measurement, and at what point will volume fraction and the effective bulk density of the suspension influence the range and resolution. In particular, the tests will determine the accuracy of the USS technique in comparison to stable, repeatable techniques for density and concentration measurement using vibration and Coriolis force principles. In addition, the tests will determine technique behavior at the upper bounds of solids loading and carrier fluid density.

The two technologies under consideration are under different phases in development. The USS technology is a commercially available unit, but is available in an in-situ package suitable for laboratory applications. The Coriolis-based vibrating densitometers are commercially available units that are designed for a multitude of application environments. The USS maturity limited the current evaluation to verification of measurement capabilities, as well as repeatability of the measurements, within a controlled laboratory environment that did not expose the probe to the rigors of a HLW tank environment. The vibrating densitometer will allow a more real-world cold test to determine utilization under varying conditions. In order to perform a comparison of the technologies, the test regime focused on validating the accuracy and repeatability of the technologies with various slurry simulants at the same scale. FIU set up a single Coriolis meter arrangement to perform measurements on the simulated slurry under test. This technology was used as the “baseline”, or reference, on which to gauge the performance and measurement accuracy of the USS.

Experimental Design

The experiments to be performed in the first phase of testing will consist of two scenarios that will be utilized to determine the capabilities of the USS in its current configuration. As a preliminary, bench-top evaluations of the USS performance for various carrier fluid densities, as well as concentration ladders with single solid media mixtures, will be performed to determine the effect on the USS attenuation, ultrasonic group velocity and density measurement. Also, the first phase of testing will include testing in a meso-scale (10 gallon) slurry simulant to collect side-by-side measurements between both technologies under consideration. This included the development of simulant slurry consistent with the physical bounds for density and primary solids particle types encountered in the AY-102 HLW tank (See Table 22). This tank will be

used as an initial staging tank for the WTP delivery, so simulants based on the current contents are used as a reference for evaluation of mixing and feed consistency.

Table 22. Hanford Tank Waste Parameters/Ranges Varied for Simulant Slurries

Parameter	Range	Unit	Comments
Density (carrier fluid)	1 – 1.47	g/cc	$NaNO_3$/sugar mixture utilized to vary parameter
Density (solid)	2 – 10	g/cc	
Mean particle size	0.65 – 1000	um	
Volume UDS fraction	1 – 20	%	

The bench-top evaluations evaluated how the technology would perform when the carrier fluid density was the only changed physical factor. This change leads to resulting change in media bulk modulus, which is directly related to ultrasonic group velocity in the media by

$$C = \sqrt{\frac{1}{K\rho}}$$

The bench-top evaluations of concentration ladder looked to determine the relationship between solids loading and attenuation/velocity of the media. It was also used evaluate the concentration estimate provided by the software, which requires solid parameters (density, bulk modulus) to be provided before concentration can be calculated. As the relationship between ultrasonic group velocity and slurry concentrations is a quadratic equation, the software provides two estimates of the concentration.

The meso-scale evaluations provided side-by-side comparison of the bulk density measurements of both the USS and the Coriolis meter system within the same slurry simulant. In addition, this allows additional examination of how well both technologies can track the mixing plume as the mixing is started/stopped, and the resulting fluctuations in bulk density as the mixture becomes consistent.

Experimental Loop

The experimental loop (Figure 70 and Figure 71) consists of a mixing tank with three jets for agitation, and a single intake located near the fluid/air interface. The mixing process is driven by a 1HP centrifugal pump. The mixing vortex is controlled using a main gate valve and ball valves located on each jet. The simulated slurry temperature is controlled through the use of a pipe-in-pipe heat exchanger using chilled water as the thermal sink. In addition to this setup, an additional bench-top system is used for troubleshooting and small scale validation tests. The setup (Figure 72) utilizes a magnetic stirrer/heater plate to agitate the media and control the temperature.

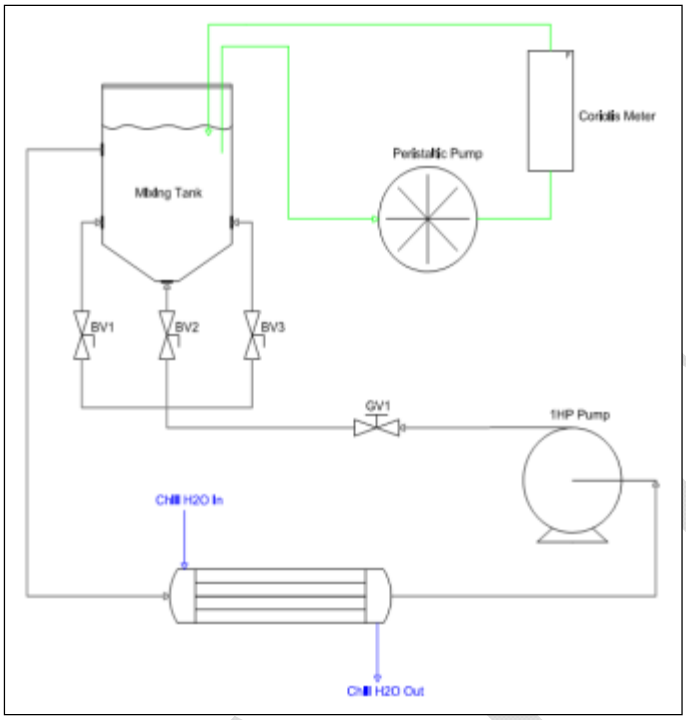

Figure 70. Mixing and sampling loop diagram.

Figure 71. Sampling loop at FIU. The sampling pump and Coriolis meter are visible in the center and top of the image.

Figure 72. Benchtop test setup. Preliminary solids loading tests and troubleshooting were performed in this setup.

Slurry Simulants

Based on the factors that influence the performance of the two candidate technologies, an experimental matrix has been prepared that will evaluate the density techniques with slurries of varying physical and rheological properties. The slurry simulants are based on the Waste Feed Small-Scale Mixing Demonstration (SSMD) Program's simulant selection report [5], which identified simulant materials, and their respective concentrations, to obtain simulant slurry with similar specific gravity and particle bounds as the waste found in AY-102, while being a simple non-cohesive simulant. The slurry simulants will consist primarily of a $NaNO_3/H_2O$ supernatant, with the addition of particles of varying specific gravity, mean size and distribution characteristics.

The carrier fluid for all slurries was either ultrapure reverse osmosis/de-ionized water (< 0.2 um) water, or a solution of $NaNO_3$ and ultrapure RO/DI water prepared to adjust the density. Three different solids media were used for the slurries undissolved solids content. $Al(OH)_3$ (processed by Huber Materials) was used to simulate the gibbsite found in the AY-102 tank; the tank consists of 53% by volume of this material. Zirconium oxide (processed by Fisher Scientific) was used to simulate the iron oxides found in the tank; they represent 40% by volume of waste. The zirconium oxide provides a similar density as the iron oxides. Stainless steel powder (manufactured by 3DS Systems) was used to simulate the larger bounding densities and particle sizes found within the tank. It was recommended that the slurries not include some of the other solids used in the SSMD simulant (such as silicon carbide), as these represent a very small amount of the waste, and could lead to problems with mixing and damage to the mixing and sampling loop. As a base material for preliminary testing, $AL(OH)_3$ was selected for several reasons. With a mean particle size of 9 micron, and a density of 2.42, it was very easy to suspend and maintain a mixed slurry for some time after turning off the mixer. Also, the particle size was smaller than the wavelength of the USS pulse even at high frequencies, which ensured that visco-inertial/thermal absorption and scattering were the only mechanisms for energy loss. A list of

slurry simulants used is provided below. The slurries with the 'B' included in their ID were prepared and used for the bench-top tests to evaluate solids loading and USS performance.

Table 23. Slurries Prepared for Technology Assessment

Slurry ID	Solids Vol (%)	Carrier Fluid	Material Requirements			
			H_2O (gal)	$AL(OH)_3$ (kg)	ZrO_2 (kg)	SS316 (kg)
T15W0f27B	0.27	H_2O	0.524	0.013	-----	-----
T15W0f55B	0.55	H_2O	0.519	0.026	-----	-----
T15W1B	1	H_2O	0.132	0.006	-----	-----
T15W1f11B	1.11	H_2O	0.508	0.052	-----	-----
T15W2B	2	H_2O	0.132	0.012	-----	-----
T15W2	2	H_2O	9.8	1.11	1.86	0.78
T15SNW2	2	$NaNO_3$ Solution (rho = 1.15)	9.8	1.11	1.86	0.78
T15W2f30B	2.3	H_2O	0.365	0.078	-----	-----
T15W4B	4	H_2O	0.132	0.025	-----	-----
T15W4	4	H_2O	9.6	2.22	3.72	1.56
T15SNW4	4	$NaNO_3$ Solution (rho = 1.25)	9.6	2.22	3.72	1.56
T15W4f80B	4.8	H_2O	0.333	0.156	-----	-----
T15W8B	8	H_2O	0.132	0.050	-----	-----
T15W8	8	H_2O	9.2	4.43	7.43	3.10
T15SNW8	8	$NaNO_3$ Solution (rho = 1.4)	9.2	4.43	7.43	3.10
T15W11B	11	H_2O	0.269	0.312	-----	-----
T15SW16B	16	H_2O	0.106	0.105	-----	-----
T15W16	16	H_2O	8.4	8.87	14.87	6.20
T15W32B	32	H_2O	0.096	0.399	-----	-----

RESULTS & DISCUSSION

Due to several software and configuration issues related to the USS, many of the required experiments were not completed within the performance period. Experiments run thus far have focused on extracting information on attenuation and velocity changes with changes in concentration of a single solid-liquid mixture. This data was then compared to solutions with similar density values ($NaNO_3$ solutions), but with no UDS in the mixture.

USS System and Installation Setup

The USS system was set up by Industrial Tomography Systems plc (the vendor) during the last quarter of the performance period. The system (Figure 73) consists of a (1) in-situ probe, (2) controller, and (3) software installation. The controller connects to the host computer using the USB interface for serial communication. The probe connects directly to the controller through a custom quick-coupling connector. The system runs off 120 VAC electrical supply, and provides built-in noise filtering and surge protection. The probe used in these experiments came with a 1 m cable that is permanently affixed to the probe; the company representative stated that this could be modified to provide longer cabling and a quick connection option at the probe. The software platform was developed using Labview®, so no unique hardware requirements are needed to install and run the system. The necessary drivers for the hardware cards used by the controller were installed with separate installation packages prior to the USS software.

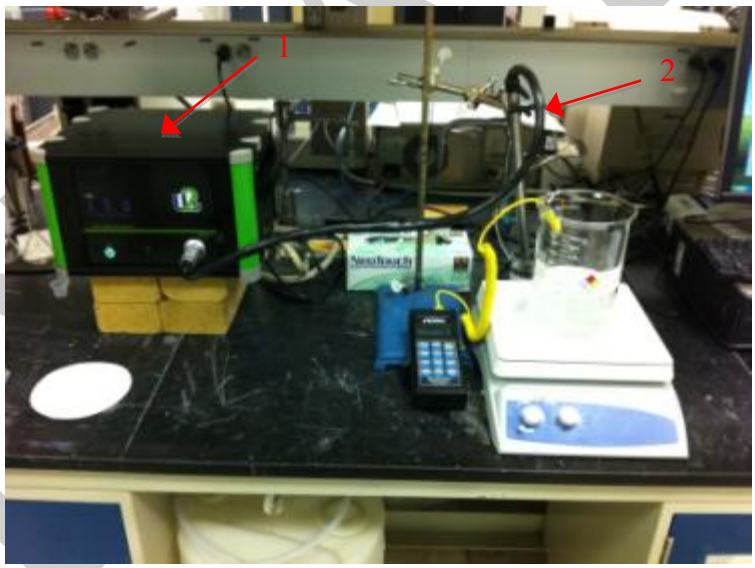

Figure 73. USS System installed in laboratory. The hardware components are shown: (1) controller, (2) probe.

The probe included various spacers to adjust the separation between the excitation element and the reflector plate. The rationale behind selection and installation of a spacer over another length is driven by the solids loading and viscosity of the media under test. If significant attenuation occurs utilizing a spacer, the separation distance can be decreased to improve echo strength. For all preliminary tests, a 40 mm spacer (Figure 74) was recommended by the company representative. After several troubleshooting issues to address several configuration problems, the spacers were replaced by 36 mm versions (Figure 75); the issues will be discussed below.

Figure 74. 40 mm spacers provided a 7.83 mm propagation path for the ultrasonic pulse.

Figure 75. 36 mm spacers reduced the propagation path to 3.83 mm, allowing for higher solids concentration in the media under test.

Preliminary Tests

In order to verify the performance of the USS system, several sodium nitrate ($NaNO_3$) solutions were prepared and used to measure the effect of changing density on liquid media with no solids suspended. It was expected that a noticeable change would occur in the ultrasonic group velocity, with no or minimal attenuation change. As expected, the system detected a shift in the ultrasonic group velocity of the solution, with very small attenuation changes (Table 24). The profile of velocity vs density change showed a linear behavior, which was the expectation in the case of a newtonian solution (Figure 78).

Several experiments were performed with suspensions of varying volume concentrations of $AL(OH)_3$. The results, provided in Table 24 show the effect of increasing solids loading on the attenuation and the ultrasonic group velocity. In particular, the solids loading between 1 – 10% shows a linear behavior, with a dramatic increase in attenuation and ultrasonic group velocity, as that ultrasonic wave is scattered by the solid particles, and the energy is absorbed by oscillations of the solid particles and thermal gradients created at the particle surface.

Table 24. Preliminary Results for Various Test Runs

Mixture description	Temp (Celsius)	density (g/cc)	Mean Attenuation at 10.2 MHz (db/cm)	Ultrasonic group velocity (m/s)
RO/DI water (standing)	21.1	0.9979	0.189	1481.95
RO/DI Water (mixing)	21.2	0.9979	0.192	1463.91
0.33M $NaNO_3$ + 5.55M H_2O	20.6	1.172	0.103	1631.16
0.50M $NaNO_3$ + 5.55M H_2O	20.3	1.226	0.073	1676.80
1.0M $NaNO_3$ + 5.55M H_2O	20.4	1.389	0.07	1818.29
T15W0f27B	21.4	---	0.745	1496.43
T15W0f55B	21.1	---	2.35	1473.8

T15W1B	20.6	1.0091	1.058	1473.187
T15W1f11B	21.3	---	1.985	1490.54
T15W2B	21.1	1.0295	2.032	1473.897
T15W2f30B	21.4	---	2.421	1480.64
T15W4B	21.2	1.0655	4.480	1473.397
T15W4f80B	19.6	---	6.369	1484.78
T15W8B	22.0	1.1181	10.553	1833.225
T15W11B	19.8	---	11.077	1829.88
T15W16B	21.4	1.2279	10.550	1840.933
T15W32B	22.2	1.4125	11.345	1840.893

It was expected that the velocity would continue to rise, as the bulk compressibility and density of the suspension continues to increase with increased solids loading. After a review of the data at the higher solids loading, it was determined that a change of the probe tip was required, as the hardware was locking onto a different echo across the entire bandwidth of the pulses. This is why the resulting profile at higher solids loading shows a different profile than expected (Figure 76).

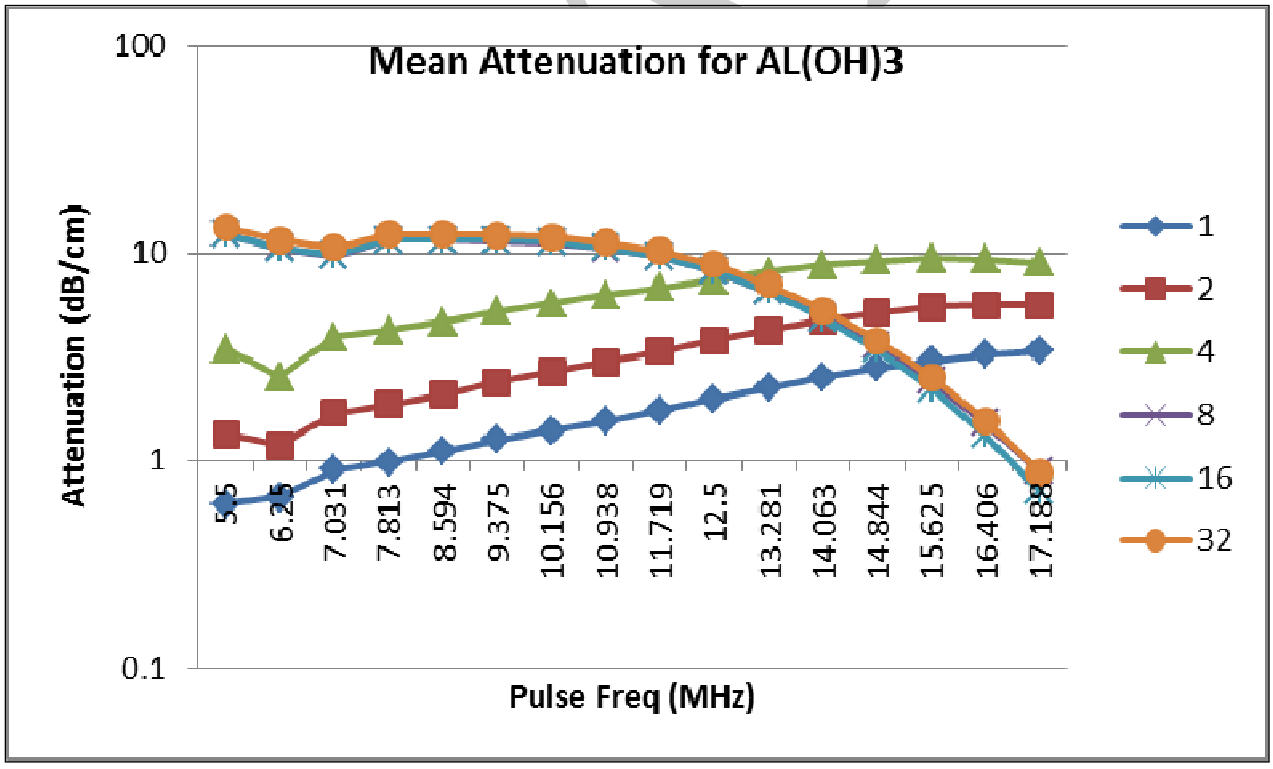

Figure 76. Attenuation versus pulse frequency for various $AL(OH)_3$ concentrations.

One interesting point is to select one pulse frequency in this linear range, and look at the profile as a function of bulk density (Figure 77). The profile is linear until a certain solids loading is reached. At this point, the effects of multiple scattering and inter-particle interaction reach a maxima in terms of attenuating the pulse. In fact, the behavior leads to the conclusion that at higher solids loading (assuming constant path length), the system would continue to provide a near-constant attenuation value at the lower frequency ranges. This behavior would change when the particle size is similar or larger than the ultrasonic pulse wavelength, as would be the case when the particle size is at the higher end of the AY-102 range (1000 um). This would lead to a very small echo.

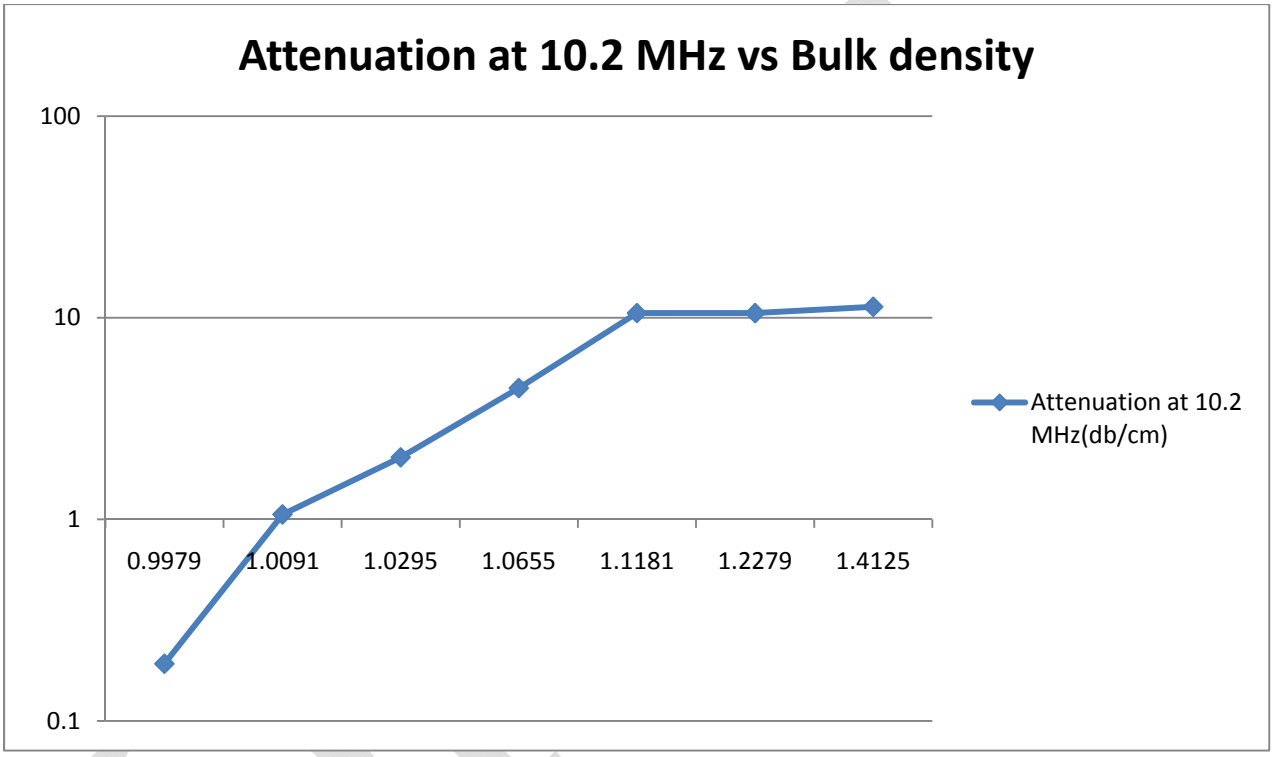

Figure 77. Attenuation profile at 10MHz pulse for varying bulk density

An investigation on the effects of ultrasonic group velocity on a solids-loaded suspension, versus a solution of similar density provides insight into the ultrasonic wave/particle interaction and effect on bulk modulus. As shown in the graph below (Figure 78), the velocity behaves in a non-linear with increased solids loading, while the change is linear with a pure liquid media. Both behaviors are in agreement with literature on the group velocity with density changes [3], although the literature suggests that the velocity will continue to rise with increasing solids loading. This discrepancy will continue to be evaluated with the testing remaining.

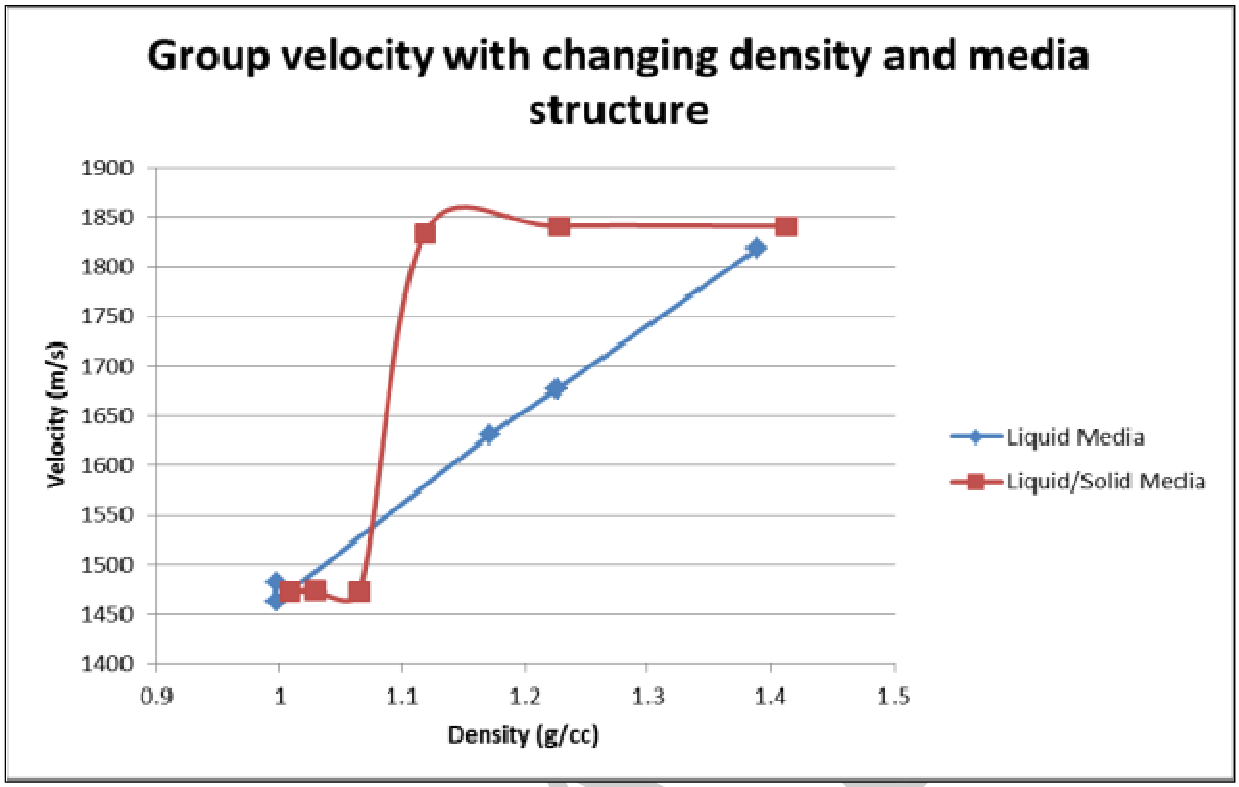

Figure 78. Relationship between liquid solution and solid/liquid suspension densities and velocity.

Configuration and Software Issues

The ITS U2S system testing is still ongoing. The system operation and testing has been contending with several software/configuration issues that have required the vendor to provide 4 different software versions to address system crashes. Also, the software in its original incarnation did not provide reflectance measurement, a component necessary to extract density measurements from the system. In this configuration, the software could only provide attenuation and velocity, and could calculate UDS concentration for single solid mixtures (solid density, and speed of sound for material required).

Initially, software installation encountered several issues when attempting it on the Windows® 7 operating system. After repeated attempts failed to provide communication between the controller and the software interface, a computer running Windows® XP was utilized, and installation was completed successfully. The software issues continued to hamper experimental runs, as the software would stop acquisition and continue to write reference values to data files. An additional software issue had to do with false triggers sent to the hardware controller from the software. This lead to large outlier measurements in the data; there was no discernable pattern to their location in the data file, and did not occur at the same time stamp. These values were included in the vectors used to calculate mean values and standard deviations. The company continues to work with FIU in addressing these issues, and a stable software version was recently sent to FIU for evaluation. Testing is expected to continue until the 16th of June to address the issues so far.

CONCLUSIONS

Although phase I testing with the USS system has not been completed, several preliminary conclusions can be drawn about the system. USS can be used track the mixing plume through changes in attenuation. The system can also utilize the velocity measurement within a small particle concentration supernate to determine the fluid density. The two measurements can be coupled to provide a wave number for the suspension at varying volume concentrations. The USS system can be useful in tracking the UDS plume as the mixing process begins, and as the suspension moves into a steady-state consistency. Attention must be paid to the maximum volume concentration that can be experienced within the mixture, as attenuation reaches a maximum around 10% solids volume and does not fluctuate much after that. For most suspensions after this maximum, the velocity will continue to rise, which results in a unique wave number for different volume concentrations.

The Woods equation relating density and ultrasonic group velocity requires the bulk modulus of media, something not easily determined for slurries with multiple solid concentrations. The advantage of the USS is that hardware configuration is such that the density of the mixture can be extracted from measurement of the reflection of the ultrasonic wave at the interface of the transducer and the media. This reflectance technique for density was utilized by PNNL for development of a pipeline density monitor [1]. Issues with temperature drift and reflectance limitations of the transducer caused issues in measurement accuracy.

A commercial Coriolis mass flow meter provides an absolute error less than ± 0.2% versus a reflectance-based error of ± 2 %. The major advantage of the USS is the simplicity of the deployment and sampling platform versus what would be required for an in-situ Coriolis-based probe. The needs for pumps, valves, flushing, and complexity of controls would be greater for the Coriolis-based system, versus the USS.

Future work could focus on improvements to the reflectance measurement through variations in reflectance scheme, improved temperature compensation for the transducer, and the utilization of alternative materials can improve the measurement error down to the range of a commercial Coriolis meter. Also, a change to the controller would be to deploy software directly on an onboard real-time OS platform, which will alleviate timing and communication faults caused by typical fairness-scheme operating systems. This configuration could be used to send data unto an existing Hanford telemetry system, without the need for a user interface.

REFERENCES

1. Bamberger, J.A., Greenwood, M.S., Development of a Density Sensor for In-Line Real-Time Process Control and Monitoring of Slurries during Radioactive Waste Retrieval and Transport Operations at DOE Sites. Richland, WA.: Pacific Northwest National Laboratory, 2001.
2. Bontha, J. R., et. al. Test Loop Demonstration and Evaluation of Slurry Transfer Line Critical Velocity Measurement Instruments. Richland, WA.: Pacific Northwest National Laboratory, 2010.
3. Harker, A. H., J.A. G. Temple. "Velocity and Attenuation of Ultrasound in Suspensions of Particles in Fluids." 21.1576-1588, 1988.
4. Lipták, Béla G. Instrument Engineers' Handbook, Fouth Edition, Volume One. Boca Raton: CRC Press, 2003.
5. Vanatta, M., "Waste Feed Delivery Small Scale Mixing Demonstration Simulant Selection Report for Phase 2 Testing", PL-SSMD-PR-0003, Rev 1, RPP-48358 Rev:0, Energy Solutions, Richland, WA, 2011.
6. Webster, J.G. The Measurement, Instrumentation, and Sensors Handbook. Boca Raton: CRC Press, 1999.

APPENDIX A

Search queries performed during literature and technology search

- ultrasonic waste slurry
- slurry velocity measurement
- slurry critical velocity
- in-situ viscosity
- in-situ density measurement
- in-situ PSD measurement
- ADCP Particle concentration
- acoustic backscattering PSD
- ERT linear probe
- linear probe tomography
- in-situ tomography
- in-situ characterization
- in-situ scattering
- in-situ spectroscopy
- in-situ thermal analysis
- in-situ thermodynamic
- in-situ particle characterization
- infrared spectroscopy in-situ
- Raman spectroscopy in-situ
- ultrasonic spectroscopy
- in situ ultrasonic
- UDV in situ
- in situ diffraction
- in situ particle size

APPENDIX B

Literature and technology search results

Technology Name	Description	Measurement Principle	Measures?	Sampling Rate (S/sec)	Measurement Range	Deployment platform	Pros	Cons	Vendor	Comments
Focused Beam Reflectance Measurement (FBRM)	The FBRM technique focuses an IR laser beam (wavelength?) to the outside surface of a sapphire window, which is in contact with the system to be measured. The laser optics are rotated at a controlled high-speed so the focused beam can scan across the system in a circular path. This focused beam reflects light when it traverses along the body of particles passing through the scanning circle. The reflection time, when used in conjunction with the scanning velocity, can be used to calculate a chord length for the particles. Several thousand of these measurements can be taken per second, with various analytical techniques used to correlate to PSD.	Optical	Chord Length Distribution (CLD)	> 1000	0.8 - 1000 um	In-vessel probe (Hastelloy C-276, Sapphire, Kalrez)	1. Various techniques for CLD to PSD correlation. 2. Fine or course electronics modules for greater edge detection 3. available in-situ configuration 4. no on-board electronics 5. Previously deployed in rad environment (ORNL, France)	1. FBRM results typically broader than other PSD techniques; can oversize small particles, and undersize large ones. Due to laser beam broadening/spreading 2. sensitive to multi-scattering effects 3. Sensitive to location and orientation in vessel; highest count when dominant flow direction towards probe measurement window 4. substances with similar index of refraction provide meaningless results	Mettler-Toledo AutoChem	Deployed at Hanford & ORNL in line configuration (factsheet provided by MT representative (P. Scholl)
Optical Back-Reflectance Measurement (ORM) / Laser Time of Reflection (TOR) Analysis	The ORM technique focuses a rotating laser beam (wavelength?) to preset ranges outside of a window, which is in contact with the system to be measured. The laser setup is configured for a single scan mode, thereby reducing the multi-scattering effects of systems that are focused at the sensing window. An additional capability of selective multi-depth focus (3D SMF) allows for the focus to be adjusted by changing the laser pulse characteristics.	Optical	Chord Length Distribution (CLD)	> 1000	< 0.5 - 4000 um	In-vessel probe (Hastelloy)	1. Capability to adjust focus location 2. single mode fiber reduces multi-scattering effects 3. available in-situ configuration 4. no on-board electronics 5. faster, farther data transmission capabilities	1. substances with similar index of refraction provide meaningless results 2. refractive particle could lead to a loss of measurement 3. little or no deployment information on technique 4. Sensitive to location and orientation in vessel; highest count when dominant flow direction towards probe measurement window	HEL Group, Inc.	Representative (B. Giordano) claims that system has improved accuracy in CLD/PSD over FBRM based on smaller, single-mode fiber filtering scattered light
Capacitance Profiling	Method measures capacitance between source electrode, and a vertical array of detector electrodes in an integrated PCB. The column can be deployed into a tank using metal flange/column assembly for structure. The tank contents are allowed to enter the inter-electrode spacing via a notch in the deployment column. Technology is measuring bulk permittivity of the contents	EM	Bulk Permittivity	~ 2	0 - 10 pF	In-vessel probe	1. In-situ configuration 2. Expandable to fit more electrodes 3. ECT techniques can be applied to this method (LBP) 4. Resolution function of AD conversion process	1. poor temperature response (due to scaling; poor material selection) 2. single excitation electrode limits capabilities 3. poor spatial resolution 4. single point measurement 5. conductivity of liquid must be evaluated 6. No available commercial vendor/unit	N/A (UMIST)	
Ultrasonic Doppler Velocimetry (UDV) / Acoustic Doppler Current Profiling (ADCP)	Ultrasonic bursts are transceived to determine the relative phase shift caused by suspended particles. This phase shift can be correlated to particle velocities. ADV typically used for measurement of mean velocities and turbulent intensities of sediment motion or fluid currents.	Ultrasound	Doppler shift	0.1 to 50	3 - 250 cm/s	in-vessel probe (lab scale)	1. deployed in-situ for sediment transport measurement 2. single transceiver required for system 3. can provide interface b/w mixing and stationary waste level	1. very limited SNR/resolution in high solids concentration 2. use of lower operating frequency to limit attenuation, would degrade resolution	SonTek/YSI	Prior use in determining sediment transport and turbulence in settled fluidized beds.
Electrical Capacitance Tomography (ECT)	Method measures capacitance between source electrode, and a circular array of detector electrodes. The source/detector configuration is changed for each array element to create spatial grid of measurement paths. These values, when processed utilizing a linear back-propagation algorithm, can be expanded to create a map of permittivity distribution of the working space bounded by the electrode array.	EM	Bulk Permittivity	up to 200 (frames)	None defined	in-line configuration (lab version)	1. Can monitor changes in relative permittivity with accuracy of 5% 2. Can determine solids distribution within measurement area	1. designed for in-line analysis 2. designed for lab use 3. Use linear back propagation algorithm to generate permittivity distribution map (approximation)	Tomoflow	
Energy Dispersive X-ray Diffraction (EDXRD)	Method solves the Bragg equation, while maintaining the Bragg angle as constant. This method detects the wavelength of the diffracted beams of the originally polychromatic beam. This method does not require a goniometer, as required for typical angle-dispersive diffraction techniques, thereby simplifying the deployment for XRD.	Optical/EM	chemical composition based on diffraction pattern	None defined	None defined	lab version	1. Allows for chemical composition and physical characterization	1. x-ray source and optics required near measurement area 2. no in-situ systems available	Xstream Systems	
Electrical Resistance Tomography (ERT)	Method measures voltage between pairs of electrodes that has been injected by a source electrode. The source/detector configuration is changed for the array elements to create a 2D estimate of measurement paths. These values, when processed utilizing a linear back-propagation algorithm, can be expanded to create a map of conductivity distribution of the working space next to the electrode array.	EM	conductivity (solids concentration)	None defined	None defined	in-situ probe	1. linear probe in field ready configuration (tested in 3.5M nitric acid reactor) 2. Correlation between conductivity measurement and solids concentration (Maxwell's Eq) 3. Can be used for phase detection	1. Use of modified sensitivity back propagation (MSBP) algorithm for map (approximation) 2. electrochemical double-layer effect 3. Susceptible to EM noise near electrodes	Industrial Tomography Systems plc	Tested for sludge settling at UMIST (T. York) in impedance mode in a trident configuration; successfully tracked sludge settling when compared to visual inspection
Lamb (Stoneley) Wave Viscosity Measurement	Method uses shear wave along interface between liquid and solid media and wave equation to determine viscosity of liquid media. Can be applied as a Lamb wave (at end of waveguide), or completely along boundary (Stoneley)	Ultrasound	Viscosity	None defined	< 7 mPa	lab version	1. capable of in-situ measurement 2. simple sensing electrode / electronics module 3. no field calibration necessary	1. Only available in lab scale configuration; no industrial deployments 2. Additional research efforts required to determine optimum deployment configuration and assess impact of multi-phase media 3. Limited viscosity range in current incarnation	N/A	
Laser Diffraction	Method uses photodetectors to measure diffraction patterns generated by particles interacting with a near IR laser light. Typically used in dilute applications, within air or clear fluids. Multiple scattering phenomenon has been used with techniques to correct dynamic range of instruments under high solids loading applications	Optical	Particle Size Distribution (PSD)	None defined	0.1 - 1000 um	in-line configuration / in-situ configuration	1. determined actual system PSD 2. in-situ deployment probe available 3. no field calibration necessary	1. requires dilute concentrations 2. probe not chemical/rad hardened 3. limited probe length	Malvern Instruments	Discussions with representative (M. Lighfoot) yielded that Parsum IPP 70 could NOT be used in chem hardened fluid due to window material
Raman Spectroscopy	Method uses the vibrational spectra given off by chemicals when interrogated by a laser in the visible/near-infrared region to determine their identity. Method requires reference Raman signatures in order to classify the resulting spectral response. Method has limitations when interrogating dark matter, as very little light is reflected.	Optical	Chemical composition/concentration	None defined	dependant on reference library number of signatures	in-situ probe (ITSR)	1. in-situ deployment probe available 2. provides composition and concentration measurements 3. testing resulted in over 90% accuracy in identification and concentration	1. requires reference signature library for identification 2. pronounced peak from a specific compound can obscure others 3. signal quality was an issue in in-tank configuration evaluated by Hanford (w/ CPT for deployment)	Kaiser Optical Systems Inc.	Tested at Hanford (ITSR) with Cone Penetrometer for deployment. Never tested in HLW tank
Dynamic Light Scattering	Method consists of a monochromatic laser light that falls on a sample region, while the scattered light is detected at various solid angles. This data can be used to calculated the PSD using the mathematical model for light scattering phenomenon (Mie Theory)	Optical	Particle Size Distribution (PSD)	None defined	< 6.5 um (lab version)	lab version probe	1. direct PSD measurement 2. reliable measurements 3. no calibration required	1. low particle size applications 2. no in-situ systems available	Wyatt Technology/Microtrac	
Ultrasound Spectroscopy (USS)	Method measures the change in ultrasonic signal per unit distance at various interrogation frequencies. This causes an energy loss in the wave that is characteristics of the material properties.	Ultrasound	Density and Viscosity	slurry dependant	slurry dependant	lab version probe	1. direct bulk density and viscosity measurement 2. simple transmitter-receiver pair configuration 3. Data can be used for trending on mixing process homogeneity	1. no in-situ systems available 2. requires standards/calibration for results interpretation	Industrial Tomography Systems plc	
Vibration-based Density measurement	The vibration-based density measurement is a technique that utilizes the damping caused by the test material on a vibrating object(s) to determine the material properties. This method that has been utilized in industry for some time in several incarnations; these include tuning forks, twin-tube and Coriolis-force based meters	vibration/resonant damping	Density and Viscosity	~ 50	Density: up to 3.00 g/cc (tuning fork; undefined for other types)	in-situ probe (tuning fork/Coriolis)	1. simplicity of measurement principle 2. compatible with chemically-agressive slurries 3. on-board temperature and viscosity compensation	1. on-board electronics 2. element fouling/plugging can lead to measurement errors 3. limited density range (tuning fork) 4. sensitive to bubbles and fast composition changes 5 sensitive to flow pattern changes/stray currents (due to jet flow)	Emerson Process (Rosemount), Endress-Hauser, Micromotion	